The Influence of the Laser Induced Plasma in the Pulsed Laser Deposition of ZnO

Eduardo de Posada

Submitted for the degree of

Doctor of Philosophy

University of Dublin

Trinity College

Physics Department

February 2005

Declaration

This thesis has not been submitted as an exercise for a degree at any other university. The work described is entirely my own, except for the assistance mentioned in the acknowledgments and the collaborative work mentioned in the list of publications. I agree that Trinity College Library may lend or copy this thesis upon request.

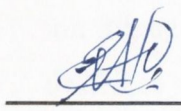

Eduardo de Posada

Summary

The thesis is divided in three main sections, two of them Chapter 2 and 3 are devoted to the study and analysis of the laser produced plasma. Finally in the third section (Chapter 4) the conclusions obtained in the first two sections are used as the basis for the explanation and discussion of the results obtained from the film growth.

In the Chapter 2 both the in vacuum and in a gas background plasma expansion was analysed. In vacuum all the analysis is supported on the Anisimov model. Using ion signals, acquired with a Langmuir probe, it is corroborated that this model describes successfully the expansion of laser produced plasma. In the case of plasma expansion in a background gas, firstly, a full characterization of the expansion is performed using intensified charged coupled device (ICCD) photography and ion signals. The Sedov-Tylor model is applied and it is shown that it describes the general features of the expansion, i.e. front expansion ~ $t^{2/5}$; however it failed in a full description of the plasma properties. It is proposed, that, the Freiwald-Axford model may be more appropriate, though such model is not applied in its original form. Based on some assumptions, which were used by the authors during the mathematical formulation of the model, the idea of describing the plasma contact front instead of the commonly described shock front is proposed. This allowed at the same time to use the plasma specific heats ratio as obtained from Anisimov model instead of approximated values of the same physical magnitude but for the gas background. A detailed comparison between the two models and the correctness of the plasma expansion velocities, positions and pressures corroborated that such an approach is correct. It is shown that the use of ion signals as extracted using the Langmuir probe is not correct for describing the plasma front. On the other hand the use of ICCD photography is correct. It is corroborated that in a background gas the plasma reaches a maximum in its expansion which is well predicted by the Predtechensky model. Beyond this distance the plasma enters in a diffusive regime which is well described by a 3-D diffusion model. It is shown that plasma properties such as initial energy and specific heats ratio obtained from the Anisimov model can be used as input for the initial conditions of the plasma expansion in a background gas.

In Chapter 3 the study is directed to the plasma internal properties. Using emission spectroscopy the plasma is shown to be composed mainly of atomic

species. Theoretical validity criteria for the assumption of existence of a local thermal equilibrium (LTE) or partial local thermal equilibrium (PLTE) in the plasma are applied. It is shown that the Boltzmann plot is a good way of corroborating such criteria. An analysis of the different mechanisms of line broadening is performed, concluding that Stark effect is predominant among the pressure mechanisms. The Doppler broadening is discussed and it is shown that for laser produced plasma expanding in vacuum this broadening is due to the supersonic velocities of the plasma expansion rather than the thermal velocities of the radiating species. It is proposed to calculate a "median" value of such broadening by using the angular distribution of the species in the plasma, as calculated with the Anisimov model. Synthetic spectra are generated to fit the experimentally obtained data and from them the plasma ion/electron density and the temperature are extracted. All calculations are performed taking line self-absorption into account. Good agreement between the ion densities extracted with the Langmuir probe and from the synthetic spectra is found. The importance of considering the Doppler broadening is also shown. The Langmuir probe technique is studied and the typical Koopman circuit is analysed. It is corroborated that it behaves as a passive high pass filter which does not affect the probe current unless the signal frequency is less than the circuit cut-off frequency. It is shown, however, that care must be taken with the voltage drop due to the probe current. It can offset the bias voltage leading to a wrong I-V plot and the consequent error in both temperature and electron density extracted from it.

In Chapter 4 the results obtained from the thin film depositions are presented. Structure, surface smoothness and optical properties of the ZnO thin films are studied and shown to present good quality. Similar results are presented from the Mn doped ZnO thin films. In this case the magnetic properties are also presented, showing that the obtained films have high critical temperature (> 300 K). It was shown that oxygen incorporation into the growing thin film occurs, preferentially, during the material condensation on the substrate.

Finally, it is discussed that the optimum conditions for the growth of good quality thin films can be predicted from models or at least bounded between some limits.

Acknowledgements

This is for me the hardest part. The space and my writing skills work in this direction. There has been 5 years of every day experiences and above all 5 years of friendship. The biggest thank you to every single person that contributed to develop my sincere appreciation for this country.

If I then keep closing the loop, it is impossible to forget the staff of the physics department, Tom Burke and John Kelly, Michelle Duffy and the rest of the gang. Next stop the workshop, Dave and Mick, what a combination. Ken for spending hours with my self governed computer, he was the only one who understood it.

Juan Castro, Carlos Beitia, Ruis, Tue Hansen have to be mentioned in here. Others within the present generation are Lee, Greg, Chris, Ciara and Venki and the rest of the army spread out in this building.

A long time ago a poet and national hero of my country, **Jose Marti**, wrote:

Tiene el Leopardo un abrigo
en su monte seco y pardo,
yo tengo mas que el Leopardo
porque tengo un buen amigo

I'm even richer; I've got two friends Donagh O'Mahony and Brendan Doggett.

I would like to thank my supervisor James Lunney. The opportunity he provided me with is the main reason for meeting you all. I have to mention the incredible patience he had in dealing with me during all these years.

Finally thanks to my parents and family in general, which even being so far away always managed to give me their support. My wife, which through all this years has afforded long separations and has demanded nothing but the best of the result in my work. To my daughter who is celebrating her birthday as I write this. Perhaps my only gift to her will be that I am handing in this work.

Table of contents

Introduction

The development of the electronic industry and the requirement to produce thin films of new materials has opened a wider field for the laser application known as Pulsed Laser Deposition (PLD). The relative simplicity of the technique, coupled with comparatively inexpensive equipment requirements, as well as its success in growing high quality high temperature superconducting materials, are the main reasons for interest in the study of this technique. PLD involves a rather complex group of physical and chemical processes which in general can be divided into three main regimes. Firstly, photons are absorbed by the material and energy released in a small volume ($\sim 3\times10^{-7}$ cm^3 in the experiments described in this thesis). This allows temperatures of the order of the melting or vaporization temperatures for the material to be reached. The next regime is plasma formation. A vapour layer on top of the material surface increases its degree of ionization due to both interactions with the laser pulse and particle collisions. Finally, the plasma expands away from the material surface. In general the main goal in the process is to obtain a thin film with good stoichiometry. Although PLD has proved adequate in achieving good stoichiometry, problems arise when growing oxide or nitride compounds. For these materials a lack of oxygen or nitrogen in the as-grown film is detected. Scattering during expansion, re-evaporation and sputtering from the substrate, due to particles with high kinetic energies, are the main reasons for such behaviour. The introduction of a background gas during the deposition process has been used to overcome these problems. In addition to the experimental achievements of the technique, great attention has being given to the development of the theoretical basis.

Plasma expansion is of particular importance to the PLD technique for the following reasons. The initial conditions or properties of the plasma are related, to some extent, to the way the vaporization processes takes place and on the other hand, the behaviour of the plasma expansion plays an important role in the final properties of the thin film (film thickness, homogeneity, stoichiometry, etc.). Studying the plasma properties and its evolution in both time and space gives a better insight into the overall process. Great attention has been given to this topic. As a result several models have been developed and a wide range of characterization techniques have been applied. Despite the available theory, it is no secret for those who work in this field that models stand in a second place during the thin film growth. A trial and

error process takes place until a film with the desired characteristics is obtained. In addition, particularly for oxides, post-deposition annealing is common in order to obtain the final stoichiometry. As a result, a simple review of the literature results in different reports in which good quality thin films of the same material have been obtained while grown under considerably different deposition conditions [Dinescu, et al., 1996;Ohtomo, et al., 1998; Ryu, et al., 2000;Sankur, et al., 1983;Shim, et al., 2002;Tang, et al., 1998;Wu, et al., 2001].

The question that arises is whether the optimum conditions for the growth of good quality thin films can be predicted from models or at least bounded between some limits. Indeed, this topic forms the basis of the discussion presented throughout this thesis, which main goals are:

- To study and characterise the expansion of the laser produced plasma during the PLD of ZnO thin films.
- To apply and compare different models devoted to this topic and identify those more relevant for PLD.
- To identify the possible ways of oxygen incorporation.

The reasons of selecting ZnO as the studied material are as follow; apart from its well known applications in solar cells and surface acoustic wave devices (SAW), amongst other, it has emerged as an important material for developing near UV semiconductor lasers. Recently good results are being obtained using it as a matrix for magnetic doping in the race for the development of so-called spin-electronic devices [Fukumura, et al., 1999].

Thesis outline

Chapter 1

Describes and presents the experimental set up used throughout this thesis. Techniques which were used for the analysis of the plasma, Emission spectroscopy, Fast ICCD photography and Langmuir probe are introduced. Maximum values of the estimated errors are presented for parameters quoted throughout the thesis.

Chapter 2

Expansion of the plasma will be treated for both cases of vacuum and in the presence of oxygen background. For the in-vacuum expansion, a 3D model will be

presented while for the expansion in gas background several models will be discussed. In the latter case, regions in which they apply as well as parameters that can be extracted will be given. The analysis will be based, mainly, on the experimental results obtained with the above mentioned techniques in the TOF mode.

Chapter 3

Presents a discussion on the use of Langmuir probe technique in the study of laser produced plasmas expansion in gas background. Also discussed is a study of the possible modifications which the electrical circuit can make to the real signal. Presents results of the study performed using emission spectroscopy. Both techniques are combined to extract the plasma parameters.

Chapter 4

Here, characterization of the grown thin films is presented. Structural, stoichiometry, morphology and optical properties are analysed. Conclusions from previous chapters are brought together and mechanisms for film growth are identified emphasizing the oxygen incorporation.

References

Dinescu, M. and P. Verardi, *Applied Surface Science*, **106**, p. 149 (1996).

Ohtomo, A., M. Kawasaki, Y. Sakurai, et al., *Materials Science & Engineering B: Solid-State Materials for Advanced Technology*, **B54**, p. 24 (1998).

Ryu, Y. R., S. Zhu, J. D. Budai, et al., *Journal of Applied Physics*, **88**, p. 201 (2000).

Sankur, H. and J. T. Cheung, *Journal of Vacuum Science & Technology A*, **1**, p. 1806 (1983).

Shim, S., H. S. Kang, J. S. Kang, et al., *Applied Surface Science*, **186**, p. 474 (2002).

Tang, Z. K., G. K. L. Wong, P. Yu, et al., *Applied Physics Letters*, **72**, p. 3270 (1998).

Wu, X. L., G. G. Siu, C. L. Fu, et al., *Applied Physics Letters*, **78**, p. 2285 (2001).

Fukumura, T., Z. Jin, A. Ohtomo, et al., *Applied Physics Letters*, **75**, p. 3366 (1999).

Chapter 1 PLD. Experimental set up and characterization techniques

1.1 Experimental set up

Figure 1.1 shows a schematic of the experimental apparatus required for a PLD system.

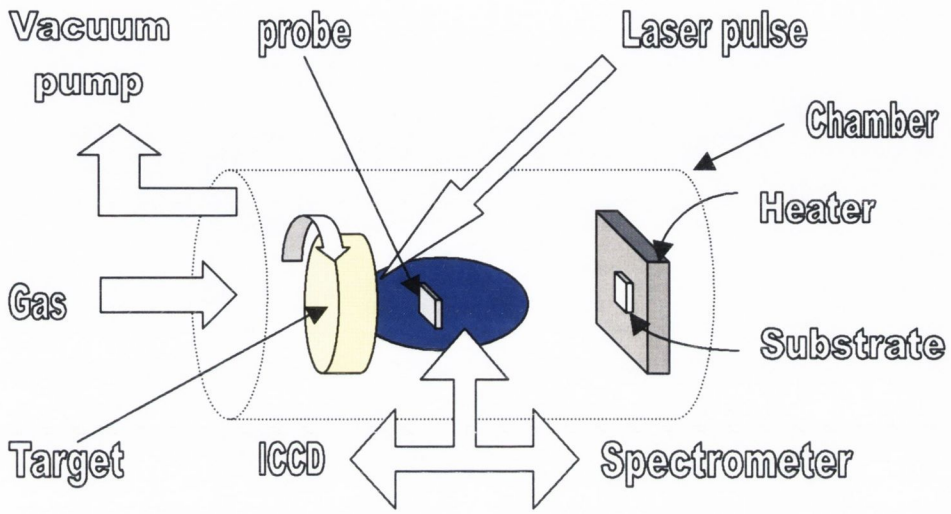

Figure 1.1. General scheme of a pulsed laser deposition system.

In general the setup can be divided into two main sections. A laser able to deliver up to hundred millijoules per pulse and a vacuum chamber in which is placed both the material to be ablated and the substrate where the plasma plume condensates to obtain a thin film, form the first section. Gas sources and substrate heater are also part of it. The laser pulse energy, both gas background species and pressure, target-to-substrate distance and substrate temperature are the variables that can be optimised in order to obtain good quality thin film growth. The second section describes all the different methods and techniques used for the characterization or monitoring of the deposition process.

For this thesis a KrF (248 nm, 26 ns) excimer laser was used for ablation. The work was carried out in a stainless steel chamber with a base pressure of $8x10^{-6}$ mbar using a Pfeiffer-Balzers TSH 050 turbo molecular system (50 l/s). When working in a background gas, 5.0 grade oxygen (Air Products) was fed through a Whitey needle-valve into the chamber. A Balzers Penning was used as pressure gauge for the 10^{-5} to10^{-3} mbar range. For the region of 0.2-1 mbar an Edwards Pirani gauge was used. The latter was calibrated using a Hastings HPM-2002-OBE wide range gauge, which

consists of a dual sensor unit containing a piezoresistive direct force sensor and a thin film Pirani type sensor. Substrate heating was accomplished by using a resistive heater able to reach up to 1000 ^{0}C. The temperature was controlled using a Eurotherm 94 PID controller and a k-type thermocouple as a sensor. An Ultimax UX-20 optical pyrometer was used for temperature corroboration. The laser pulses were focused on the rotating target (Chapter 4) using a 50 cm focal length lens obtaining a rectangular spot of 0.6 x 0.1 cm dimensions. The laser pulse was incident at an angle of 45^{0} to the normal of the target. The spot dimensions were kept constant and the fluence was varied by varying the energy of the pulse. The average energy per pulse was measured using a Scientech thermopile joulemeter.

1.2 Characterization techniques

In general terms the characterization methods commonly used in the PLD technique can be labelled as post deposition methods. This is, the characterisation of the obtained thin film properties (structure, stoichiometry, etc.), after the growth process. The other approach is to study the film properties during the growth process, which is called the *in situ* method. Examples of techniques that are used for the *in situ* characterisation are Optical reflectometry and RHEED. Others *in situ* characterization techniques are those used for the study of the plasma produced during the growth, such as absorption and emission spectroscopy and the Langmuir probe. The physics of a laser produced plasma limits the applicability of the different diagnostic techniques. Generally each diagnostic method allows a view of just one or two components of the plasma plume (atoms, ions, molecules, etc.). So to develop an understanding of the plasma features, it is necessary to work with different techniques.

1.3 Optical Emission Spectroscopy. Basics

The presence of excited species within the plasma plume allows the use of optical emission spectroscopy. The theory developed in spectroscopy can be used to obtain densities and temperatures of different species. This is due to the fact that the recorded spectrum of a plasma is the final result of the perturbations due to the different interactions over the ideal spectra of the isolated species. Broadening or

shifting of the profiles, appearance of emission lines and changes in line intensities are examples of the effects a plasma induces.

Once a transition is optically allowed its intensity will be defined by the density of population at the upper level and the strength of the line, the latter is an intrinsic property of the specific atom. So if the above mentioned atomic properties are known, the intensity of the lines in the recorded spectra are related to the population of the level from which the transition starts. At the same time non-emissive depopulation mechanisms will take place. In general several populating and depopulating* mechanisms take place, each of which are the ways a specific level interacts with its neighbourhood. Examples of these mechanisms are:

- Excitation - De-excitation*
- Ionisation - Three body recombination*
- Autoionization - Dielectronic recombination*
- Radiative recombination

All these rates depend on the electron temperature (T_e) in the plasma and how important they are within the whole populating-depopulating process is dependent of the electron density (n_e) in the plasma [Griem, 1997].

Plasmas can be divided in three regions regarding electron densities:

- $n_e<10^8$ cm^{-3}. In this region only ionisation and radiative recombination rates are important. Their ratio will define the density ratio of two consecutive ionisation stages of a species. This is called the Corona ionisation model.
- $10^8<n_e<10^{16}$ cm^{-3}. All the rates have to be taken into account and the net balance will define the density of population of the species. This is the Collisional Radiative model.
- $n_e>10^{16}cm^{-3}$. High density region where the level population will be in local thermal equilibrium (LTE) and the atom, ion and electron density will be described by the Saha-Boltzman model.

Due to its simplicity the Saha-Boltzman model is the most widely used. It is clear of course, that the plasma under study should meet the conditions where a LTE can be assumed. Validity criteria with this aim have been developed [Griem, 1963]. Different criteria will apply depending on whether the plasma is homogeneous or inhomogeneous, transient or time independent and if optically thin or thick with

respect to the resonance line of the emitting species. On the other hand a partial LTE (PLTE) can exist where certain levels are in LTE, not with respect to their ground level, but with respect to the ground state of the next higher ionization stage. In all cases the criteria, for either PLTE or LTE, is fulfilled if the electron density in the plasma is greater than a critical value:

- Partial LTE in homogeneous time independent plasma:

$$n_e = 7.4x10^{18}\left(\frac{z^7}{n^{\frac{17}{2}}}\right)\left(\frac{kT_e}{1.602x10^{-19}E_z}\right)^{\frac{1}{2}} \qquad (1.1)$$

where n is the level for which the criteria is applied. E_z is defined as:

$$E_z = \frac{z^2e^2}{2a_0}$$

z is the effective charge, equal to 1 for atomic species, 2 for single ionised and so on.

- Complete LTE in homogeneous time independent plasma. Optically thin with respect to the resonance line:

$$n_e = 9.2\times10^{17}z^7\left(\frac{kT_e}{1.602x10^{-19}E_z}\right)^{\frac{1}{2}}\left(\frac{E_{up}}{E_z}\right)^3 \qquad (1.2)$$

where E_{up} is the energy of the upper level of the resonance line.

- Complete LTE in homogeneous time independent plasma. Optically thick with respect to the resonance line:

$$n_e = 10^{17}z^7\left(\frac{kT_e}{1.602x10^{-19}E_z}\right)^{\frac{1}{2}}\left(\frac{E_{up}}{E_z}\right)^3 \qquad (1.3)$$

In all cases the electron density is in cm^3 and the energy in eV. Figure 1.2 shows the critical densities as calculated using each of the previous equations.

In addition to the criteria outlined in equations (1.1), (1.2) or (1.3), a further requirement for transient plasmas is that changes in electron temperature and other plasma parameters are small over times characterizing the establishment of excitation and ionization equilibrium. Similarly, for inhomogeneous plasmas, the following condition needs to be introduced; the gradients in electron temperature are so small that an atom does not diffuse, at least during the time needed for the establishment of excitation and ionization equilibrium, over regions of significantly different temperatures.

Other important methods that do not rely on obtaining local thermal equilibrium are based on Doppler and pressure broadening and shifting of the lines profiles, which depend on the plasma temperature and density [Griem, 1997].

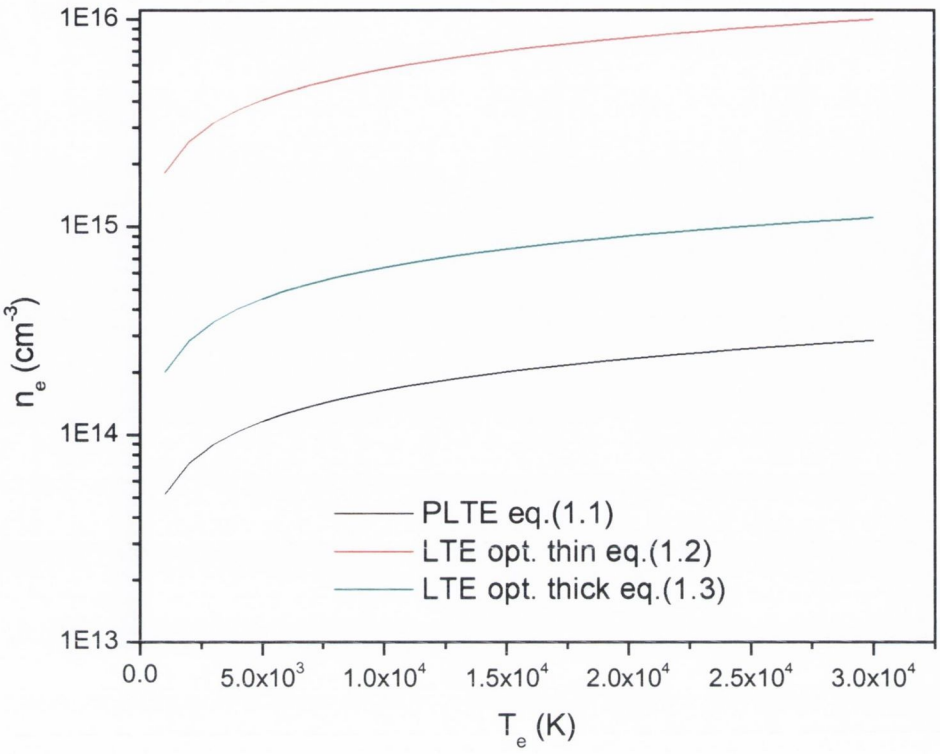

Figure 1.2. Critical densities for the fulfilment of PLTE and LTE in a plasma. PLTE was calculated for n =3.

1.3.1 Spectrometer and delivery system

A 25 cm focal length Oriel Imaging Spectrometer coupled to an Andor ICCD camera was used. The spectrometer focal length together with both a 1200 lines/mm grating and 50 μm slit ensured a spectral resolution of 0.175 nm. The spectra were recorded in both time and space resolved mode over a distance of 0-35 mm from the target surface, which is the typical range of target-substrate distances used in PLD. A Stanford delay generator, with a time resolution of 5 ps, was used to trigger the ICCD. All measurements were performed with a time window of 18 ns on the image intensifier and the counts on 8 pixels were binned together and summed over 100 laser shots at each wavelength. The ICCD detector was cooled to 0 ^{0}C.

Figure 1.3 shows a schematic diagram of the optical system used to image the plume on the spectrometer slit. It includes a system of mirrors to rotate the image of

the ablation plume so that the axis normal to the target lies along the spectrometer slit; thus making it possible to obtain space resolved measurements along that axis. The ICCD array was divided into 5 tracks, which allowed simultaneous recording of the emission from 5 different positions from the target surface (5, 10, 18, 26 and 33 mm).

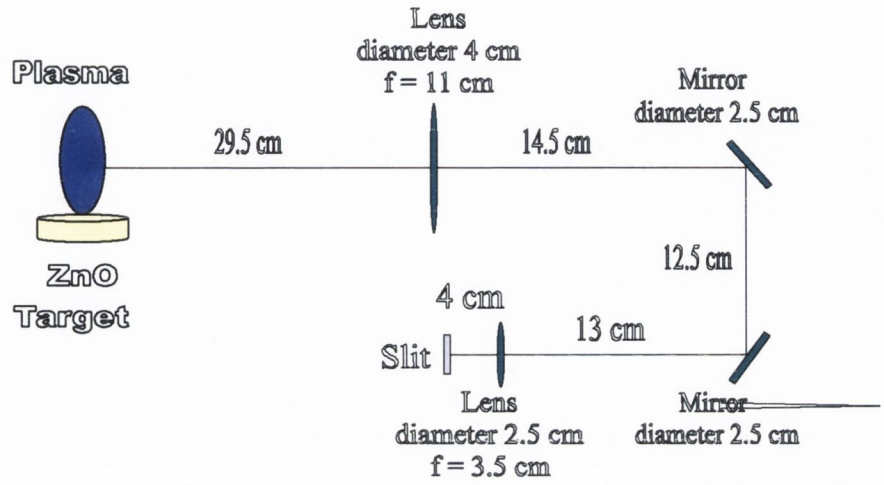

Figure 1.3. Schematic diagram of the optical delivery system used for spectroscopic study.

1.3.2 Spectrometer calibration

Spectral and sensitivity calibration of the spectrometer is of great importance when performing spectroscopical analysis. The identification of the emitting or absorbing species relies on the accuracy of the spectral calibration. This accuracy is limited by the resolution of the spectrometer. The wavelength calibration was performed using a Hg spectral lamp and corroborated using band-pass filters and a diode laser. On the other hand sensitivity calibration is needed to obtain the proper spectral energy distribution of the emission.

In general terms, the number of counts obtained when using a CCD as a sensor of emitted light by a source, is a measure of the number of photons that arrived to the active area of the sensor. In spectroscopical analysis, generally, a certain amount of the light emitted by the source is collected and delivered onto the entrance of the spectrometer and after it has been diffracted is delivered onto the sensor surface. During this process several factors cause losses or changes in the spectral energy

distribution of the collected light. Scattering, reflection and both diffraction grating and sensor spectral response are examples of such factors. A calibration process has the aim of defining a general response function that accounts for all the above mentioned factors and establishes a correlation between the collected light and the final measurement result.

As mentioned above an ICCD is a device which is sensitive to the photons arriving on its surface producing as a response a certain number of counts. The counts to photons relation can be defined by:

$$C(\lambda) = F(\lambda)\#_{photon} \qquad \text{(Counts)} \qquad (1.4)$$

where $F(\lambda)$ is a function that covers all the factors that modulate the real number of photons , $\#_{photon}$, collected from the source.

If a source with a known irradiance ($E(\lambda)$) is used, the number of photons collected is at each wavelength:

$$\#_{photon} = \frac{E(\lambda)at}{hc/\lambda} \qquad (1.5)$$

where a is the area over which the flux is measured, t is the time duration of the measurement and λ is the wavelength.

In order to correct for the above factors the absolute sensitivity for both delivery system and spectrometer was measured using an Oriel 6333 100 W quartz halogen lamp. This lamp produces a uniform flux density, $E_L(\lambda)$, over an area of 2.5 x 2.5 cm^2, at a distance of 50 cm. The manufacturer's tabulated values were fitted using the expression for the black body irradiance $E_L(\lambda, T)$, given by:

$$E_L(\lambda,T) = A_{fit}\,3.74\times10^{20}\,\lambda^{-5}\left(e^{\frac{1.44\times10^7}{\lambda T}} - 1\right)^{-1} \quad (\text{W m}^{-2}\text{ nm}^{-1}) \qquad (1.6)$$

where A_{fit} was introduced as a scaling constant and λ is the wavelength in nm. The best fit gave the following values: $A_{fit} = 1.83 \times 10^{-5}$ and $T = 3317.8$ K.

The equation (1.4) can be rewritten for the lamp case as:

$$C_L(\lambda) = F(\lambda)\frac{E_L(\lambda)a_L t_L}{hc/\lambda} \qquad \text{(Counts)} \qquad (1.7)$$

From this equation the function $F(\lambda)$ is obtained as:

$$F(\lambda) = \frac{C_L(\lambda)}{E_L(\lambda) a_L t_L} h c/\lambda \qquad \text{(Counts/\#}_{\text{photons}}\text{)} \qquad (1.8)$$

Using the same procedure the corresponding equation for the plasma is:

$$C_p(\lambda) = F(\lambda) \frac{E_p(\lambda) a_p t_p}{h c/\lambda} \qquad \text{(Counts)} \qquad (1.9)$$

from which:

$$E_p(\lambda) = \frac{C_p(\lambda)}{F(\lambda) a_p t_p} h c/\lambda \qquad (\text{W m}^{-2}\ \text{nm}^{-1}) \qquad (1.10)$$

and using equation (1.8)

$$E_p(\lambda) = \frac{C_p(\lambda) E_L(\lambda) a_L t_L}{C_L(\lambda) a_p t_p} \qquad (\text{W m}^{-2}\ \text{nm}^{-1}) \qquad (1.11)$$

To obtain the radiance, $L_p(\lambda)$, of the plasma, equation (1.11) is divided by the solid angle, Ω_p (the solid angle accepted by the overall system) obtaining:

$$L_p(\lambda) = \frac{C_p(\lambda) E_L(\lambda) a_L t_L}{C_L(\lambda) a_p t_p \Omega_p} \qquad (\text{W m}^{-2}\ \text{sr}^{-1}\ \text{nm}^{-1}) \qquad (1.12)$$

The effective area from which photons were collected is defined by the width of the slit (SW) in one axis. This axis is constant for both lamp and plasma. The other axis is defined by the number of pixels recorded in the experiment ($\#_{pixels}$). In general the area (a) is a function of the optical demagnification (OD) of the delivery system, the instrument magnification (IM) and the slit width and can be defined by:

$$a = \frac{SW}{OD} \times \frac{\#_{pixels}\ 26\mu m}{OD \times IM} \qquad (1.13)$$

Using equation (1.13) and the values for the different parameters, presented in Table 1.1, the final expression for equation (1.12) is:

$$L_p(\lambda) = \frac{C_p(\lambda) E_L(\lambda)}{C_L(\lambda)} 2.78 \times 10^5 \qquad (\text{W m}^{-2}\ \text{sr}^{-1}\ \text{nm}^{-1}) \qquad (1.14)$$

Table 1.1. Values for the parameters on calibration equations.

Optical demagn.	Instrument magn.	SW (μm)	t_L (μs)	t_p (ns)	$\#_{pxls}$ lamp	$\#_{pxls}$ plasma	Ω_p (sr)
0.078	1.6	50	10	18	48	8	0.012

Figure 1.4 shows the lamp irradiance, the lamp spectrum as recorded by the spectrometer and the calibration function $F(\lambda)$.

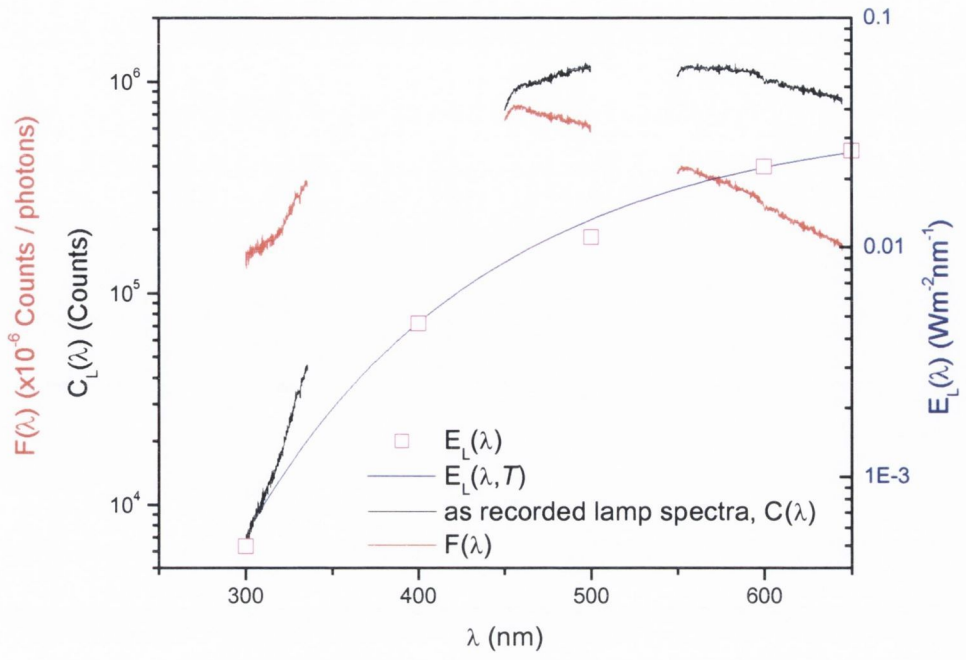

Figure 1.4 Tabulated lamp irradiance $E_L(\lambda)$ (squares), fit using eq. 1.6 (blue line), the recorded lamp spectra $C(\lambda)$ (black line) and the calibration function $F(\lambda)$ (red line).

1.4 Fast ICCD photography

Using the ability of gated ICCD cameras to resolve acquisition windows of the order of nanoseconds, it is possible to study the expansion of a transient process such as the expansion of a laser produced plasma. This study was performed by placing the ICCD camera parallel to the plasma expansion axis and using a combination of two lenses to image the plasma onto the detector of the camera. Figure 1.5 shows a schematic of the system used. A 25 cm focal length and 50 mm diameter lens was used to collect the total emission of the plasma. A lens of 4 cm focal length and 50 mm diameter was the used to produce the image. The axis of the delivery system cut the plasma expansion axis at a distance of 2 cm from the target surface in order to cover a total distance of 4 cm which was the maximum substrate position used for film growth. The demagnification was 1/6 making a pixel in the ICCD equivalent to 0.165 mm along the plasma expansion axis. All the measurements were performed using an acquisition time of 3.8 ns and at different delay times after the arrival of the laser pulse to the target. The acquisition time used guaranteed that even for the in

vacuum expansions velocity of 2.3×10^6 cm/s obtained in the experiments (Chapter 2) the displacement was about 0.09 mm. This corresponds to less than a pixel error (0.165 mm). As for the spectroscopic studies both delay and acquisition times were established using a Stanford delay generator.

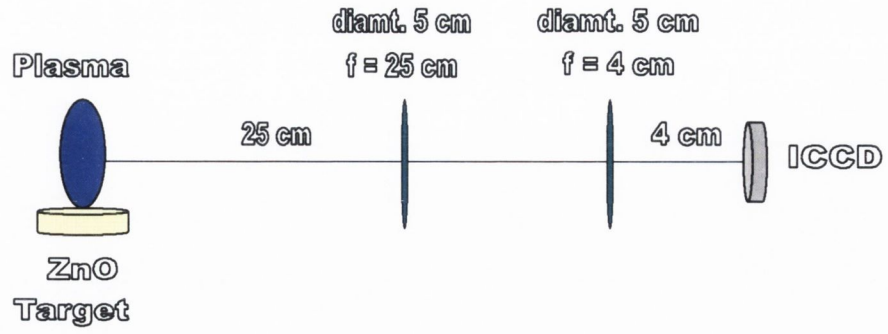

Figure 1.5. Delivery system used for the imaging of the plasma expansion using fast ICCD photography

1.5 Langmuir probe

This technique was introduced for plasma characterization in 1926 when Langmuir [Langmuir, et al., 1926] presented the theory to relate the current of ion and electrons extracted by a conductor immersed in the plasma to its density and temperature. The theory was presented for steady and collisionless plasmas in which the electron energy distribution function (EEDF) was Maxwellian. The technique was extended by Koopmann et al. [Koopman, 1971] to the study of flowing plasmas. In general the basis of the theory and the experimental set up are relatively simple.

Figure 1.6 shows a scheme of the typical (Koopmam) circuit. A conductor probe with a collecting area (A) is introduced in the plasma and biased with respect to a defined ground. The bias voltage is swept from negative to positive voltages allowing for the measurement of ions or electrons respectively. Both theory and experiment shows that at negative voltages high enough as to prevent the electrons with the highest thermal energies in the plasma to reach the probe, the detected ionic current saturates. Furthermore this current is proportional to the density of ions (n_{ion}) in the plasma [Langmuir, et al., 1926] through the following expression:

$$I_{ion} = evAn_{ion} \qquad (1.15)$$

where e is the electron charge, v is the expansion velocity of the plasma and A is the area of the collecting probe. It has been assumed the presence of only single ionized species.

By moving the bias voltage toward positive values, ion repulsion takes place and the current due to electrons increases. In this region the current will be related to the electron energy distribution. For a Maxwellian distribution the measured current is defined as:

$$I = I_{e,sat} e^{\left(\frac{V_{bias} - V_p}{kT_e}\right)} \tag{1.16}$$

where V_{bias} is the bias voltage, V_p is the plasma voltage potential, T_e is the electron temperature and $I_{e,sat}$ is the saturation electron current [Langmuir, et al., 1926]. The saturation electron current region is reached with further increase in voltage to values greater than the plasma potential. At this point there is no longer electron retardation and the current saturates. The measured current will be proportional to the density of electron (n_e) and the average thermal velocity in the plasma (v_e), and is defined as:

$$I_{e,sat} = \frac{1}{4} e v_e A n_e \tag{1.17}$$

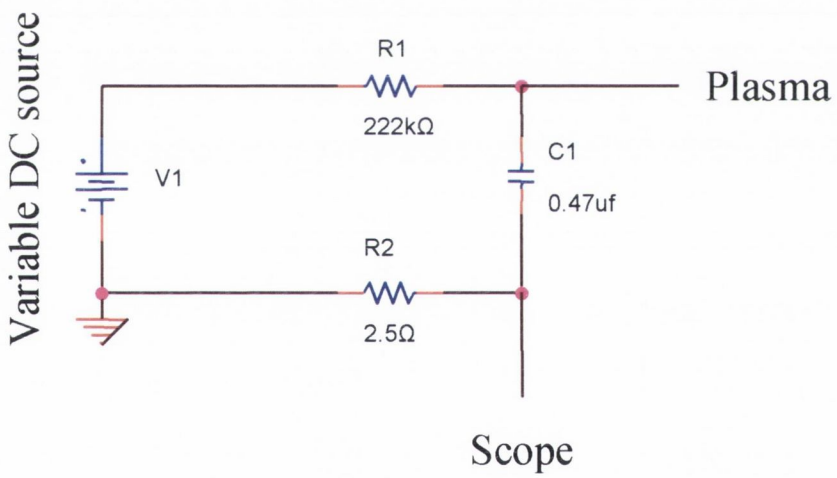

Figure 1.6. Typical Koopmann circuit for the study of flowing plasmas.

Figure 1.7 shows an example of the recorded ion and electron current as the bias voltage is swept from negative to positive values. At each bias voltage the measured current is characterized by a sudden rise which is related with the arrival of the plasma front at the probe, it reaches a maximum that indicates the most probable velocity of the flowing particles (this is valid only for the ion part) and then falls slowly to reach the zero value. At this point the plasma has moved away from the

probe. If at a specific time the value of the current is plotted versus the bias voltage applied in the measurement the so-called I-V curve is obtained. Figure 1.8 (bottom) shows an example of the I-V obtained from Figure 1.7 at 1.36 μs. The red line is an example of how to apply equation (1.15).

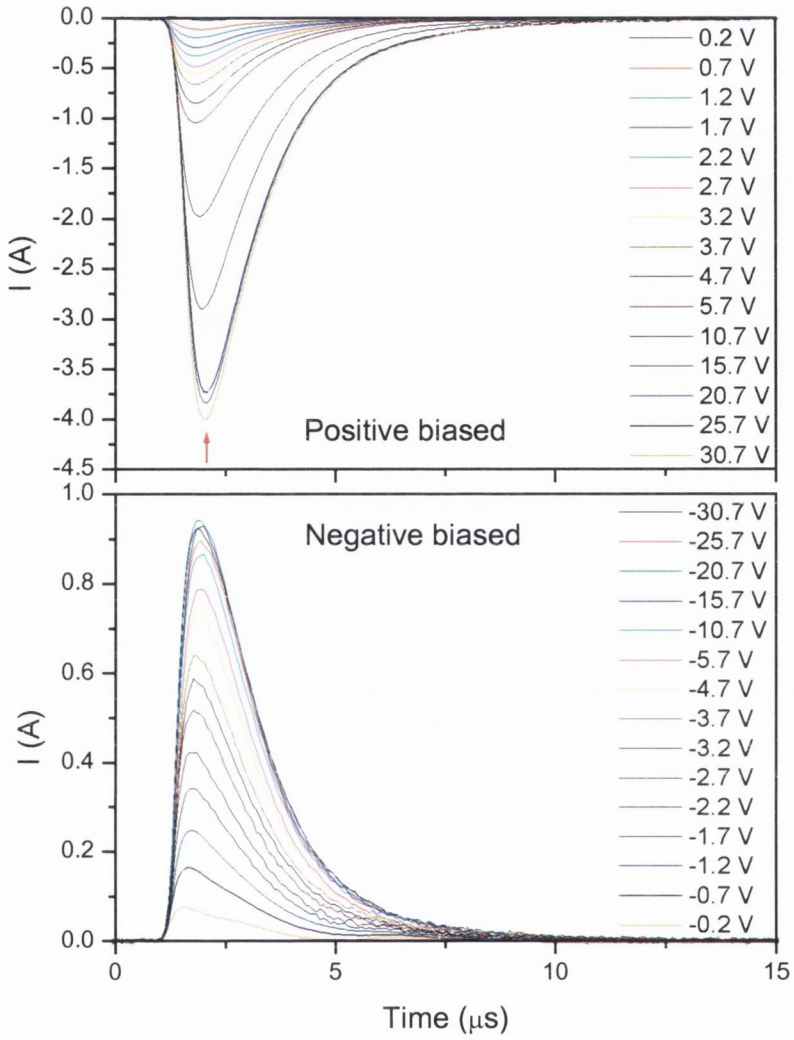

Figure 1.7. Langmuir probe signals, recorded in vacuum at 26 mm from the target, as the bias voltage is swept from -30 V to +30 V.

The top part of the figure shows the plot of the natural logarithm of the I-V after being corrected by subtracting the ion current component of the curve. As represented, using equations (1.16) and (1.17) the temperature and the electron density can be extracted.

Langmuir probe theory is rather complex despite the relative simplicity of the data acquisition. Not only is the electron energy distribution function (EEDF) not always Maxwellian but the geometry of the probe plays an important role. When a probe is

introduced into the plasma it will be surrounded by a shield as a response of the plasma to maintain its neutrality. This is the Debye sheath. It establishes both a boundary within which the plasma neutrality is broken and a limit beyond which the applied bias voltage vanishes.

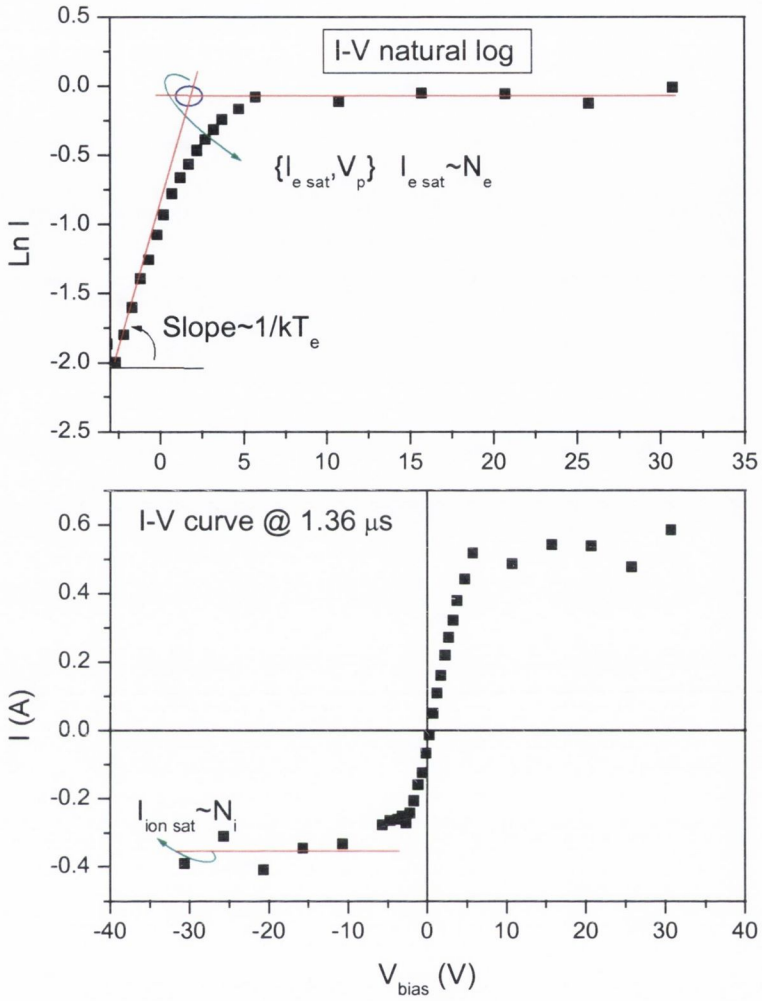

Figure 1.8. Bottom presents an example of I-V from which ion density can be extracted. Top presents the I-V natural logarithm; its slope is proportional to the plasma temperature and the saturation current is proportional to the electron density.

The detected current will depend on both the distribution of carrier density and the potential in the sheath. The mathematical solution describing these distributions is rather complex and has been developed for specific cases such as planar, cylindrical or spherical probe geometry [Swift, et al., 1970]. On the other hand there are different regimes of probe operation which establish limits to the validity of the theories.

The different regimes will be defined by the plasma and probe features such as specie mean free path (λ_{path}), energy relaxation length (λ_{relx}), characteristic probe dimension (d_{probe}) and sheath thickness (h). Three main regimes can be identified as follows:

- Collisionless: $\lambda_{path} >> d_{probe} + h$
- Nonlocal: $\lambda_{relx} >> d_{probe} + h >> \lambda_{path}$
- Hydrodynamic: $d_{probe} + h >> \lambda_{relx}$

Each of the above regimes is divided into different subregimes [Demidov, et al., 2002].

In Figure 1.8 the slope of the linear part of the I-V natural logarithm plot was used to extract the electron temperature. As was mentioned before, this is possible only if the EEDF is Maxwellian. More general methods exist that allow the determination of the EEDF from the measured I-V. Druyvesteyn [Druyvesteyn, 1930] demonstrated the proportionality between the EEDF and the second derivative of the electron current respect to the probe potential. If $F(E)$ is the EEDF, the plasma parameters such as electron density and average electron energy can be obtained as follows:

$$n_e = \int_0^\infty F(E)dE$$
$$\langle E \rangle = \frac{1}{n_e}\int_0^\infty E \quad F(E)dE \tag{1.18}$$

Besides the theoretical conditions which should be fulfilled to apply this technique properly, care most be taken with the design of the circuit. Referring again to Figures 1.7 and 1.8 it can be observed that if an I-V is to be constructed at the time at which the currents reach the maximum it would be incorrect to use the voltage values set by the source. The current at the position marked in Figure 1.7 is approc voltage of 10 V across the resistance, similarly, a voltage $\sim \frac{1}{C}\int I(t)dt$ will develop

a voltage of 10 V across the resistance, similarly, a voltage $\sim \frac{1}{C}\int I(t)dt$ will develop

across the capacitor. At this time the real bias voltage is obtained by subtracting the sum of these two voltages to the one set by the source. More detailed analysis on this topic will be presented in Chapter 3.

1.6 Estimated errors

The following table summarises the maximum errors for several of the parameters values quoted throughout the thesis. Other errors for parameters such as arrival time etc. depend on the specific measurement and will be presented when they are treated.

Table 1.2. Estimated maximum errors.

Parameter	Maximum error
Averaged laser energy per pulse	± 0.005 J
Laser spot area	± 0.007 cm^2
Fluence	± 0.4 J/cm^2
Distance to target	± 0.2 cm
Background gas pressure	± 0.004 mbar
Target mass loss per pulse	± 0.1 μg
Substrate temperature	± 15 ^0C
Radiance and Irradiance	± 5 %

References

Griem, H. R., *Principles of Plasma Spectroscopy* (Cambrige University Press, 1997).

Griem, H. R., *Physical Review*, **131**, p. 1170 (1963).

Langmuir, I. and H. M. Mott-Smith, *Physical Review*, **28**, p. 727 (1926).

Koopman, D. W., *Physics of Fluids*, **14**, p. 1707 (1971).

Swift, J. D. and M. J. R. Schwar, *Electrical probes for plasma diagnostics* (London :Iliffe, 1970).

Demidov, V. I., S. V. Ratynskaia, and K. Rypdal, *Review of Scientific Instruments*, **73**, p. 3409 (2002).

Druyvesteyn, M. J., *Z. Phys*, **64**, p. 781 (1930).

Chapter 2 Plasma expansion

Studies on the expansion of laser produced plasma can be traced back to as early as the 60s, where both the in vacuum [Linlor, 1963] and in gas background [Bobin, et al., 1968] expansion was analysed. From these early studies, it was realised that the expansion was strongly directed along the target normal. Cowin et al. [Cowin, et al., 1978] used TOF measurements to correlate the speed of the plasma components to the surface temperature of the target. By performing angular scanning, it was found that the extracted temperatures were too high for perpendicular emitted particles, while for the obliquely emitted particles the temperatures were too low. Similar behaviour was reported by [Namiki, et al., 1985]. These reports suggested that part or all of this behaviour was due to near-surface gas phase collisions. The region of the vapour where such collisions take place was termed the "Knudsen layer" and it was shown that evaporation of even 0.8 monolayer/pulse was enough for this layer to be developed [Kelly, et al., 1988]. Within the Knudsen layer particles tend to reach equilibrium and develop a common center of mass with a flow velocity directed normally to the target. This speed equals the sound speed in the layer [Kelly, et al., 1988], which is dependent of the temperature in the Knudsen layer. Two possibilities exist for the flow of particles beyond the boundaries of the Knudsen layer. If there are no collisions, a free expansion will develop, whereas if collisions persist, an adiabatic expansion takes place [Kelly, 1989]. For most of the conditions under which the PLD process is carried out an adiabatic expansion is present.

Of great importance for PLD is knowledge of the plasma distribution during its expansion as both film homogeneity and stoichiometry are related to this issue. Again, different models have been proposed to describe these expansions [Bulgakov, et al., 1995;Jeong, et al., 1998a;Leboeuf, et al., 1996], most of them using a gas-dynamic approach and describing both temporal and spatial behaviour of macroscopic parameters, such as density, temperature and expansion velocity. The usual high particle concentration in laser produced plasmas allows the use of gas-dynamic formulation. Although most thin films are grown in the presence of a gas background, PLD of some materials is still carried out in vacuum. In any case knowledge of the characteristics of the in vacuum expansion can be used as a reference or as input data for analysis of the expansion in a gas background. The following two sections present an analysis of the plasma expansion in the

experiments performed for this thesis. The vacuum expansion will be treated separately from the expansion in background gas. For the in vacuum case the Anisimov model will be presented. For gas background different models will be assessed and compared.

2.1 Expansion in vacuum

2.1.1 Anisimov model

Anisimov et al. [Anisimov, et al., 1996] treated the adiabatic expansion of a one component vapour cloud into vacuum using a particular solution of the gas-dynamic equations, which applies when describing flows with self similar expansion. It is assumed that the formation time of the vapour cloud is much less than its expansion time and that the focal spot of the laser has an elliptical shape with semi-axes X_0 and Y_0. The expansion is modelled as a triaxial gaseous semi-ellipsoid (Figure 2.1) whose semi-axes are initially equal to X_0, Y_0 and $Z_0 \approx v_{sound} t_p$, where t_p is the duration of the laser pulse and v_{sound} is the sound speed in the vaporised material.

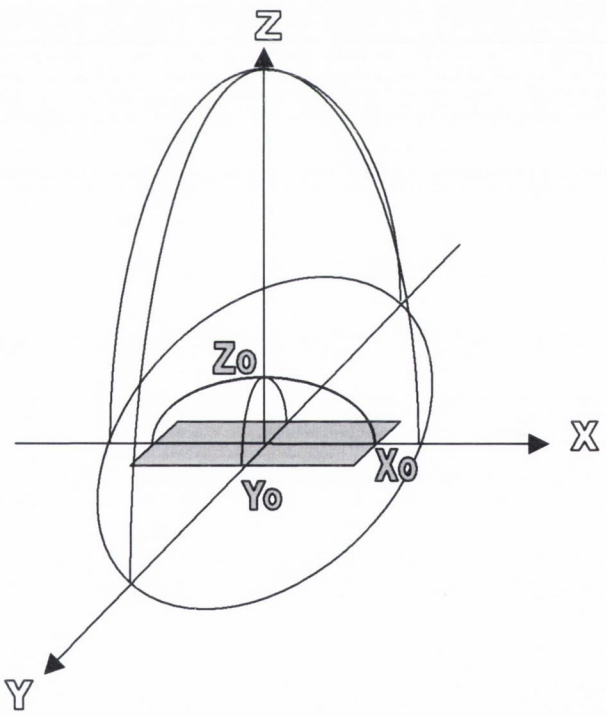

Figure 2.1. Scheme of the ellipsoid assumed for the in vacuum plasma expansion. Grey rectangle represents the laser spot.

The gasdynamic equations are:

$$\frac{\partial \rho}{\partial t} + div(\rho \mathrm{v}) = 0$$
$$\frac{\partial \mathrm{v}}{\partial t} + (\mathrm{v}\nabla)\mathrm{v} + \frac{1}{\rho}\nabla p = 0 \qquad (2.1)$$
$$\frac{\partial S}{\partial t} + \mathrm{v}\nabla S = 0$$

where ρ, p, v and S are the density, pressure, velocity and entropy of the gas respectively. It is assumed that the flow parameters are constant on ellipsoidal surfaces and the density and pressure profiles can be written as:

$$\rho(x,y,z,t) = \frac{M}{I_1(\gamma)XYZ}\left[1 - \frac{x^2}{X^2} - \frac{y^2}{Y^2} - \frac{z^2}{Z^2}\right]^{\alpha}$$
$$p(x,y,z,t) = \frac{E}{I_2(\gamma)XYZ}\left[\frac{X_0Y_0Z_0}{XYZ}\right]^{\gamma-1}\left[1 - \frac{x^2}{X^2} - \frac{y^2}{Y^2} - \frac{z^2}{Z^2}\right]^{\alpha+1} \qquad (2.2)$$

where $M = \int \rho(r,t)dV$ is the mass and $E = (\gamma-1)^{-1}\int p(r,0)dV$ is the initial energy of the vapour cloud and γ is the ratio of the plasma specific heats. The constants I_1 and I_2 are equal to:

$$I_1(\gamma) = \frac{\pi^{\frac{3}{2}}\Gamma(\alpha+1)}{2\Gamma\left(\alpha+\frac{5}{2}\right)}$$
$$I_2(\gamma) = \frac{\pi^{\frac{3}{2}}\Gamma(\alpha+2)}{2(\gamma-1)\Gamma\left(\alpha+\frac{7}{2}\right)} \qquad (2.3)$$

where $\Gamma(z)$ is the Gamma-function. For the pressure and density profiles defined by Eq. 2.2 and when the initial vapour cloud is isentropic ($\alpha=1/\gamma-1$), the entropy depends on the coordinates and time as:

$$S = \frac{1}{\gamma-1}\ln\left\{\frac{E}{I_2(\gamma)X_0Y_0Z_0}\left(\frac{I_1(\gamma)X_0Y_0Z_0}{M}\right)^{\gamma}\left[1 - \frac{x^2}{X^2} - \frac{y^2}{Y^2} - \frac{z^2}{Z^2}\right]^{\frac{\gamma-2}{\gamma-1}}(\gamma-1)\right\} + const \qquad (2.4)$$

Using Eqs 2.2 and Eqs. 2.3, the gas-dynamic equations can be reduced to a set of ordinary differential equations:

$$\begin{aligned}
\ddot{X} &= -\frac{\partial U}{\partial X} \\
\ddot{Y} &= -\frac{\partial U}{\partial Y} \\
\ddot{Z} &= -\frac{\partial U}{\partial Z} \\
U &= \frac{5\gamma - 3}{\gamma - 1}\frac{E}{M}\left[\frac{X_0 Y_0 Z_0}{XYZ}\right]^{\gamma-1}
\end{aligned} \tag{2.5}$$

The initial conditions for Eq. 2.5 are set as:

$$\begin{aligned}
&X(0) = X_0, Y(0) = Y_0, Z(0) = Z_0 \\
&\dot{X}(0) = \dot{Y}(0) = \dot{Z}(0) = 0
\end{aligned} \tag{2.6}$$

In order to integrate Eq. 2.5 numerically, the following dimensionless quantities are introduced, using X_0 as a spatial scale length:

$$\xi\ddot{\xi} = \eta\ddot{\eta} = \zeta\ddot{\zeta} = \left[\frac{\eta_0\zeta_0}{\xi\eta\zeta}\right]^{\gamma-1} \tag{2.7}$$

with initial conditions:

$$\begin{aligned}
&\xi(0) = 1, \eta(0) = \eta_0, \zeta(0) = \zeta_0 \\
&\dot{\xi}(0) = \dot{\eta}(0) = \dot{\zeta}(0)
\end{aligned} \tag{2.8}$$

where

$$\begin{aligned}
\xi &= \frac{X}{X_0}, \eta = \frac{Y}{X_0}, \zeta = \frac{Z}{X_0} \\
\tau &= \frac{t\beta^{1/2}}{X_0}, \eta_0 = \frac{Y_0}{X_0} \\
\zeta_0 &= \frac{Z_0}{X_0}, \beta = (5\gamma - 3)\frac{E}{M}
\end{aligned} \tag{2.9}$$

Equation 2.7 is solved using a fourth order Runge-Kutta-Nyström method. Details of the program and the mathematical method used can be found in Hansen [Hansen, et al., 1999]. From Eq.2.2 we can obtain the mass flux in the Z direction:

$$j(z,t) = \rho(x,y,z,t)\mathrm{v}_z(x,y,z,t)$$
$$\mathrm{v}_z(x,y,z,t) = \frac{z}{Z}\dot{Z} \tag{2.10}$$

The angular dependence of the number of particles arriving per unit area normal to the flow, $J(\theta)$, can be found by integrating Eq.2.10 from the arrival time t_s to infinity [Hansen, et al., 1999]. The arrival time t_s is the time at which the expansion front reaches the position of the probe. If $t_s >> X_0/\beta^{1/2}$ the analytical expression for $J(\theta)/J(0)$ in the plane y-z will be:

$$\frac{J(\theta)}{J(0)} = \left(1+\tan^2\theta\right)^{\frac{3}{2}}\left[1+\left(\frac{Z_{\inf}}{Y_{\inf}}\right)^2\tan^2\theta\right]^{-\frac{3}{2}} \tag{2.11}$$

2.1.2 Results

From Eq.2.9 it can be seen that the model depends on two pure geometric parameters (X_0 and Y_0), which are related to the shape of the laser spot, and a third parameter related to the dimension of the plasma perpendicular to the target surface after the laser pulse has elapsed (Z_0). This parameter depends on the physical properties of the plasma through γ. For a sudden expansion of a gas into vacuum the velocity of the expansion front (v_f) is related to the sound speed through the following expression [Kelly, 1989] $\mathrm{v}_f = 2(\gamma-1)^{-1}\mathrm{v}_s$. The expansion front velocity was calculated from the measured arrival time of the plasma front to different positions using the ion signals from Langmuir probe measurements. The expansion velocity was calculated to be ($\mathrm{v}_f = 2.3\times10^6$ cm/s). In all cases the time at which 10% of the maximum signal is reached was used in the calculations. Numerical calculations were performed for different γ values. Each γ value was used to calculate different v_s and Z_0. Then using Eq.2.10 the current flow was calculated at different positions along the plasma expansion axis. The calculated current flows were compared in each case to the experimentally obtained ion currents in order to obtain the best γ value. Figure 2.2 shows examples of the results. The best fit for both time of arrival

and signal shape was obtained for $\gamma=1.1$. In all cases both the calculated and the ion signals were normalised to their respective maximum. Figure 2.3 shows the time (dimensionless) dependence of the Z/Y, Z/X and Y/X values for $\gamma=1.1$.

The plasma angular distributions in both the X and Y directions were measured by rotating the probe in the x-z and y-z planes respectively. Figure 2.4 shows the normalised ion angular distributions. For the y-z plane the radius of the described circumference was 4 cm from the target, while for the x-z plane it was 7.8 cm. Both data were fitted, using Eq.2.11, giving the ratios $Z/X=2.4$ and $Z/Y=1.8$. Comparison of these values with those predicted by Anisimov model shows good agreement, (see Figure 2.3). This result is another way of corroborating the used γ value.

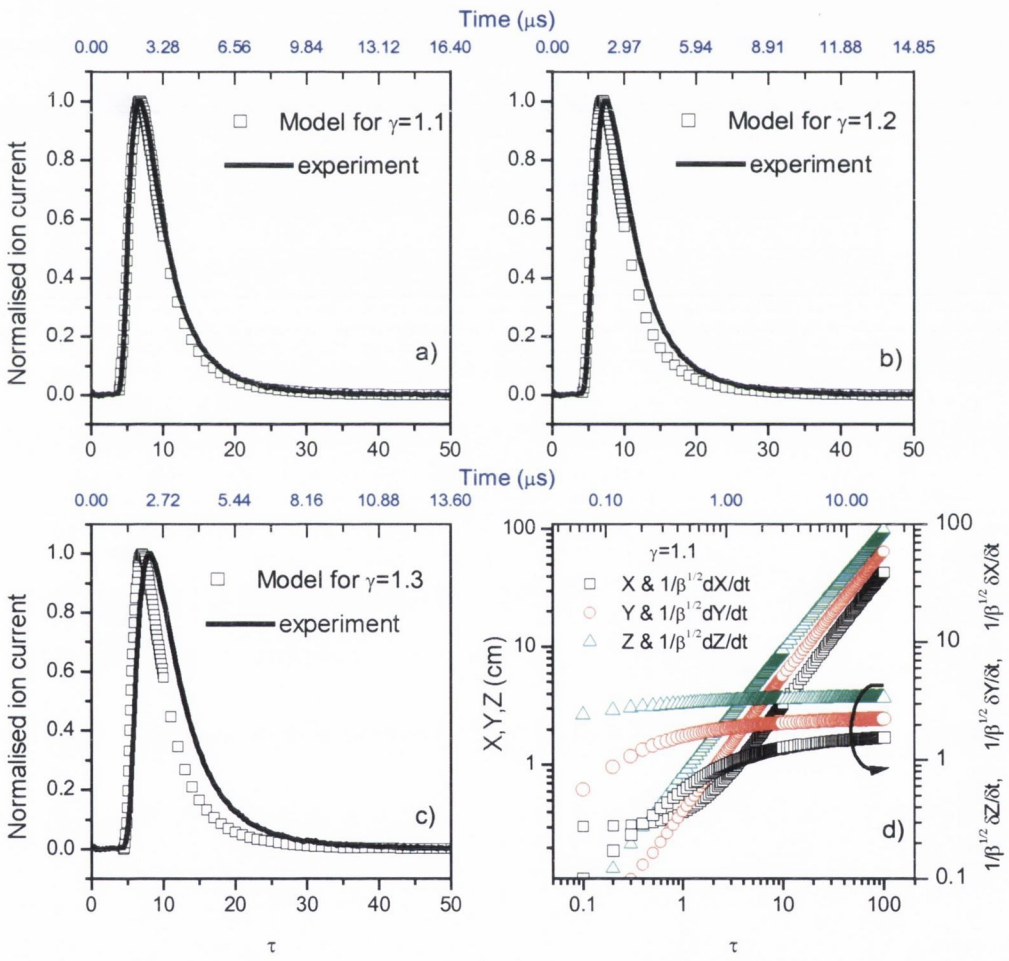

Figure 2.2. In a),b) and c) comparison of the particle flows obtained from the model for different γ values and the ion current measured experimentally is shown. In all cases the ion current was measured at 2.6 cm from the target surface in vacuum. Top axes are the real time and bottom dimensionless time. In d) the results of the numeric solution of Eq.2.7. are presented.

Using this γ value, the total initial energy of the plasma was estimated from Eq. 2.9, obtaining $E=0.053$ J, which is a reasonable result if we take into account the energy losses during the evaporation of the material. Here, it was assumed that the energy required for evaporation of the target material is the sum of the energy expended in heating up the material E_{heat} and the vaporization energy E_{vap}. Thousands of degrees Kelvin are temperatures typically reached on the target material during PLD process. For ZnO at the pressures used in this thesis, vaporization temperatures are in the range of 1000 to 1500 K [Searcy, et al., 1970].

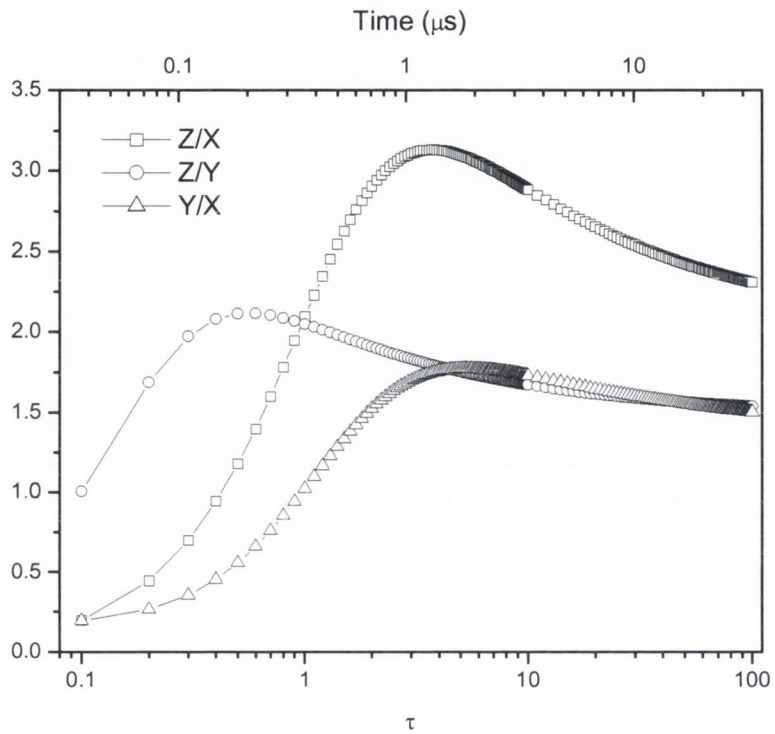

Figure 2.3. The time dependence of the Z/X, Z/Y and Y/X values. Note that at about 0.3 μs, the dimension of the plasma in the Y direction is greater than the dimension in the X direction i.e. there is a rotation of the semi-axes of the ellipsoid.

The energy needed to bring a certain mass of material at room temperature to the above mentioned temperatures can be estimated as $E_{heat} = mc\Delta T$; with $c = 0.5$ $JK^{-1}g^{-1}$ and a mass of 1.6 μg, which was the average evaporated mass per pulse, a value of $E_{heat} = 0.001$ J is obtained. Using 464 kJ mol^{-1} as the vaporization energy per mol [Searcy, et al., 1970] and knowing the number of moles in the evaporated mass (1.23 x 10^{-8} mol of ZnO), the energy expended for the vaporization will be $E_{vap} \sim 0.006$ J. The total energy required for the evaporation is then ~ 0.007 J, adding this value to the energy obtained from the model (0.053 J) gives a total energy of 0.06 J which

was the average energy used in the experiments. In both Figures 2.3 and 2.4 the so called "flip over" can be observed. After a period of time, hundreds of nanoseconds for this case, following the initiation of the plasma expansion, the dimension of the plasma in the *Y-Z* plane is grater than in the *X-Z* plane. The angular distribution is broader in the *Y-Z* plane, which is the plane of the semi-minor axis of the laser spot (see Figure 2.1).

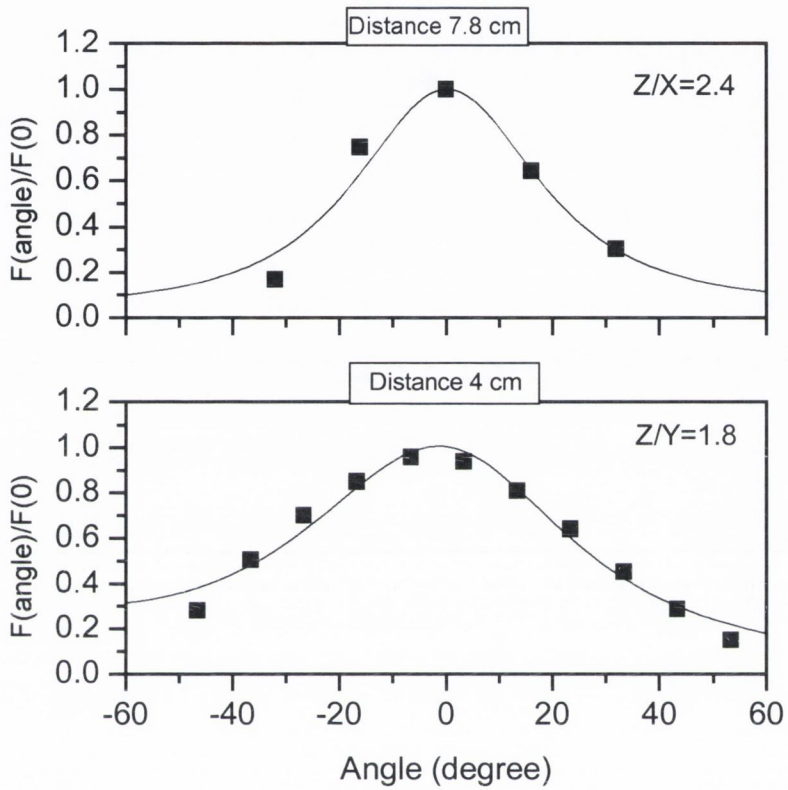

Figure 2.4. Ion angular distribution, measured by a Langmuir probe at different angles with respect to the plasma expansion axis. Top: at a distance from target of 7.8 cm in the x-z plane. Bottom: at a distance of 4 cm and in the y-z plane. Squares are experimental values and solid lines are the fits obtained using Eq. 2.11.

2.2 Expansion in a gas environment

2.2.1 Overview

Under this condition the analysis of the plasma expansion is definitively more complex than the vacuum case. Now the expanding plasma particles will interact with the molecules of the gas, new processes of energy exchange appear speeding up the reduction of the total energy of the expanding plasma. Both elastic and inelastic interaction probabilities are related to the relative kinetic energy of the interacting

particles; for steady plasmas in equilibrium and when the most important interactions are those in which electrons are involved, it will suffice to know the electron temperature. None of the latter conditions are completely fulfilled in a PLD process. Not only have the transient properties of the laser-produced plasma compromised the possibility of reaching equilibrium over the entire expansion but now other important interactions are present, i.e. chemical reactions involving ions and the background gas species (molecules, atoms, ions, etc.). However interactions of electrons with the background gas play an important role in producing ionised or exited species which increases the probability of the desired reaction with ions. The characterization of the electron temperature will be dealt with in the next chapter.

In supersonic expanding plasmas, as developed during PLD, translational energies are greater than the internal energies of the ions; from this the importance of being able to characterise the plasma expansion is evident. Depending on the pressure of the gas, plume splitting and total braking of the expansion occurs. Plume splitting is characterised by the detection of two peaks in TOF studies of the plasma flow. In general terms the explanation for such a splitting has been attributed to the existence of an energetic component of the plasma particles which travel through the gas background suffering little or no collisions while a slow component is formed after it couples with the gas background losing momentum and decelerating its flow. After a period of time the two components will be spatially separated. However, in terms of a theoretical explanation things are not so clear. Wood and Geohegan [Wood, et al., 1998] explained the process using a simple theory in which the particles were distributed within the plasma plume depending on their energy after scattering by elastic collisions with the gas background. Similar results using the collisional approach in Monte-Carlo simulation were reported by Sushmita et al. [Sushmita, et al., 2001]. In the development of a model for the dynamics of laser produced plasmas into ambient gases, Bulgakov et al. [Bulgakov, et al., 1995] related the splitting to oscillations that occur in the plasma as different secondary shock waves travel within it. However, while splitting due to such a process was detected at distances of 2-4 cm from the target for a pressure of 40 Pa, the time scale was in the order of a hundreds of microseconds, which is much greater than the results presented here.

In general both features, plume splitting and plasma deceleration, are related with the appearance of both a shock wave and a contact front. The shock wave is the propagation of a perturbation created by the sudden impact of the expanding plasma

with the gas background. It defines a boundary layer separating the unperturbed gas in front of the shock wave from the gas that went through this layer and is perturbed. The contact front, then, establishes a boundary between this perturbed gas and the plasma.

The formation and propagation of shock waves has been widely studied [Sedov, 1959;Zel'dovich, et al., 1966]. It is well known that the formation of such a feature is related to the ratio of the pressure (density) of the perturber and the gas and that the speed at which it propagates through the gas is defined by the thermodynamic properties of the gas. On the other hand, a full formulation has been given in which parameters such as pressure, density and temperature of the perturbed gas behind the shock wave are expressed as a function of the speed at which this wave propagates through the gas. A more specific work on shock waves developed for the modelling of strong explosions [Sedov, 1959] has been widely used for the description of the laser produced plasmas [Geohegan, 1992a;Gupta, et al., 1991;Harilal, et al., 2003;Jeong, et al., 1998b;Misra, et al., 1999;Gonzalo, et al., 1997]. The justification for such an approach can be understood by analysing the basic assumptions in the strong explosion theory [Sedov, 1959]: (i) a large amount of energy E_s is released instantaneously from a small (negligible) volume, (ii) the mass of the energy source m_s is negligible compared with the mass of the gas background swept by the shock wave and (iii) the pressure exerted by the explosion over the gas should be greater than the pressure in the unperturbed background gas. The first assumption is generally fulfilled for the energies and laser spot size used in laser ablation processes. However, the second, strictly speaking, is not fulfilled unless a very small amount of the ablated material is removed or the plasma has expanded over a volume for which the mass of the swept gas is greater than the ablated mass. A more fundamental problem arises from the fact that this model describes the propagation of a shock wave, which experimentally is difficult to measure. The remainder of this section will be devoted to the analysis of the use of shock wave theory for laser produced plasmas, identifying both regions of applicability and plasma measurable parameters which could be used not only for a post experiment plasma characterization but also in predicting its characteristics.

2.2.2 Sedov-Taylor model

The Sedov-Taylor (S-T) theory defines the shock position R by:

$$R = \varepsilon_0 \left(\frac{E_s}{\rho_0} \right)^{\frac{1}{(2+\upsilon)}} t^{\frac{2}{(2+\upsilon)}}$$
$$\varepsilon_0 = 1.08 \left(\frac{\gamma+1}{2} \right)^{\frac{2}{(2+\upsilon)}} \tag{2.12}$$

where ρ_0 is the density of the gas background and γ its specific heats ratio. The parameter υ will take values of 1, 2 or 3 for expansions with planar, cylindrical or spherical symmetry. The flow speed U_{bs}, density ρ_{bs}, peak pressure P_{bs} and temperature T_{bs} behind the shock (bs) are given by:

$$U_{bs} = \frac{2}{\gamma+1} \frac{dR}{dt}$$
$$\rho_{bs} = \frac{\gamma+1}{\gamma-1} \rho_0$$
$$P_{bs} = \frac{2}{\gamma+1} \rho_0 \left(\frac{dR}{dt} \right)^2 \tag{2.13}$$
$$T_{bs} = \frac{2\gamma}{(\gamma+1)} \left[\frac{(\gamma-1)}{(\gamma+1)} M^2 + 1 \right] T_0$$

where $M = \dfrac{dR/dt}{\mathrm{v}_{sound}}$ is the Mach number with $\mathrm{v}_{sound} = \left(\gamma \dfrac{P_0}{\rho_0} \right)^{\frac{1}{2}}$.

Until this point the existence of the shock wave has been assumed. A shock wave is formed only if the shock wave thickness (Δ) is greater than the diffusion length (l_{Diff}) of the gas molecules through the perturbed region. These two parameters are defined as follows:

$$\Delta = \frac{\gamma-1}{\gamma+1} \frac{R}{3}$$
$$l_{Diff} = 2\sqrt{Dt} \tag{2.14}$$

where D is the diffusion coefficient within the shock region and t is the diffusion time. The diffusion coefficient is defined as follows [Dyer, et al., 1990]:

$$D = D_0 \left(\frac{T_{bs}}{T_0} \right)^{0.75} \left(\frac{\rho_{atm}}{\rho_{bs}} \right) \tag{2.15}$$

In practice this model is commonly used to extract the plasma expansion velocity by fitting curves of shock position versus time measured during the experiment. Langmuir probe and ICCD images are the main characterization techniques used to measure the experimental values.

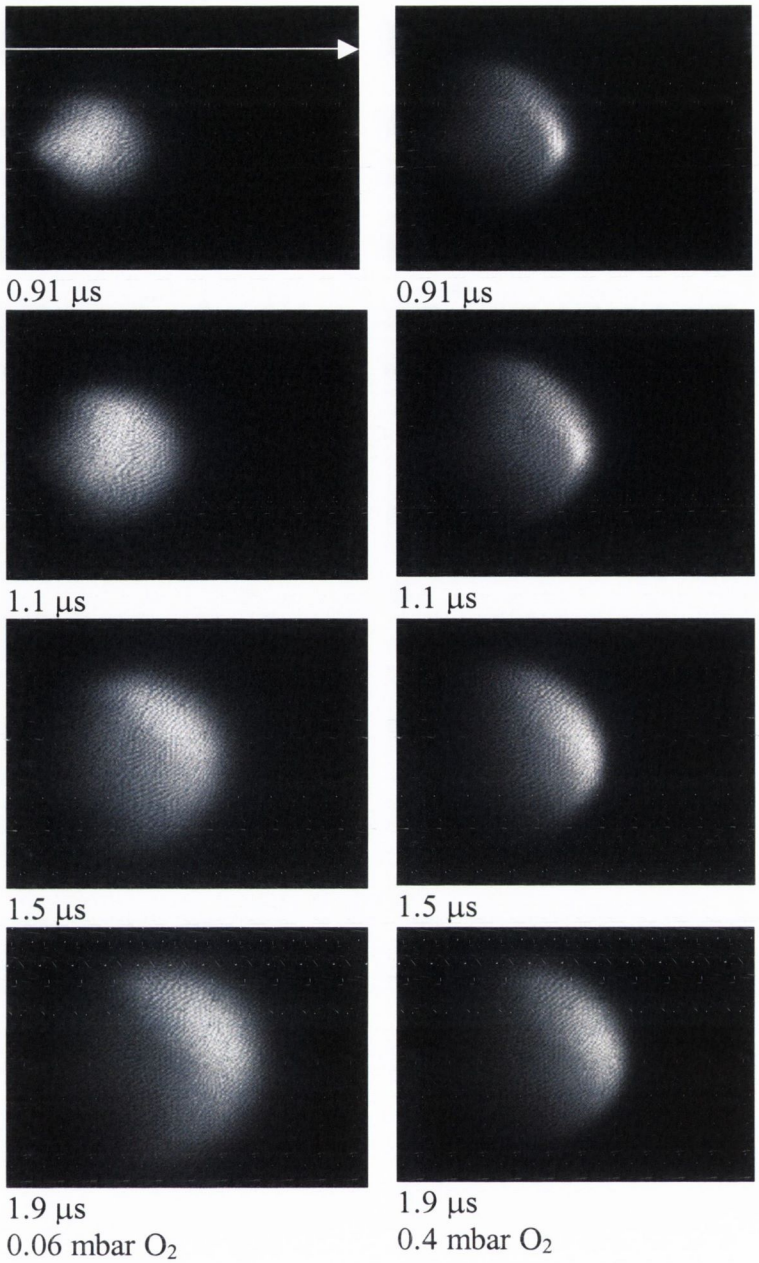

Figure 2.5. Images acquired for different time delay as the plasma expands in gas background at 0.06 mbar and 0.4 mbar. The direction of the expansion is denoted on the top-left image with length scale of 4 cm. The target position is the left border in all cases. Images are normalised to their maximum intensity.

Figure 2.5 shows time resolved images, which were recorded using the ICCD camera as explained in Chapter 1. The images were recorded for two different pressures of oxygen, 0.06 mbar and 0.4 mbar. The low pressure case is characterised by a broader and homogeneous distribution of the hotter regions in the plasma plume. As the plasma expands, the hotter region starts concentrating toward the leading edge of the plume. The higher pressure case shows the presence of the

confined region occurring earlier in time during the expansion. For longer periods of time this region begins to broaden. For both cases the appearance of such a region defines the formation of a contact front, which in turn is related to the formation of a shock wave.

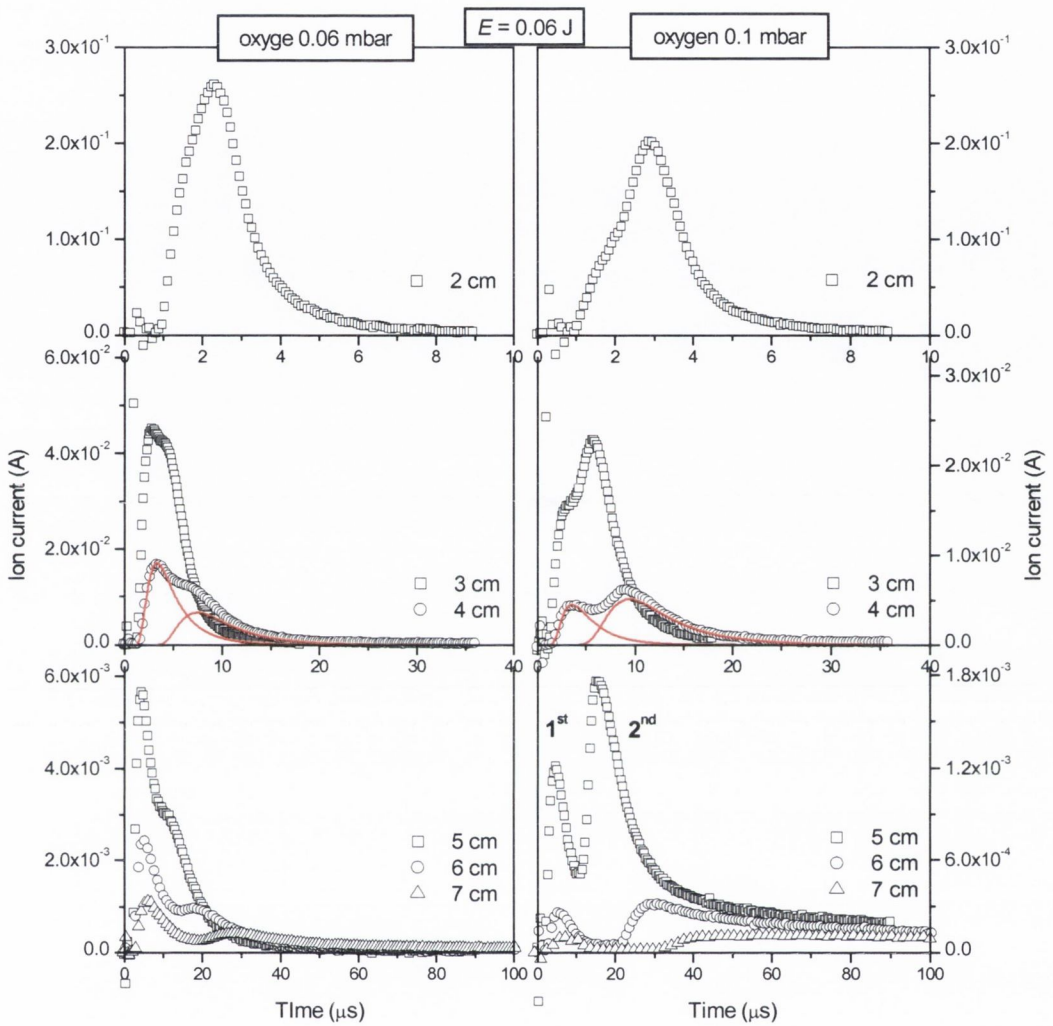

Figure 2.6 Ion currents measured in the TOF study of the plasma expansion at 0.06 mbar and 0.1mbar of oxygen. Two peaks are detected. The first peak expands through the gas background with a vacuum-like constant velocity, while the second peak decelerates. First and second peaks are labelled in the right-bottom graph for clarity. Examples of the fits (red lines) are presented for TOF measured at 4 cm for both pressures.

Figure 2.6 shows the measured TOF using the Langmuir probe for the 0.06 and 0.1 mbar oxygen pressures. The plume splitting is clearly present at all distances and at the two pressures, though its resolution increases with the increase of both distance and pressure. For clarity the peaks are labelled in the bottom-right graph. Figure 2.7 shows the TOF of the ion signals as measured using the Langmuir probe at a distance

of 2, 3 and 4 cm from the target surface and at a pressure of 0.4 mbar of oxygen. At this pressure plume splitting is no longer detected. There is a stronger peak value reduction with increasing distance and a broadening of the distribution.

In order to extract the profiles of the curves which convolve to form the observed TOF, the curves were fitted using shifted half Maxwellians (Figure 2.6) and then both front and peak arrival time were extracted. The plots of the arrival time at each position for both peaks at the three different pressures are shown in Figure 2.8. As mentioned before, the first peak shows a TOF which indicates a linear vacuum-like flow. The velocities, in each case extracted from the slope of the plots, were similar for both pressures and half the value obtained for the in-vacuum expansion in the previous section. The second peak shows a decelerated expansion with a greater deceleration at the higher pressure.

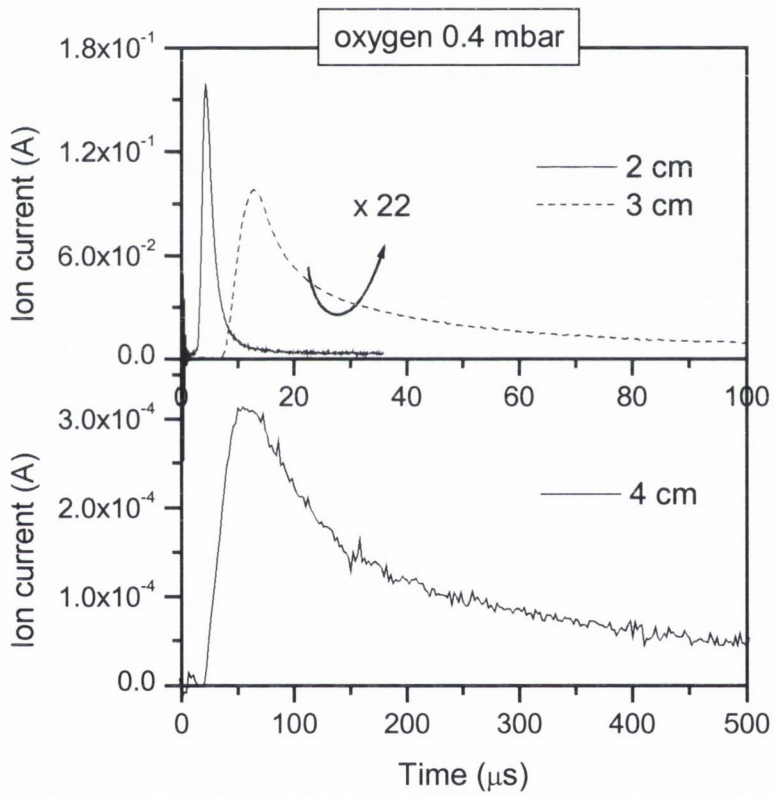

Figure 2.7. Ion currents measured in the TOF study of the plasma expansion at 0.4 mbar of oxygen. The expansion is characterised by a strong deceleration and a broadening of the signals. Note that the signal corresponding to 3 cm has been increased for clarity in the plots.

The Sedov-Taylor model, equation 2.13, was used to fit the data extracted from both the ion signals and the ICCD photographs.

As mentioned above the Figure 2.8 corresponds to the data extracted using the Langmuir probe. Dashed and dotted lines were obtained by setting fixed values of both E_p and ρ_0 to 0.053 J and $9x10^{-5}$ kg/m^3 respectively allowing the fitting procedure to find the best ε_0 and υ. The values of E_p and ρ_0 correspond to the energy predicted by the Anisimov model in the previous section and the background gas density for a pressure of 0.06 mbar respectively. The solid lines were obtained by setting fixed values of parameter ε_0, choosing $\gamma = 1.28$, and $\upsilon = 3$ corresponding to a spherical symmetry as explained before.

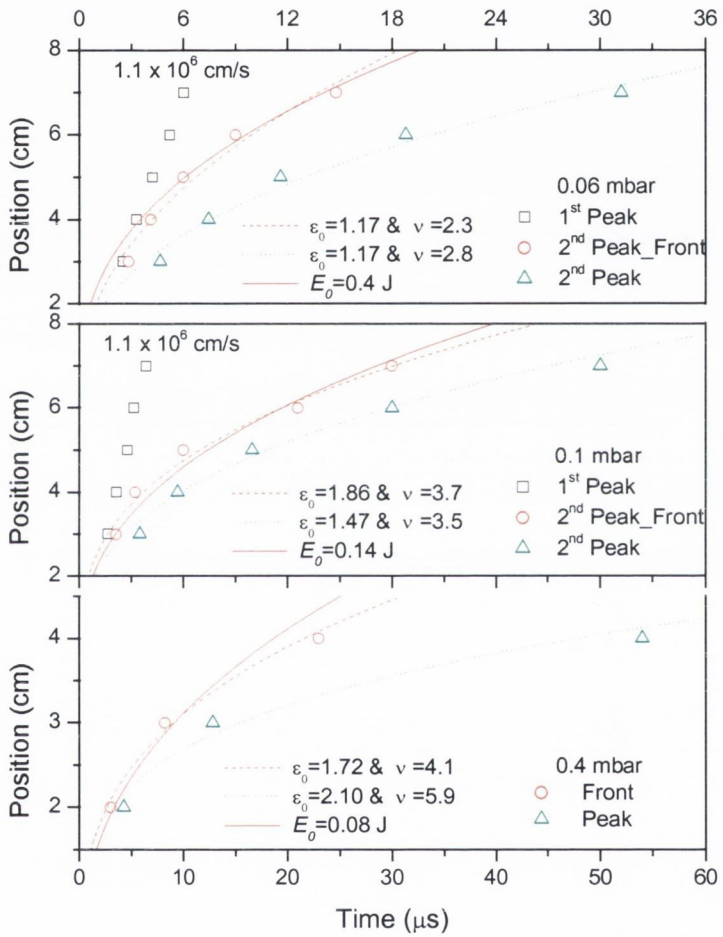

Figure 2.8. Plots of the arrival time of ion TOF at each position for both peaks at 0.06, 0.1 and 0.4 mbar of oxygen. For 0.06 and 0.1 mbar, where plume splitting is observed, the first peak shows a vacuum-like expansion. Both front and peak arrival times at each position show a decelerated expansion. Dashed, dotted and solid curves represent the fits performed using equation 2.12.

The analysis performed to the data extracted using the ICCD camera is presented in the Figure 2.9. The data represents the position of the front edge of the images

presented in Figure 2.5. The fitted curves were obtained following the same idea as for the fit of the data presented in Figure 2.8.

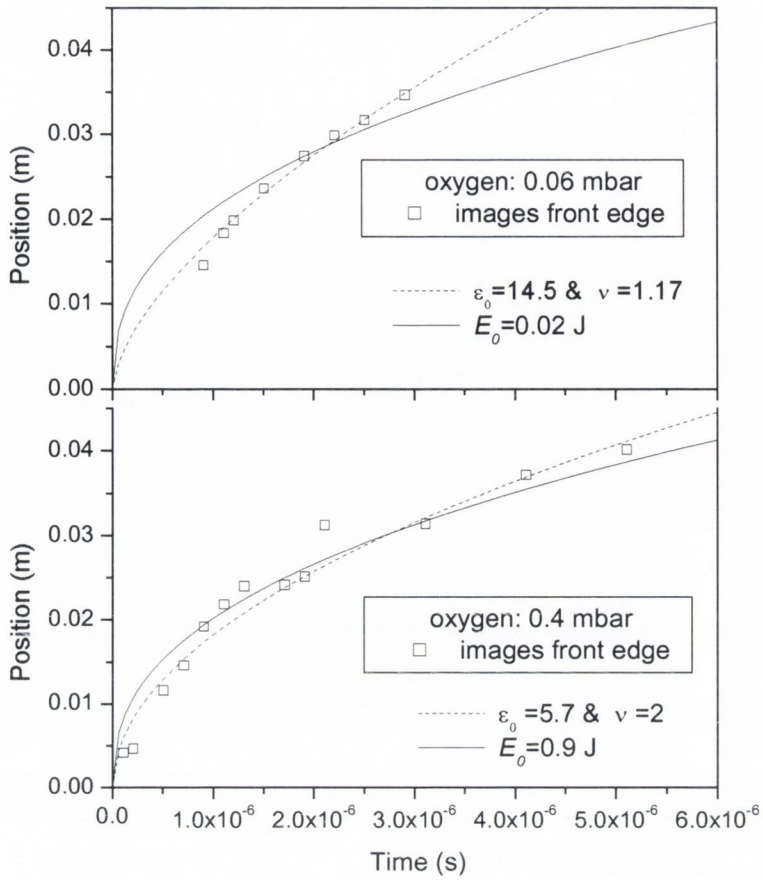

Figure 2.9. Plots of the arrival time of the images front edge at each position for both pressures 0.06 and 0.4 mbar of oxygen. For the two background pressures the expansion is decelerated. Both dashed and dotted fit lines were obtained following the same procedure as explained for Figure 2.8.

In an overview of the results presented in both Figure 2.8 and 2.9 it can be corroborated that in general the expansion of laser produced plasmas is satisfactorily reproduced by a general shock wave law of the type of equation 2.12. However a close comparison reveals that different values of the parameters of the equation are obtained for the same experimental data. At 0.06 mbar of oxygen background, Figure 2.8, the fit of the front position (dashed line) suggests that the plasma expands with a cylindrical symmetry while the fit of the peak position (dotted line) is closer to a spherical one. Similar problems arise if comparing the previous mentioned results with the 0.06 mbar of oxygen case but for the data measured using ICCD images (Figure 2.9). These last results pose the question as to whether the reason for these inconsistencies is due to the non fulfilment of the basis of this theory, presented earlier in this section, or simply that, strictly, none of the used techniques are able to

characterise the developed shock front. In trying to answer this question another model was used.

2.2.3 Freiwald-Axford model

This model, a modification of the Sedov-Taylor theory, was developed by Freiwald and Axford [Freiwald, et al., 1975] with the aim of taking into account the mass of the explosion source. Their article showed that this modification is of particular importance at early stages of the plasma expansion. In what is, at least from the literature review performed for this thesis, the only work referring to this model, Kapitan and Coutts [Kapitan, et al., 2002] used it to explain the deviations of the S-T theory in describing shock waves produced in laser ablation processes. One of their main conclusions was that the model could be applied to describe processes carried out in background pressures >1 mbar. However, while their work followed the traditional approach of relating the plasma expansion to the properties of the gas background, in this thesis another approach is proposed.

Freiwald et al. took into account that a portion of the total energy E_p, released in the explosion is converted into both kinetic and internal energy of the source mass and not only in perturbing the gas through a shock wave. During the formulation an average source mass density of the following form was defined, $\overline{\rho}_p \equiv \rho_p \left(\frac{R_p^3}{R^3} \right)$, which implies the assumption that the radius of the plasma $R_p \approx R$, the shock wave radius. This assumption supports the idea of firstly, using the model to describe the propagation of the plasma itself and secondly to use the plasma gamma value instead of that of the gas background. As a result, an equation relating the energy of the source (initial plasma energy E_p), its density ρ_{p0}, plasma front position R_p and time was obtained:

$$E_p^{1/2} t = C_1^{1/2} \left(\frac{C_1}{C_2} \right)^{1/2} \left(0.455 F\left(\phi, 75^o\right) + \frac{2}{5} R_p \left(\frac{C_2}{C_1} \right)^{1/3} \left(1 + R_p^3 \frac{C_2}{C_1} \right)^{1/2} - 0.842 \right) \tag{2.16 a}$$

$$C_1 = \frac{8.37}{(\gamma+1)^2}\rho_{p0}R_{p0}^3 \qquad C_2 = 8.37\rho_0\left(\frac{2}{(\gamma+1)^2}+\frac{1}{\gamma^2-1}\right)$$

$$\phi = \cos^{-1}\left(\frac{0.73 - R_p\left(\frac{C_2}{C_1}\right)^{1/3}}{2.73 + R_p\left(\frac{C_2}{C_1}\right)^{1/3}}\right) \qquad (2.16\text{ b})$$

where R_{p0} is the radius of the volume of the plasma before the explosion and the function $F(\Phi,75^\circ)$ is the elliptic integral of first kind. Knowing the values of the energy, density and radius of the plasma before starting the expansion the position of the plasma front as a function of time can be obtained by numerical evaluation. The plasma front velocity is obtained as follows:

$$\left(\frac{dR}{dt}\right)^2 = \frac{E_p}{\frac{16.75}{(\gamma+1)^2}\rho_0 R^3 + \frac{8.37}{(\gamma+1)^2}\rho_p R_p^3 + \frac{8.37}{\gamma^2-1}\rho_0 R^3} \qquad (2.17)$$

Once the plasma front velocity is known the rest of the parameters can be calculated using Eq. 2.13.

Figure 2.10 shows the results (solid lines) of the numerical calculation performed using equation 2.16 for both 0.06 and 0.4 mbar pressures. In the calculation the values of the energy and γ obtained from the Anisimov model (see previous section) were used as input data. Both results show good agreement in describing the plasma front position as extracted from the ICCD images.

2.2.4 Discussion

In corroborating the correctness of the previous results the following phenomenological analysis was used. As has been reported [Predtechensky, et al., 1993] when the plasma expands in the presence of a gas background there exists a maximum distance which it will be able to reach. This is due to the reduction of its internal energy as a consequence of the work developed in displacing the surrounding gas. At this distance the pressure exerted by the plasma equals that of the gas background.

Two different models were used to estimate the maximum distance for the experimental conditions presented in this work, the so called drag model developed

by Goehegan et al [Geohegan, 1992b] and a model developed by Predtechensky et al. [Predtechensky, et al., 1993].

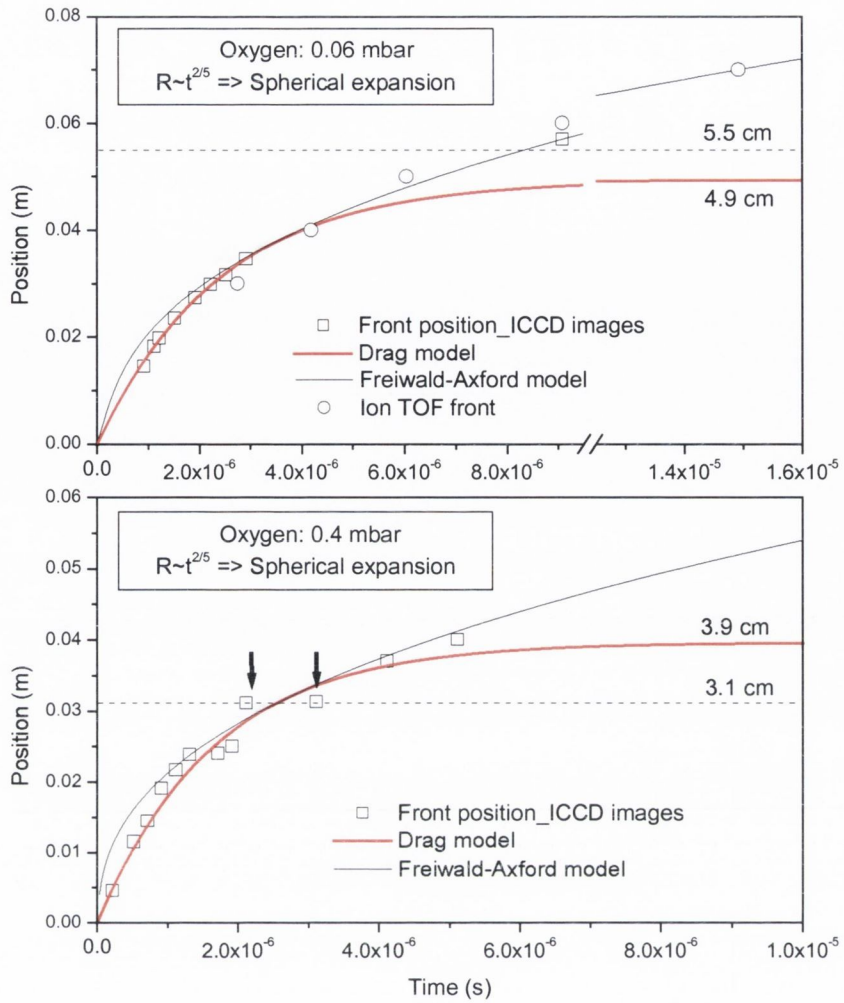

Figure 2.10. Solid lines represent the results of the numerical calculation preformed using equation 2.16. Red lines represent the Drag model and dashed lines maximum position as predicted by equation 2.19. Squares represent the front edge in the ICCD images presented in Figure 2.5. Circles (top figure) represent the arrival times of the 2nd peak fronts from the ion TOF at 0.06 mbar as in Figure 2.8.

The drag model is defined by:

$$R = R_{\max}\left(1 - e^{-\beta t}\right)$$
$$R_{\max} = \frac{v_0}{\beta} \qquad (2.18)$$

where v_0 is the initial velocity of the plasma expansion and β is a slowing coefficient. Predtechensky model is defined by:

$$R_{\max} = \left(\frac{2ME_p}{\pi^2 \rho_g P_g} \right)^{1/6} \qquad (2.19).$$

The values for the maximum distance as predicted from each model are indicated in Figure 2.10. It can be observed that the drag model allows not only the prediction of the maximum travel distance; it also describes the plasma expansion. From the Figure 2.10 it seems that the Predtechensky model gives more accurate results in the calculation of the maximum position. In this figure the two arrows mark two data points which for the same distance were measured at different times with an interval of 1 μs. The data points correspond to a distance of ~ 3 cm which coincides with the value predicted by this model.

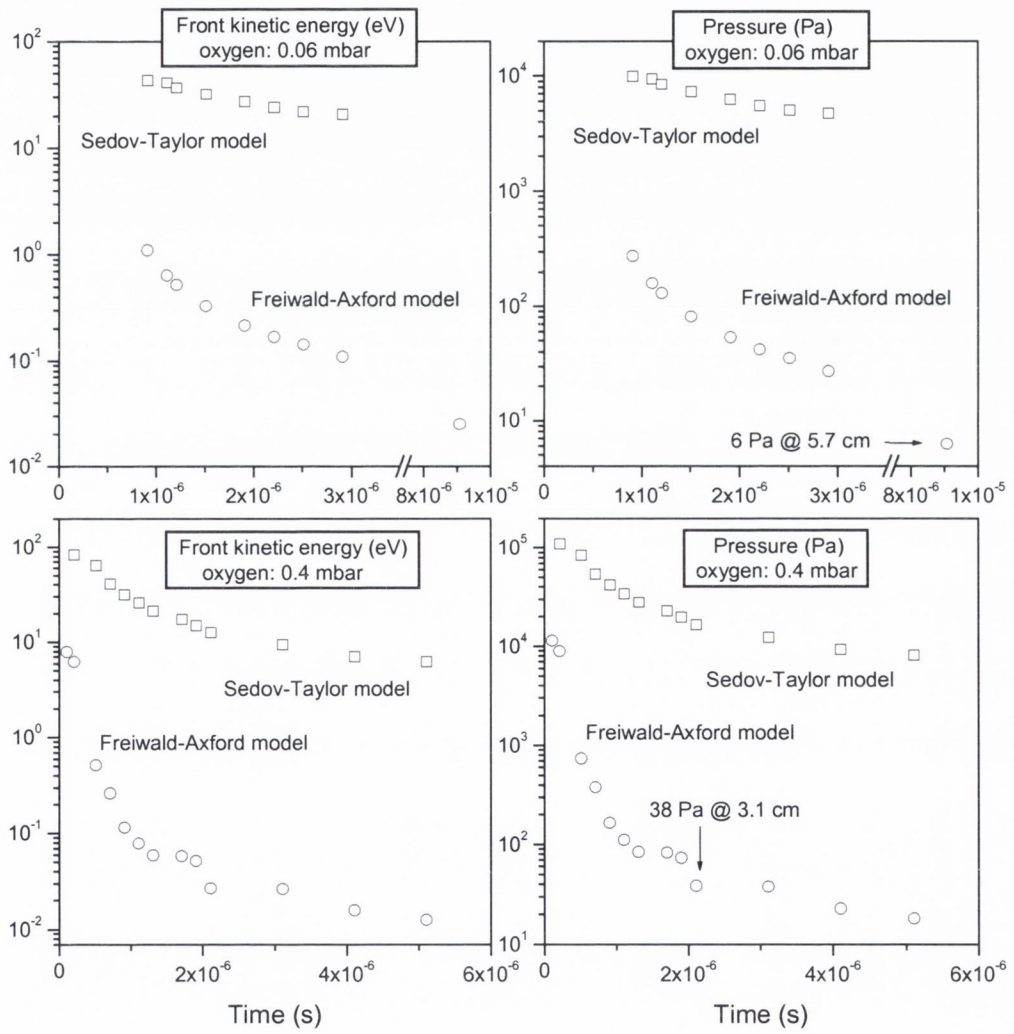

Figure 2.11. Values of pressure and front kinetic energy as predicted by both the S-T and F-A models. Left column presents the kinetic energy in eV and the right column presents the pressure in Pa. Top row for a gas background pressure on 0.06 mbar and bottom 0.4 mbar.

Figure 2.11 shows the values of the front kinetic energy and pressure exerted over the gas background as predicted by both the S-T and the F-A models. In the case of the S-T model the front velocities were calculated by the derivative of the expression obtained from the fit of Figure 2.9 (dashed line). For the F-A model the front velocities were calculated using equation 2.17. In both models after the front velocities were known, the pressures were calculated from equation 2.13. The difference between values predicted for each model is of several orders with the S-T model predicting the higher values. The pressure plot shows that for both gas backgrounds the F-A model predicts with good agreement the position at which the plasma exerted pressure equals that of the gas surrounding it. If the value for the maximum expansion distance is correct, it is to be expected that from this point on the plasma expands similarly to the spreading of a cloud of ions by diffusion through a gas.

The ionic number density n at a radius r from the release point and time t can be defined as follows [Mason, et al., 1988]:

$$n = \frac{N_0}{\left(4\pi D(t-t_0)\right)^{3/2}} e^{-\frac{r^2}{4D(t-t_0)}} \qquad (2.20)$$

where N_0 is the initial number of ions at the point where the diffusion starts and D is the diffusion coefficient. The parameter t_0 was introduced for fitting purposes to allow for an offset in the initial time.

Figure 2.12 shows the results of the fit performed using equation 2.20 to the ion current measured at 4 cm in an oxygen background of 0.4 mbar. The best values obtained in the fit were r = 1.01 cm and t_0 = 8.66 μs, both in good agreement with the previous models. Note that at this pressure the maximum expansion distance, predicted by both equation (2.19) and the F-A model, was 3.1 cm and that the front arrival time to this distance was 8.2 μs (Figure 2.8). The lack of experimental data in diffusion of zinc ions prevents a comparison with the value obtained for the diffusion coefficient but longitudinal diffusion coefficients of the same order have been reported for ions of elements as heavy as Rb [Mason, et al., 1988].

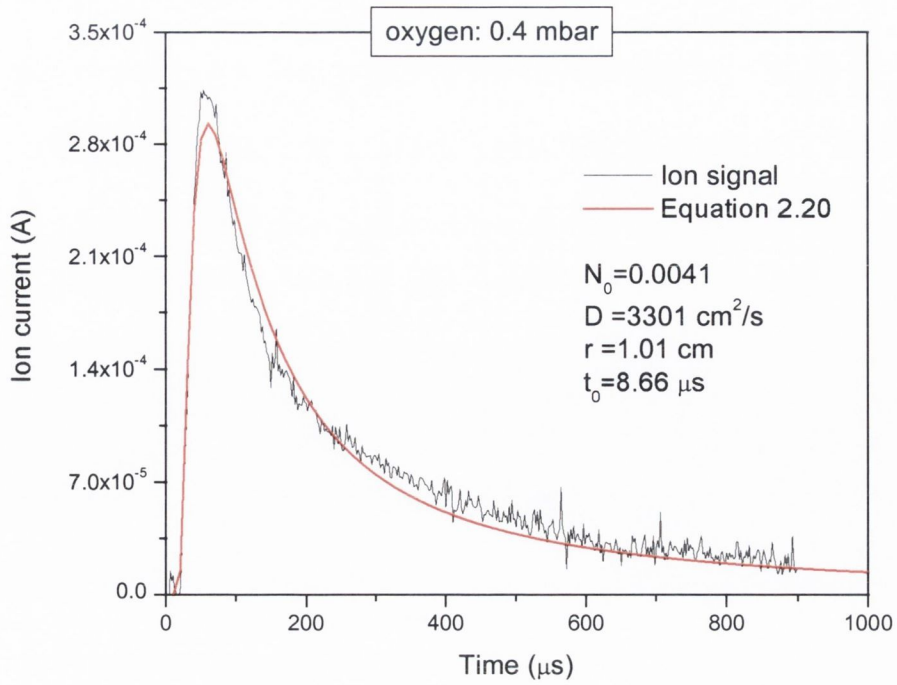

Figure 2.12. Shows the ion current signal measured at 4 cm from the target and in 0.4 mbar of oxygen background. Dotted line represents the fit obtained by using equation 2.20.

In section 2.2.2 inconsistencies were found among results from using the S-T to fit data belonging to the front of the ion signal or its peak values (Figure 2.8). The same was observed when comparing results from using ICCD images front edge data (Figure 2.9) and any of the two options in ion signals. In section 2.2.3 (Figure 2.10) the F-A model described successfully both ICCD images front edge data and ion signal front arrival times but only at 0.06 mbar oxygen pressure. Although no ICCD front edge data was available to compare with, the F-A model was used to model the front expansion as monitored using the Langmuir probe but after increasing the laser fluence to 2.5 J/ cm^2. For this laser fluence the mass loss measurements gave ~ 4 μg per pulse. The in vacuum plasma expansion velocity was measured to be the same as for the previous used laser fluence so $\gamma = 1.1$ and an initial plasma energy $E_p = 0.12$ J was used as input data. This value of energy comes after taking into account the energy released during the vaporization of the above mentioned mass of material, using the same procedure as explained in section 2.1.2.

Figure 2.13 shows the results of the numerical calculation (solid line) together with the plot of the arrival time at each position of the front in the ion signals. The dashed line represents the maximum travel distance from equation 2.19. A

reasonable agreement can be observed for the plasma front positions and the predicted position at which pressure equals that of the background gas. Again deviations appeared when applied to the 0.4 mbar case.

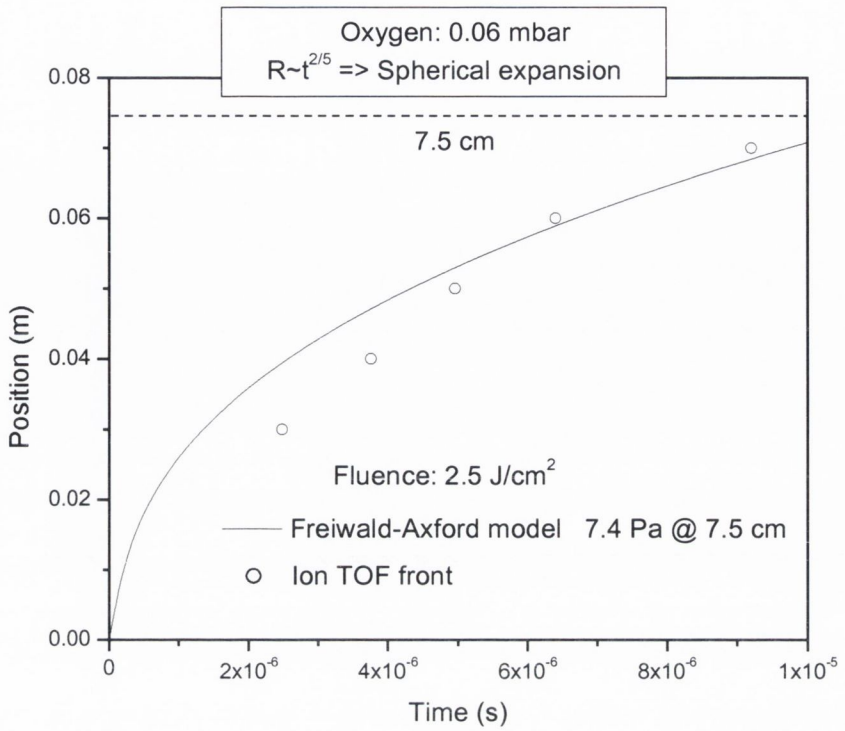

Figure 2.13. Result from using the F-A model (solid line) to predict plasma expansion in 0.06 mbar of oxygen background but after increasing the laser fluence to 2.5 J/cm^2. Circles represent the front arrival time at each position as measured using a Langmuir probe.

Although not commented upon, a similar discrepancy can be observed in the data presented by Geohegan et al [Geohegan, 1992b], when applying these two techniques in studying the expansion of laser produced plasmas in presence of a gas background. An explanation for such behaviour is not clear but the coincidence of both techniques at background pressures lower than 0.1 mbar might be related to the strong overlap that still exists between the first and second peak of the plume splitting for the distances and laser fluences presented here. On the other hand at this low pressure neutralization of ions in the contact front might not be as efficient as for higher pressures.

2.3 Conclusions

As far as the results obtained and presented in this chapter, the Anisimov model proved to describe with good agreement the in vacuum expansion and distribution of

laser produced plasmas. This implies that the specific heat ratio value extracted from the model is correct. On the other hand the plasma initial energy calculated with the model was in good agreement with the energy calculated using the reported vaporization energy of the target.

Although in general the standard shock model can be used to fit correctly the experimental data of the position of the plasma expansion in gas background other parameters such as velocity and pressure extracted from it are over estimated.

The use of Freiwald and Axfords theory but with a different approach reproduces with good agreement the experimental data. Firstly, it is not the shock wave but the contact front of the expanding plasma what it is described. Secondly, the plasma gamma value is used instead of the gamma value of the background gas. The velocity and pressure as extracted from it gave the expected values, i.e. at the plasma stopping distance the pressure equals the pressure of the oxygen background and the expansion velocity is less than the sound speed in the oxygen background. This approach allowed the use of input data obtained from the Anisimov model which implies that predictions of the plasma expansion in a gas background can be done by characterizing its expansion in vacuum. This means a simpler characterization process.

Finally, it should be mentioned that it is not correct the use of Langmuir probe for the description of both the shock front and the contact front developed during the expansion of laser produced plasmas in a gas background. On the other hand time resolved images recorded using an ICCD reproduce correctly the development of the contact front. Although in the present thesis the shock wave was not detected, it has been reported [Gupta, et al., 1991] that ICCD can also be used to study the shock wave.

References

Linlor, V. I., *Physical Review Letters*, **12**, p. 383 (1963).

Bobin, J. L., Y. A. Durand, P. P. Langer, et al., *Journal of Applied Physics*, **39**, p. 4184 (1968).

Cowin, J. P., D. J. Auerbach, C. Becker, et al., *Surface Science*, **78**, p. 545 (1978).

Namiki, A., T. Kawai, Y. Yasuda, et al., *Japanese Journal of Applied Physics*, **24**, p. 270 (1985).

Kelly, R. and R. W. Dreyfus, *Nuclear Instruments & Methods in Physics Research, Section B*, **B32**, p. 341 (1988).

Kelly, R., *Proceedings of the SPIE - The International Society for Optical Engineering*, **1056**, p. 258 (1989).

Bulgakov, A. V. and N. M. Bulgakova, *Journal of Physics D (Applied Physics)*, **28**, p. 1710 (1995).

Jeong, S. H., R. Greif, and R. E. Russo, *Applied Surface Science*, **127-129**, p. 177 (1998a).

Leboeuf, J. N., K. R. Chen, J. M. Donato, et al., *Applied Surface Science*, **96-98**, p. 14 (1996).

Anisimov, S. I., B. S. Luk'yanchuk, and A. Luches, *Applied Surface Science*, **96-98**, p. 24 (1996).

Hansen, T. N., J. Schou, and J. G. Lunney, *Applied Physics A*, **A69**, p. 601 (1999).

Searcy, A., D. V. Ragone, and U. Columbo, (Wiley-Interscience, New York, 1970).

Wood, R. F., J. N. Leboeuf, D. B. Geohegan, et al., *Physical Review B (Condensed Matter)*, **58**, p. 1533 (1998).

Sushmita, R. F. and R. K. Thareja, *Applied Surface Science*, **177**, p. 15 (2001).

Sedov, L. I., *Similarity and dimensional methods in mechanics* (New York :Academic Press, 1959).

Zel'dovich, Y. B. and Y. P. Raizer, in *Physics of Shock Waves and High Temperature Hydrodynamic Phenomena* (Academic Press, New York, 1966), Vol. 1.

Geohegan, D. B., *Applied Physics Letters*, **60**, p. 2732 (1992a).

Gupta, A., B. Braren, K. G. Casey, et al., *Applied Physics Letters*, **59**, p. 1302 (1991).

Harilal, S. S., C. V. Bindhu, M. S. Tillack, et al., *Journal of Applied Physics*, **93**, p. 2380 (2003).

Jeong, S. H., R. Greif, and R. E. Russo, *Applied Surface Science*, **127-129**, p. 1029 (1998b).

Misra, A., A. Mitra, and R. K. Thareja, *Applied Physics Letters*, **74**, p. 929 (1999).

Gonzalo, J., C. N. Afonso, and I. Madariaga, *Journal of Applied Physics*, **81**, p. 951 (1997).

Dyer, P. E., A. Issa, and P. H. Key, *Applied Physics Letters*, **57**, p. 186 (1990).

Freiwald, D. A. and R. A. Axford, *Journal of Applied Physics*, **46**, p. 1171 (1975).

Kapitan, D. and D. W. Coutts, *Europhysics Letters*, **57**, p. 205 (2002).

Predtechensky, M. R. and A. P. Mayorov, *Applied Superconductivity*, **1**, p. 2011 (1993).

Geohegan, D. B., edited by E. Fogarassy and S. Lazare (North-Holland, 1992b).

Mason, E. A. and E. W. McDaniel, *Transport properties of ions in gases* (Wiley, 1988).

Chapter 3 Plasma properties

In the previous chapter the plasma expansion was characterized for both the in vacuum case and in the presence of a gas background. Using a gas-dynamic approach the plasma front kinetic energy was described for both conditions.

The present chapter characterizes the internal properties of the plasma. Using emission spectroscopy and Langmuir probe techniques plasma species temperatures and densities are studied.

3.1 Emission spectroscopy

3.1.1 General features

In order to establish a reference for the emission of zinc species the spectra of the laser produced plasma from zinc metal target 99.999 % purity was recorded. In this case the fluence of the laser pulse was 2.5 J/cm^2, at which the presence of transitions of ionized species was detected.

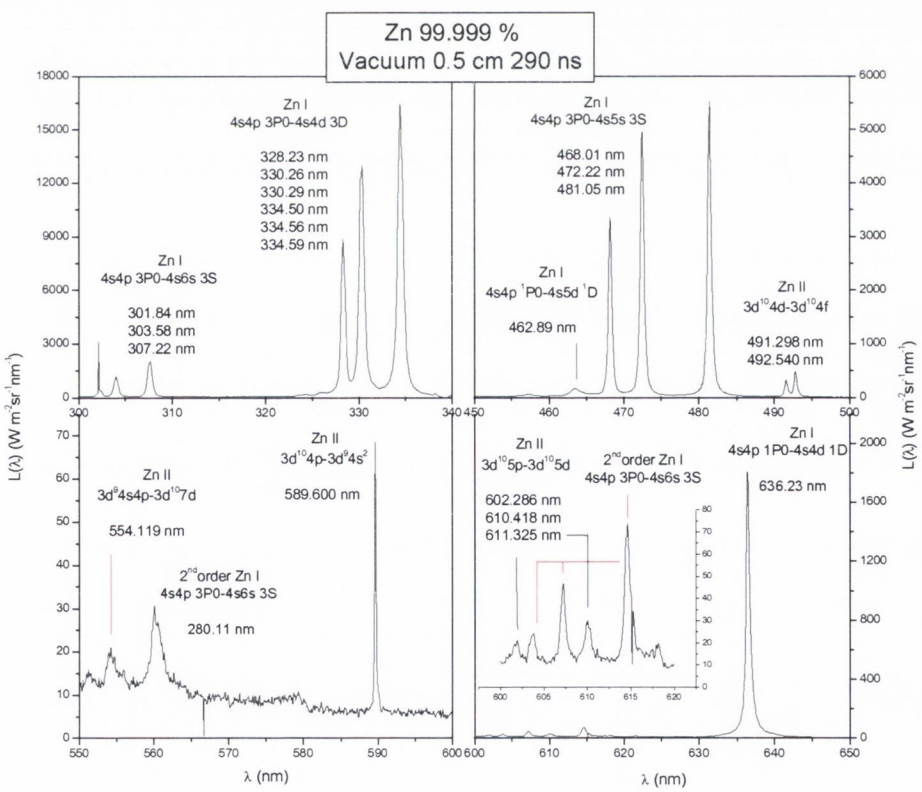

Figure 3.1. Emissions recorded after ablating a (99.999 % purity) zinc target with 2.5 J/cm^2 laser fluence.

Figure 3.1 shows examples of the recorded spectra. The experimental set up and method of acquisition were as explained in Chapter 1.

As the fluence was reduced to 1 J/cm^2, which is the fluence used throughout the thesis, only three of the spectral regions presented in figure 3.1 were studied since no emission was detected in the (500-600) nm region. Figure 3.2 shows an example of the recorded spectra from a ZnO ceramic target for the same delay time and position used for the spectra presented in Figure 3.1.

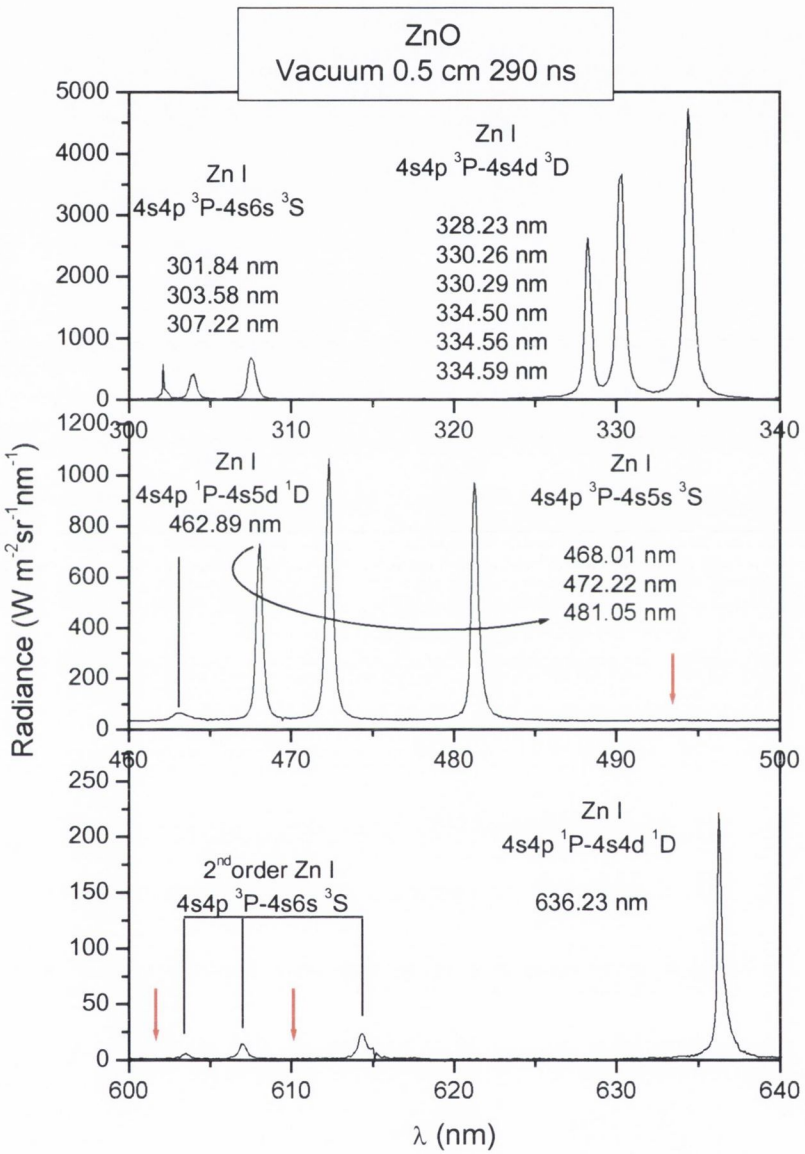

Figure 3.2. Emission spectra recorded after the laser ablation of a ceramic ZnO target. Red arrows indicate the position where transitions belonging to ionized zinc should appear.

From Figure 3.2 it is clear that apart from differences in the line radiances, which will be dealt with later, and the absence of lines associated with ionized species, the

recorded lines coincide with the emissions of zinc species only. No oxygen transitions were detected, even with the introduction of oxygen to a pressure of 0.4 mbar. Figure 3.3 shows the recorded spectra for two different pressures of oxygen at the same position and delay time as Figure 3.2.

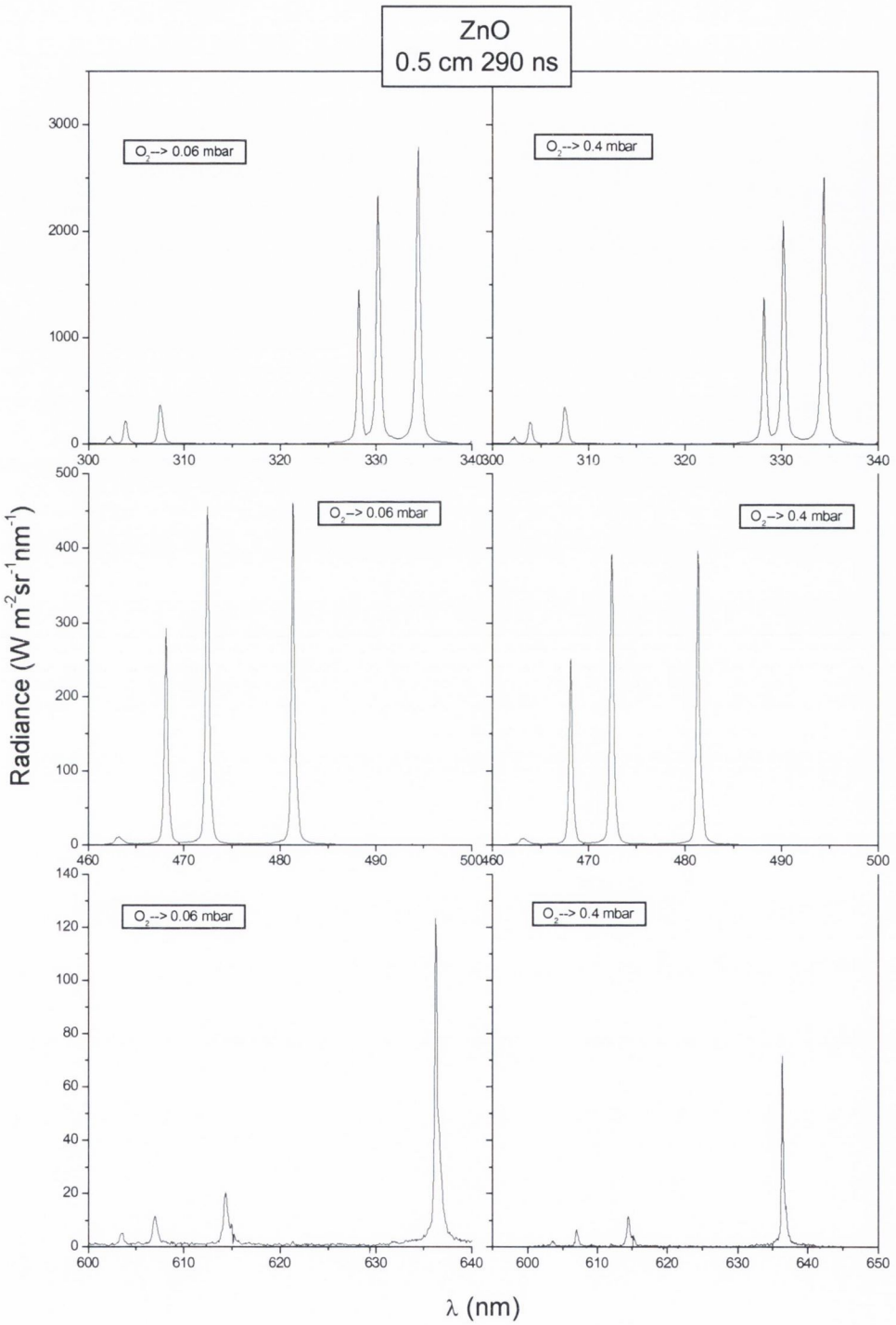

Figure 3.3. Recorded spectra for two different pressures of oxygen.

As in the vacuum case all the detected lines are due to atomic zinc.

Figure 3.4 shows a reduced block diagram of the lines detected.

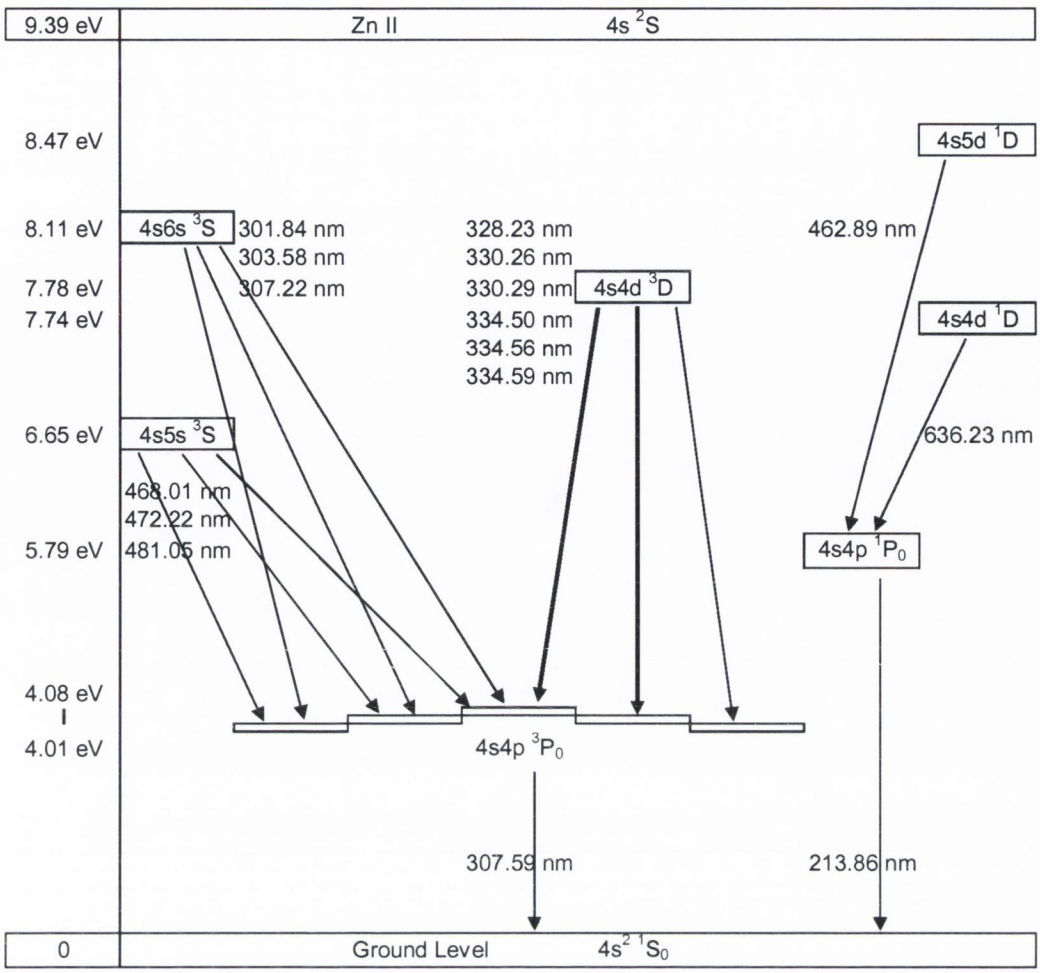

Figure 3.4. Reduced block diagram of the Zn atomic levels. Note the metastable level 4s4p $^3P_0$ has been split for clarity of the drawing.

3.1.2 Plasma parameters extraction

The first step in the analysis was to define whether the plasma fulfils the conditions for local thermal equilibrium. In Chapter 1 the theoretical criteria for the prediction of thermal equilibrium were introduced while in Figure 1.2 the calculated critical densities were plotted. The greatest densities (10^{16} cm^{-3}) are required for the establishment of a LTE in an optically thin plasma, while densities of the order of 10^{14} cm^{-3} are required for the establishment of PLTE of the levels ($n \geq 3$) with the ion ground state. As will be discussed in the next section, Langmuir probe measurements suggests that densities varied from orders of 10^{15} cm^{-3} at positions close (<5mm) to the target to 10^{13} cm^{-3} at 4 cm from the target. This implies that LTE equilibrium can not be reached but a PLTE can be expected.

A second step was to corroborate the presence of PLTE by performing Boltzmann plots. For this the logarithms of the peak radiance of each emission line, each multiplied with the appropriate factors occurring in equation 3.1, were plotted as a function of the energy of their upper energy level. If PLTE is present, a semi-log plot should show a linear dependence in which the slope is inversely proportional to the plasma temperature, defined by:

$$\ln\left(\frac{4\pi L_{21}^{peak}\lambda_{21}}{hcg_2A_{21}l}\right) = -\frac{1}{kT}E_2 \qquad (3.1)$$

where L_{21}^{peak} is the peak radiance of the emission line, λ_{21} is the wavelength, A_{21} is the transition probability and g_2, E_2 are the statistical weight and the energy of the upper level of the transition, respectively. Figure 3.5 shows examples of the plots performed from spectra recorded in vacuum at 0.5 cm from the target.

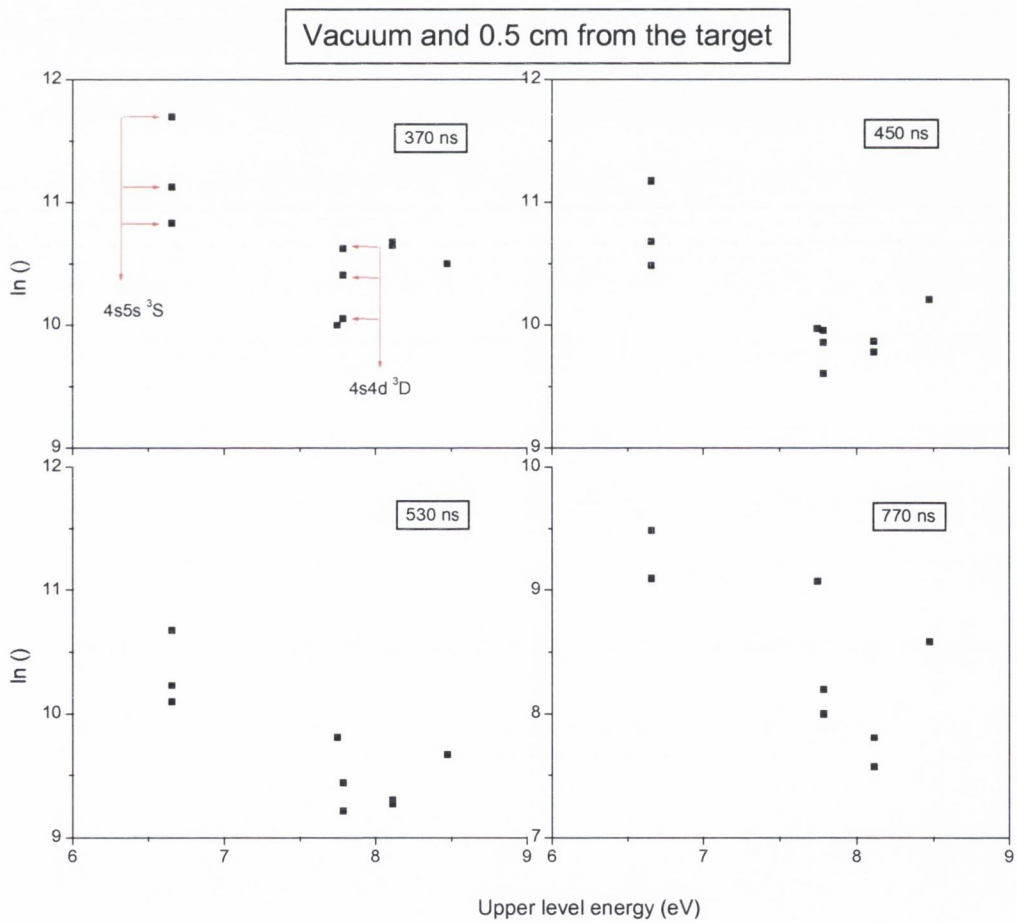

Figure 3.5. Boltzmann plots using data extracted from spectra recorded at 0.5 cm from target in vacuum for different delay times after the laser pulse.

It is clear that the dependence on the level energy is quite erratic and, although it tends to linearise at later times, i.e. at 770 ns, there is no clear evidence of a linear dependence. While this behaviour in time is to be expected due to the transient properties of laser produced plasmas, the time required to reach equilibrium should still only be of the order of 10s of nanoseconds, particularly when we consider the average density and temperature of these plasmas [Griem, 1963]. It is also of interest to examine the relative radiance of the lines within a multiplet which are from common or closely spaced levels. If the plasma is optically thin the relative radiance within the multiplet should remain constant and be determined by the line strength (*S*). Thus, for example, taking S from Table 3.1, lines within triplet *4s4d* ^3D would have ratios of 1.8, 5 and 2.8 but clearly they do not (Figures 3.6 and 3.7). Similar problem can be observed for the triplet *4s5s* ^3S.

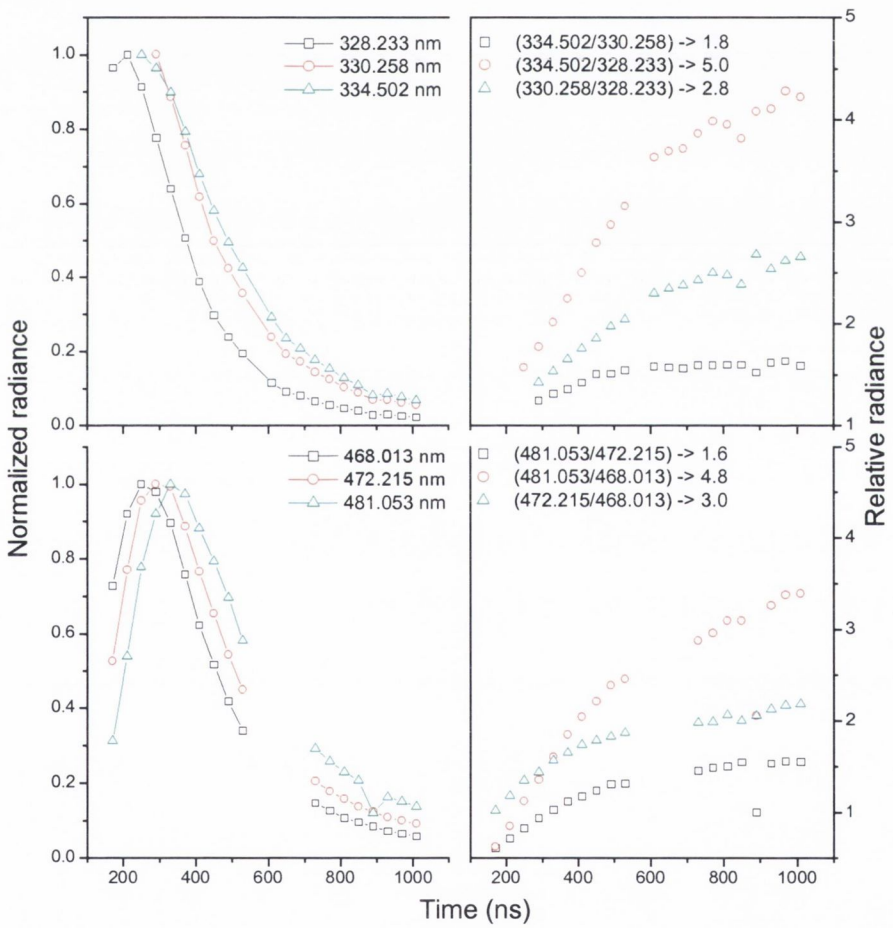

Figure 3.6. Left hand side shows the time behaviour of the intensity of the lines in the triplet 4s5s ^{3}S and *4s4d* ^3D. Right hand side shows evolution of the relative intensities of the lines in the triplet and in the legend the theoretical relative intensity is presented.

From Figure 3.6 it can be observed as well that the transitions reach their maximum at different times which seems unreasonable since they belong to the same triplet. This behaviour suggests that a self absorption process is present, and therefore, the plasma is optically thick for some transitions.

In order to correct for such a process it is necessary to know if and to what extent each line is self absorbed. The self absorption coefficient $\kappa_{abs}(\lambda, T)$ is defined by:

$$\kappa_{abs}(\lambda, T) = \pi r_0 \lambda^2 f_{12} n_1 \left[1 - e^{-\frac{hc}{\lambda kT}} \right] P(\lambda, \lambda_0) \qquad (3.2)$$

where $r_0 = 2.82 \times 10^{-15} m$ is the classical electron radius, n_1 is the population of the lower level in the transition and $f_{12}, \lambda, P(\lambda, \lambda_0)$ are the absorption oscillator strength, the wavelength and the profile of the transition line [Thorne, et al., 1999]. As a first approximation a comparison of the absorption among lines of the same multiplet can be performed by looking at the product $\lambda^2 f_{12} n_1$. Assuming LTE, an estimate of the relative level population can be made from their statistical weight g_1. Table 3.1 shows the result of such an approach for all transitions presented in Figure 3.4 together with some fundamental properties.

Table 3.1. Values of fundamental properties of the levels involved in the studied transitions. In the table S is the line strength in atomic units and A_{21} is the transition probability, the rest of the magnitudes as previously explained.

Wavelength (nm)	E_2 (eV)	A_{21} (s^{-1})	g_1	g_2	f_{12}	f_{21}	S (a.u.)	$\lambda^2 * f_{12} * g_1$ (10^{-13} m^2)
213.857	5.796	7.039E+08	1	3	1.4390	0.4797	10.19	0.658
301.836	8.113	3.583E+06	1	3	0.0146	0.0049	0.15	0.013
303.578	8.113	1.057E+07	3	3	0.0145	0.0145	0.44	0.040
307.206	8.113	1.702E+07	5	3	0.0144	0.0239	0.73	0.068
328.233	7.783	8.657E+07	1	3	0.4169	0.1390	4.53	0.449
330.258	7.783	1.072E+08	3	5	0.2904	0.1742	9.53	0.950
330.294	7.783	5.956E+07	3	3	0.0968	0.0968	3.18	0.317
334.502	7.784	1.500E+08	5	7	0.3501	0.2501	19.40	1.959
334.557	7.783	3.749E+07	5	5	0.0625	0.0625	3.46	0.350
334.594	7.783	4.166E+06	5	3	0.0042	0.0069	0.23	0.023
462.981	8.473	1.492E+06	3	5	0.0079	0.0048	0.37	0.051
468.013	6.655	1.553E+07	1	3	0.1521	0.0507	2.36	0.333
472.215	6.655	4.576E+07	3	3	0.1520	0.1520	7.13	1.017
481.053	6.655	7.004E+07	5	3	0.1449	0.2415	11.54	1.677
636.234	7.744	4.652E+07	3	5	0.4676	0.2806	29.57	5.679

In Table 3.1, different colours were used to group transition from the same multiplet. From the values in the last column of the table is to be expected that within their respective multiplet the lines 307. 206 nm, 334.502 nm and 481.053 nm are the most self absorbed. This is in agreement with the pattern of the relative intensities showed in Figure 3.6 and is more clearly observed in Figure 3.7, where an evolution in time of the emission from the multiplet $4s5s\ ^3S$ is shown.

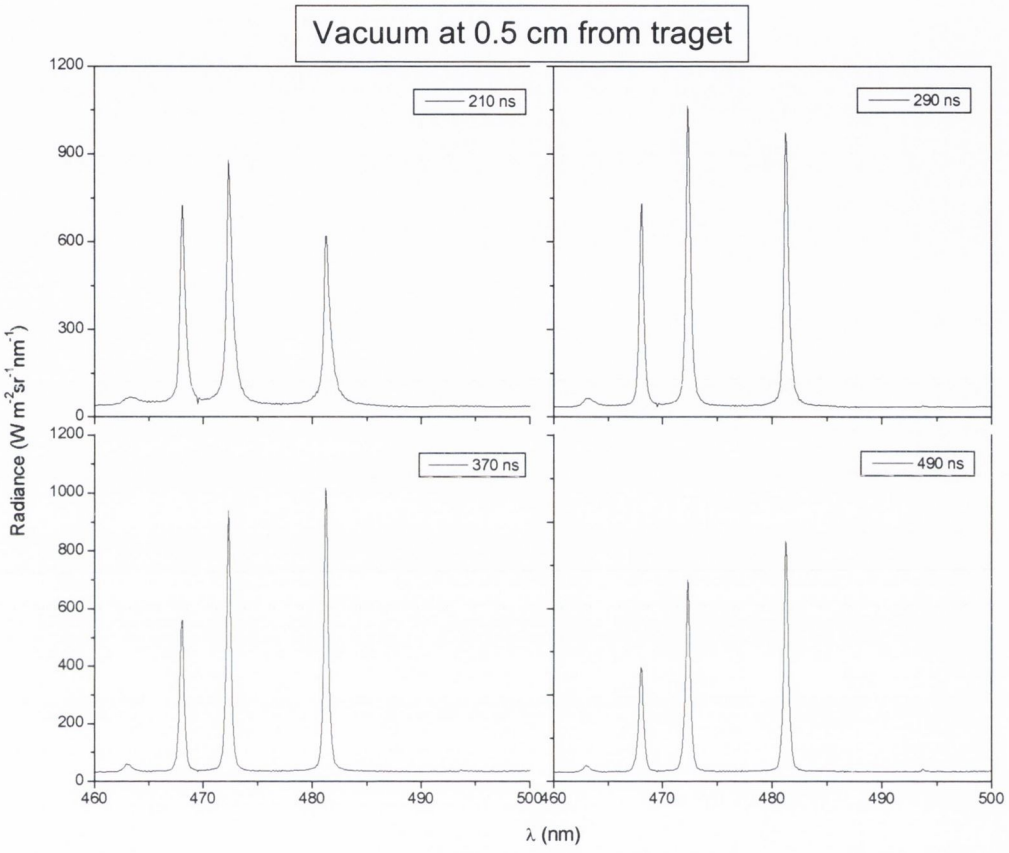

Figure 3.7. Transitions from the triplet 4s5s ^{3}S. The line 481.053 nm shows a greater self absorption.

3.1.3 Correction for self-absorption

For a complete estimate of the absorption coefficient (equation (3.2)) it is necessary to know both the line profile and population of the lower level involved in the transition.

The line profile used to do the radiation transport calculation will be Gaussian or Lorentzian if Doppler or pressure broadening can be neglected, respectively. If both are taken into account a Voigt profile is obtained. It should be noted that the recorded spectral line can be modulated by the spectrometer response function. This is the

case if the FWHM of the response function is comparable to or greater than the resultant FWHM of the line due to all the broadening mechanisms. The recorded spectra will be a convolution of the line profile with the spectrometer response function, which is closely reproduced by a Gaussian profile.

Besides natural broadening, two processes are responsible for the broadening of the emission lines, Doppler effect and pressure broadening. The former is related to the relative speed of an emitter moving toward or away from the observer. Doppler broadening is usually determined by the thermal velocity of the emitting species and is characterized by a Gaussian distribution. It is defined as:

$$\Delta\lambda_D = 2\sqrt{\ln 2}\frac{\mathrm{v}}{c}\lambda_c \qquad (3.3)$$

where c is the light speed, v is the plasma emitting species velocity relative to the observer and λ_c is the central wavelength of the emission [Thorne, et al., 1999]. For heavy atomic and ionic species this velocity is small and the Doppler broadening can be neglected in comparison with pressure broadening. In laser produced plasmas, depending on whether the process takes place in vacuum or in presence of gas background, the expansion velocity could be greater than the thermal and the former determines the Doppler broadening. It should be noticed that in such case the profile is not necessarily Gaussian as the relevant one-dimensional velocity distribution function may not be Gaussian. An estimate of the maximum bulk motional Doppler broadening can be obtained using the component of the plasma front expansion velocity in x axis (Figure 2.1). In Chapter 2 the plasma front expansion velocity in the z axis was determined to be 2.3×10^4 m/s and knowing the elongation constant ($K_e = 2.4$) in the plane xz (Figure 2.4) the velocity in the y axis can be obtained as follows:

$$\mathrm{v}_x = \frac{\mathrm{v}_z}{K_e} \qquad (3.4)$$

From equations (3.3) and (3.4) Doppler broadening of the order of $\Delta\lambda_D = (0.01-0.03)\,nm$ are expected for the spectral region studied in this thesis. Perhaps a better approach for determining Doppler broadening due to the plasma flow is to use the component of the most probable velocity (1×10^4 m/s) of the particles at the FWHM (44^0) of the angular distribution in the plane xz (Figure 2.4)

instead of using the velocity defined in equation (3.4). In this case the estimated Doppler broadening would decrease to $\Delta\lambda_D = (0.007 - 0.01)\,nm$.

Pressure broadening includes three processes; resonance ($\Delta\lambda_{res}$), van der Waals ($\Delta\lambda_{vw}$) and stark ($\Delta\lambda_{st}$) broadening. All of them are characterized by a Lorentzian shape and are defined by [Born, 1999]:

$$\Delta\lambda_{res} = \frac{\lambda_c^2}{c}\pi C_{res} n_{rad}$$

$$\Delta\lambda_{vw} = \frac{\lambda_c^2}{2\pi c} 8.08 \left(\frac{8kT}{\pi}\right)^{0.3} \sum_p \left(\frac{1}{\mu_{rad,p}}\right)^{0.3} C_{vw}^{0.4} n_p \qquad (3.5)$$

$$\mu_{em,p} = \frac{m_{rad} m_p}{m_{rad} + m_p}$$

$$\Delta\lambda_{st} = \frac{\lambda_c^2}{2\pi c} 11.37 \left(\frac{8kT}{\pi m_e}\right)^{\frac{1}{6}} C_{st}^{2/3} n_e$$

Here, the summation is performed over the total number of neutral perturbers denoted by index (p), m_{rad}, m_p are the mass of the radiating and the perturber species and n_{rad}, n_e are the density of radiating species and electrons. The constants C_{res}, C_{vw}, C_{st} are the coefficients for resonance, van der Waals and Stark broadening respectively.

Figure 3.8 shows the values associated with the different broadening mechanisms as function of atomic and ion density. The values used for the coefficients in equation (3.5) were extracted from the work reported by Born [Born, 1999, Dimitrijevic, et al., 1983]. A temperature value of 116000 K was used to account for the possible maximum broadening.

In the van der Waals broadening calculation the interaction with the oxygen atoms in the plasma was not taken into account. This is due to the fact that both α_O=0.82×10^{-24} cm^3 and α_{O2}=1.58×10^{-24} cm^3, for atomic and molecular oxygen polarizabilities respectively [Lide, 1998], are negligible compared to the zinc polarizabilty α_{Zn}=7×10^{-24} cm^3.

From Figure 3.8 it can be observed that broadening due to neutral perturbers is dominated by the resonance interaction. The Doppler effect can be neglected compared to resonance or Stark effect only if the atom density is greater than 10^{24} m^{-3} or the electron density is greater than 10^{23} m^{-3} respectively.

In Chapter 2 the dimensions of the expanding ellipsoidal plasma plume were obtained (Figure 2.2 d) from the Anisimov model. Using this and the total number of zinc atoms (~1.2×10^{16}), extracted from the mass loss measurement, the temporal evolution of the number density of zinc can be obtained (Figure 3.9).

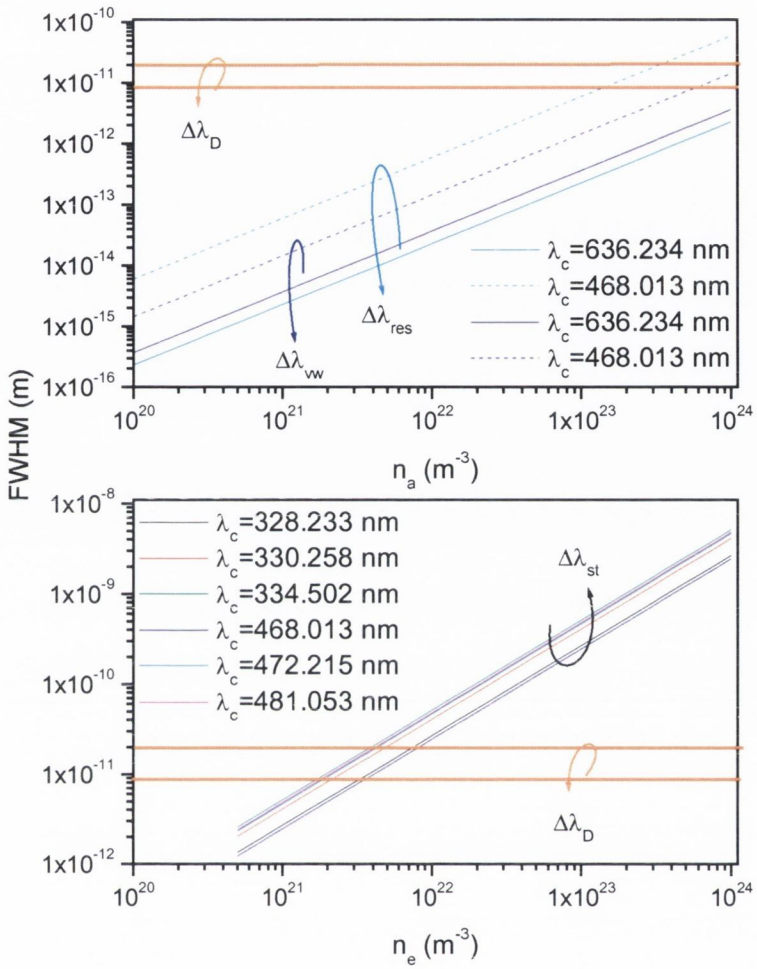

Figure 3.8. Calculated line broadening as a function of atom (top) and ion density. In both sets of data van der Waals and Stark broadening was accounted for using a temperature of 116000 K .

In the calculation of the number densities plotted in Figure 3.9 only half of the measured mass loss was used. This is due to the fact that the broadening due to zinc-oxygen interaction was neglected. Strictly, Figure 3.9 represents the total number density of zinc species including both atoms and ions. Correction for the ion component can be done by using the ion densities extracted with the Langmuir probe technique. In the next section it will be seen that the ion density is of the order of 10^{18}-10^{20} m^{-3} (10^{12}-10^{14} cm^{-3}), which does not affect seriously the values of neutral atom density plotted in Figure 3.9.

Comparison of Figure 3.8, 3.9 and the extracted electron number density suggests that Doppler broadening cannot be neglected. However, the problem is which distribution should be used if the Doppler broadening is to be taken into account. Although a solution for such a problem is not presented in this thesis, the possible effects of considering or not this broadening will be discussed later. It should be noticed that in most of the reports [Born, 1999;Harilal, et al., 1997;Hermann, et al., 1998] on this topic for laser produced plasmas, it is assumed that the line profiles are defined by pressure broadening mechanisms.

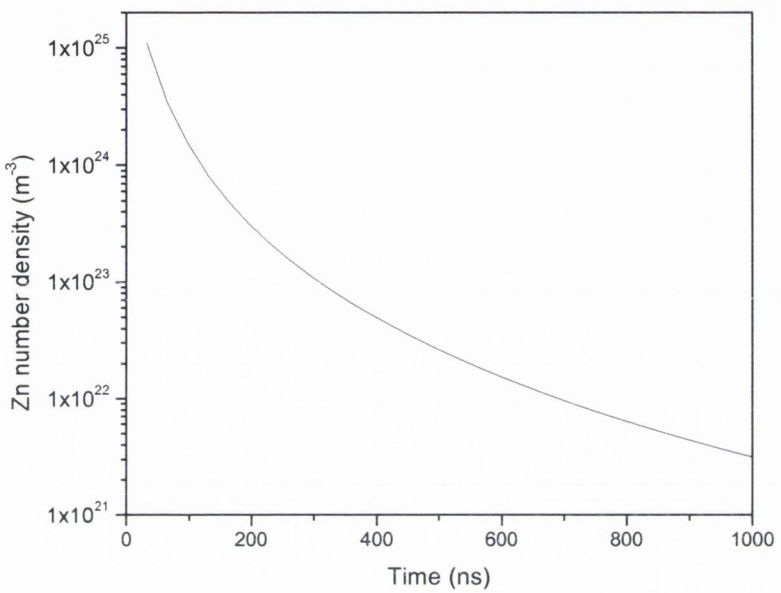

Figure 3.9. Number density of zinc species as calculated using Anisimov model and the measured mass loss.

Using the equations (3.5) the Lorentzian line profile [Born, 1999] can be defined by:

$$P(\lambda,\lambda_0)=\frac{\Delta\lambda}{2\pi}\frac{1}{(\lambda-\lambda_c-\delta\lambda)^2+\left(\frac{\Delta\lambda}{2}\right)^2}$$

$$\Delta\lambda=\Delta\lambda_{res}+\Delta\lambda_{vw}+\Delta\lambda_{st} \qquad (3.6)$$

$$\delta\lambda=0.36\Delta\lambda_{vw}+0.86\Delta\lambda_{st}$$

where λ_c is the transition wavelength, $\Delta\lambda$ is the total width of the line and $\delta\lambda$ is the line shift.

As mentioned at the beginning of this subsection, besides the line profile, the number density of atoms with exited state n_1, the lower level in a transition, is needed to account for self absorption of the emitted line (see equation (3.2)).

From the calculated criteria (Chapter 1) and the ion density, extracted using the Langmuir probe technique (Figure 3.23), it was concluded that the condition for a PLTE was established even down to the metastable level.

If a PLTE exists, the number density of atoms in state j (n_{aj}) is related to the electron (n_e) and ion (n_i) number densities by [Thorne, et al., 1999]:

$$\frac{n_e n_i}{n_{aj}} = 2\frac{(2\pi mkT)^{\frac{3}{2}}}{h^{\frac{3}{2}}}\frac{g_i}{g_{aj}}\frac{Z_i(T)}{Z_a(T)}e^{-\frac{E_i-E_j}{kT}} \tag{3.7}$$

where g_i, g_{aj} are the statistical weights and $Z_i(T)$, $Z_a(T)$ the ion and atom partition functions. Since the oxygen ionization energy is greater than that of zinc, it was assumed that all ionic species are single ionised Zn atoms. Equation (3.7) can be expressed as:

$$n_{aj} = \frac{n_e^2}{2\frac{(2\pi mkT)^{\frac{3}{2}}}{h^{\frac{3}{2}}}\frac{g_i}{g_{aj}}\frac{Z_i(T)}{Z_a(T)}e^{-\frac{E_i-E_j}{kT}}} \tag{3.8}$$

Combining equations (3.2), (3.5) and (3.8), the absorption coefficient is completely defined by the principal properties of the plasma such as both electron and atom number density and plasma electron temperature. Therefore it is possible to have a complete estimation of self absorption effects over the different transitions providing we know the plasma properties. On the other hand these are, indeed, the parameters which need to be determined. In order to determine these parameters synthetic spectra for different values of the plasma parameters were generated and fitted until the experimental recorded spectra is matched. The approach used to model the spectra is outlined in the following section.

3.1.4 Spectra calculation

The radiance $L(\lambda,T)$ emitted by a transition from the upper level n_2 to a lower n_1 is defined by [Thorne, et al., 1999]:

$$L(\lambda,T) = \frac{2hc^2}{\lambda^5}\frac{g_1 n_2}{g_2 n_1} \tag{3.9}$$

and accounting for self-absorption:

$$L(\lambda,T) = \frac{2hc^2}{\lambda^5}\frac{g_1 n_2}{g_2 n_1}\left(1-e^{-\kappa(\lambda,T)l}\right) \tag{3.10}$$

where $\kappa(\lambda, T)$ is the absorption coefficient as defined in equation (3.2) and l is the length of line of sight in the measurement. Equations ((3.2)-(3.10)) are fully determined by the plasma properties.

As highlighted earlier the recorded spectra are a result of a convolution of the line profile, as defined by equation (3.6), and the spectrometer response function. The spectrometer response function was assumed to be Gaussian with a FWHM determined by the greatest of the used slits (W_{slit}), the instrument magnification in the horizontal axis (1.1) and the instrument linear dispersion (LD), that is:

$$FWHM_{spect} = 1.1 \times W_{slit} \times LD \qquad (3.11)$$

From equation (3.11) with $W_{slit} = 50\mu m$ and a $LD = 3.2\,{}^{nm}/_{mm}$ the $FWHM_{spect} = 0.176nm$.

For the calculations a small code was developed using the LabTalk programming tool within Origin software. The general algorithm is as follows:

- First a set of values for the plasma parameter is introduced and using the above defined set of equations the radiance of a defined spectral region is calculated. The reason for calculating separately the different spectral regions is due to the fact that each of them was recorded with different wavelength calibration, so the wavelength step was different.
- The second step was to convolve the calculated spectrum with a normalized Gaussian distribution with $FWHM_{spect} = 0.176nm$.
- Finally the convolved spectrum is compared to that obtained experimentally.

The following constraints are used during the calculation:

- The value for the line of sight (l) is obtained using the Anisimov model (Vacuum) or from the ICCD photographs (oxygen). For both cases knowing the position of the plasma front at the time the spectrum was recorded, the dimension of the line crossing the plasma at the measuring position can be calculated.
- Although the atom number density has little effect in the calculation, which follows from the negligible effect of both resonance and van der Waals broadening in the lines profile, its value is obtained too from Figure 3.9.

- The electron number density, which is assumed to be equal to the ion number density, is up bounded by the ion number density extracted using Langmuir probe.

Figure 3.10 shows the result of the above calculation for the lines emitted from the *4s4d* ^3D and *4s5s* ^3S triplets. In both cases the spectrum was recorded in vacuum at 0.5 cm from the target and 290 ns delay time.

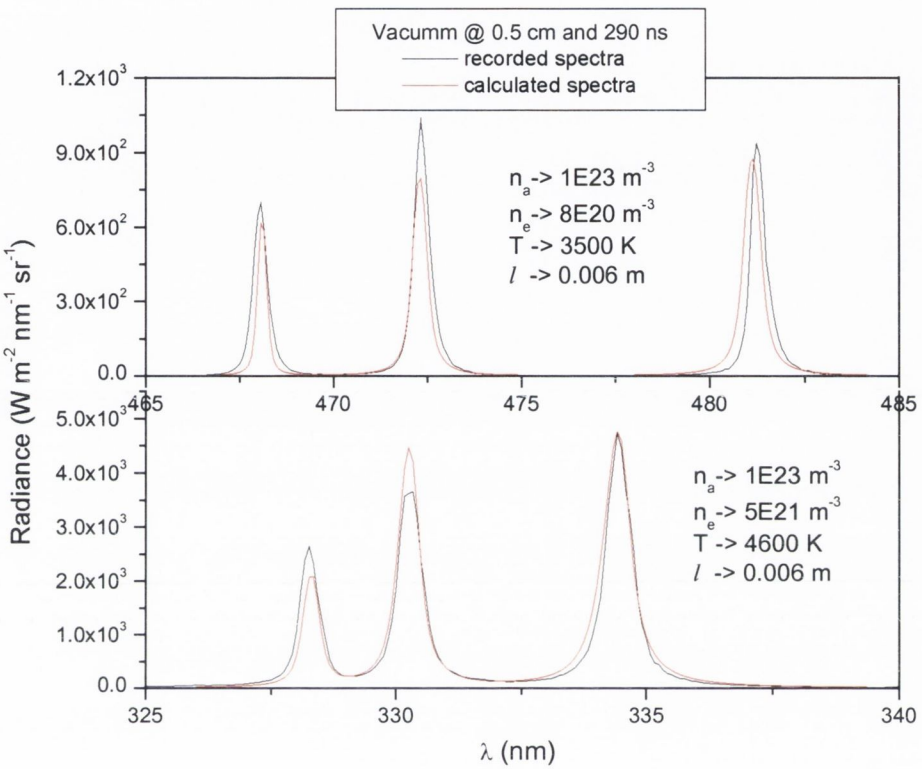

Figure 3.10. Comparison of recorded and calculated spectra of transitions from both *4s4d* ^3D (bottom) and *4s5s* ^3S (top) triplets. Plasma parameters as extracted from the calculation are shown for each case.

Comparison of the plasma parameters presented in Figure 3.10 reveals great difference for both temperature and electron density. The reason for such a result could be a failure of the assumption of PLTE down to the metastable level. In order to corroborate the latter, the following calculation was performed. Instead of fixing the population of the metastable level through equation (3.8), a best value adjustment routine was allowed during the process. As the lower levels are common to both set of transitions their population should be the same independently of which upper level is analysed. From this, firstly, the best lower level populations ($n_{a,low}$) were extracted using the set of transitions from triplet *4s4d* ^3D. Then these values were used as input

data for the calculation of the set of transitions from triplet *4s4d* ^3S, keeping constant the remaining parameters. The reason for selecting the transitions from triplet *4s4d* ^3D to calculate the lower level populations will be observed later. Figure 3.11 shows the result of such a calculation.

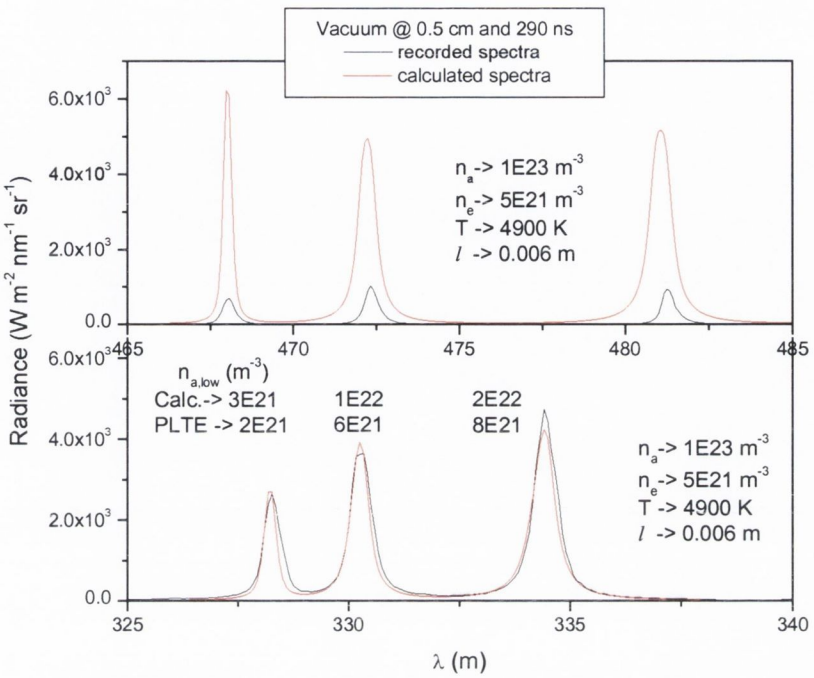

Figure 3.11. Bottom part shows a comparison of the recorded and calculated spectrum of the transitions from triplet *4s4d* ^3D. In the calculation of lower level populations a best value adjustment routine was allowed during the process. The results were used to calculate the spectrum of the transitions from the triplet *4s5s* ^3S, shown in the top part. Note that both the calculated lower populations and their values if a PLTE is established are given in the bottom figure.

The result shows a great difference between the recorded and calculated spectrum for the transitions from the triplet *4s5s* ^3S. In other words, this means that if calculation is performed separately for each set of transitions the best values for the lower level populations would be different, which is in contradiction with the explanation presented in the preceding paragraph. Once more, arises the question of whether the assumption of PLTE is valid for the triplet *4s5s* ^3S arises Although the validity criteria (Chapter 1) suggest that this is the case for levels with $n \geq 3$, it should be noticed that such criteria applies, for non-hydrogenic species, and it could lead to up to 20 % of error in its estimation [Griem, 1963].

In judging which of the analysed triplets are in PLTE equilibrium, it is reasonable to select the triplet *4s4d* ^3D. This comes from the fact that it lies closer to the ionic ground state. If this assumption applies, it should be possible to calculate the

spectrum of the transitions from triplet *4s5s* ^3S using parameters obtained from the triplet *4s5d* ^3D. As was done for the metastable levels, the population of the triplet *4s5s* ^3S is allowed to adjust to best values. The uniqueness of the solution is guaranteed by two main reasons. Firstly, line profiles are fully dependent on the electron density and plasma temperature. Second, as both statistical weight and energy of the triplet *4s5s* ^3S is equal for all transitions, the relative line intensities will be determined by the absorption oscillator strength of the lines and the population of the metastable levels. So only one set of plasma parameters and levels population can be found which reproduces all the features of the recorded spectra for both triplets. Figure 3.12 shows the result of such a calculation.

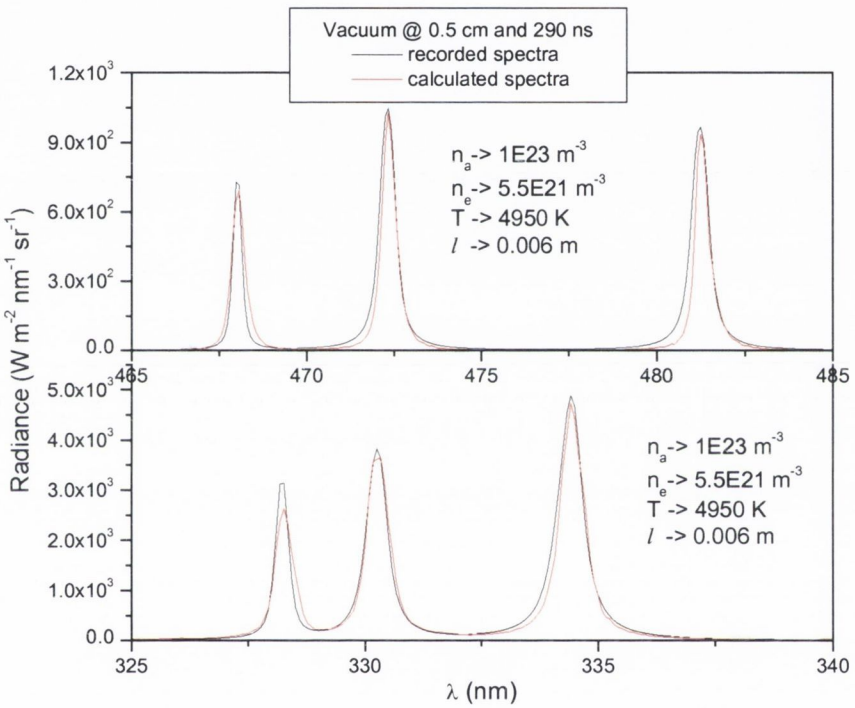

Figure 3.12. The figure shows a comparison of the recorded and calculated spectra of the transitions from triplet *4s4d* ^3D and triplet *4s5s* ^3S. In the calculation both lower levels populations and upper level population of triplet *4s5s* ^3S were let to adjust to the best values.

The result of the calculation is in reasonable agreement with the recorded spectra. For all cases the relative lines intensities are well reproduced. The major discrepancies are in the line profiles with greater deviation for the transitions from the triplet *4s5s* ^3S. Such a discrepancy can be explained if the accuracy of the broadening coefficients (~ 20%) is taken into account [Dimitrijevic, et al., 1983]. The lower levels population were the same as presented in Figure 3.11. The

calculated population for the triplet *4s5s* ^3S was 3×10^{18} m^{-3} lower than 1×10^{19} m^{-3}, the value predicted if PLTE is established.

To this point all the results support the idea that LPTE can only be assumed for levels with energies equal or greater than the triplet *4s5d* ^3D. On the other hand plasma parameters obtained from the fit of the spectrum from this triplet have proved to be correct. From this, from now on, all the plasma parameter extraction will be performed using this triplet.

From Figure 3.12, it can be observed that, although reasonable, the extracted electron density is greater than the one measured using Lamgmuir probe. The maximum electron density predicted from this technique is in the order of 1×10^{21} m^{-3}.

As previously mentioned it is important to have an idea of the effects of the Doppler broadening on the overall spectra. Figure 3.13 presents the results of the calculation of the spectrum of the transitions from the triplet *4s5d* ^3D but taking into account this broadening. The procedure was to include the maximum broadenings, calculated earlier in this section, within the total profile broadening defined by equation (3.6).

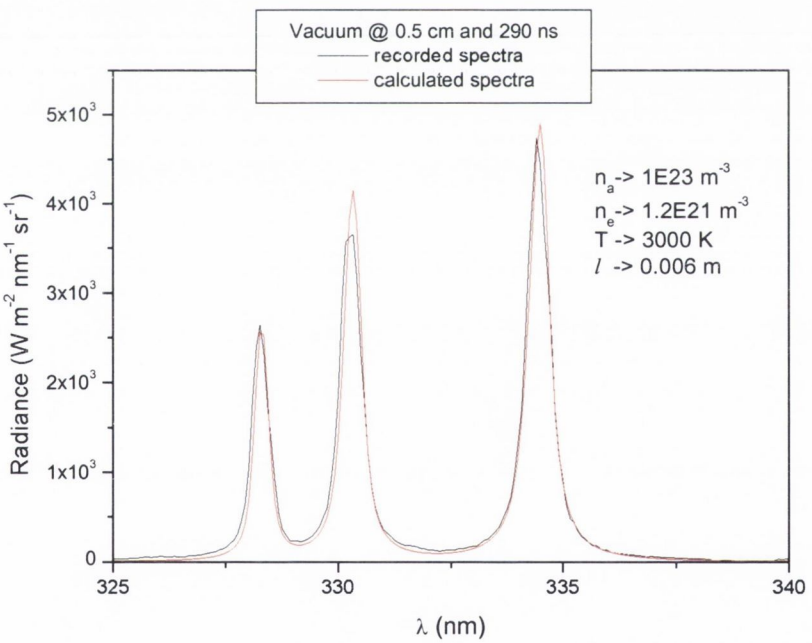

Figure 3.13. The figure shows a comparison of the recorded and calculated spectra of the transitions from triplet *4s4d* ^3D but taking into account the broadening due to Doppler effect.

Comparison of the results presented in Figure 3.12 and Figure 3.13 shows that, not only the reproduction of the over all spectrum features is better but that the

extracted plasma electron density is in much better agreement to the values obtained using Langmuir probe.

For a laser produced plasma expanding in vacuum effects of the Doppler broadening are expected to be more relevant at later times, i.e., when the plasma plume had increased its volume and the number density reduces but the expansion velocity keeps constant. The former causes the pressure broadening mechanisms to become less predominant compared to Doppler. An example of such process can be observed in Figure 3.14.

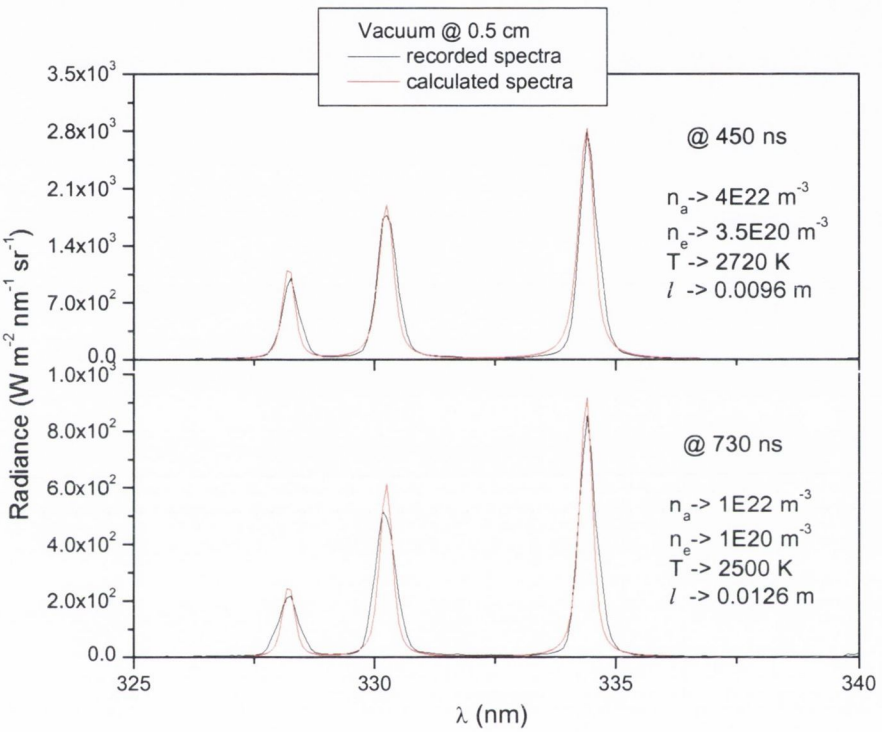

Figure 3.14. Recorded and calculated spectra at two different delay time 450 ns (top) and 730 ns (bottom). For both cases the plasma expanded in vacuum.

Although the calculated and recorded spectra are still in reasonable agreement, differences can be observed in the line profiles. Now the component of the Lorentzian profile is less significant and the final recorded line profile tends to a Gaussian shape. Note that the extracted plasma parameters show a consistent reduction for both electron density and temperature.

The same calculation procedure was performed to identify the effects of the oxygen background over the plasma properties. Figure 3.15 shows the result obtained. Comparison of these results with the ones obtained for the vacuum case

(Figure 3.13) reveals that there is a reduction of the electron density while the temperature was not noticeably affected.

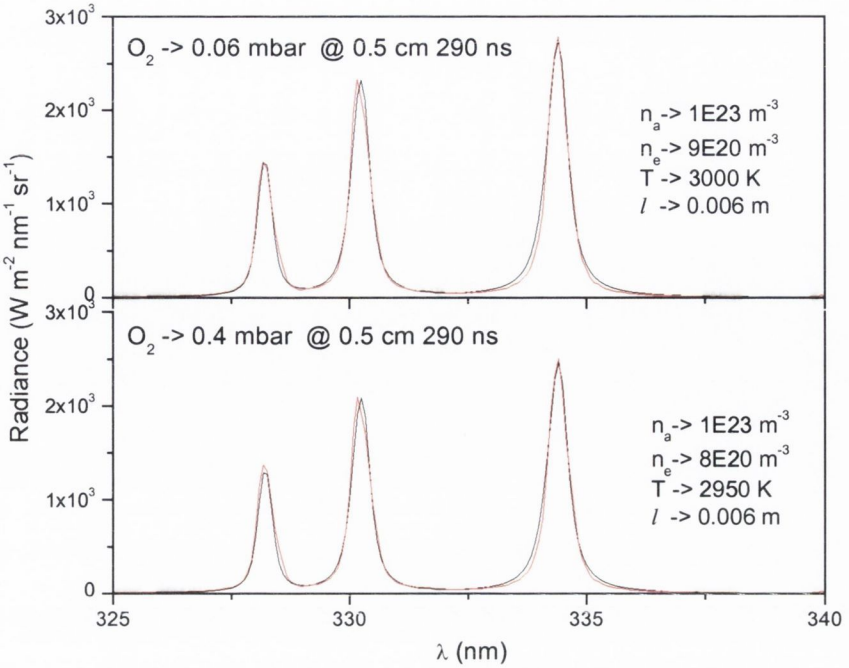

Figure 3.15. Comparison of the recorded and calculated spectra of the transitions from triplet $4s4d\ ^3D$. Top, after the introduction of 0.06 mbar of oxygen and bottom for 0.4 mbar.

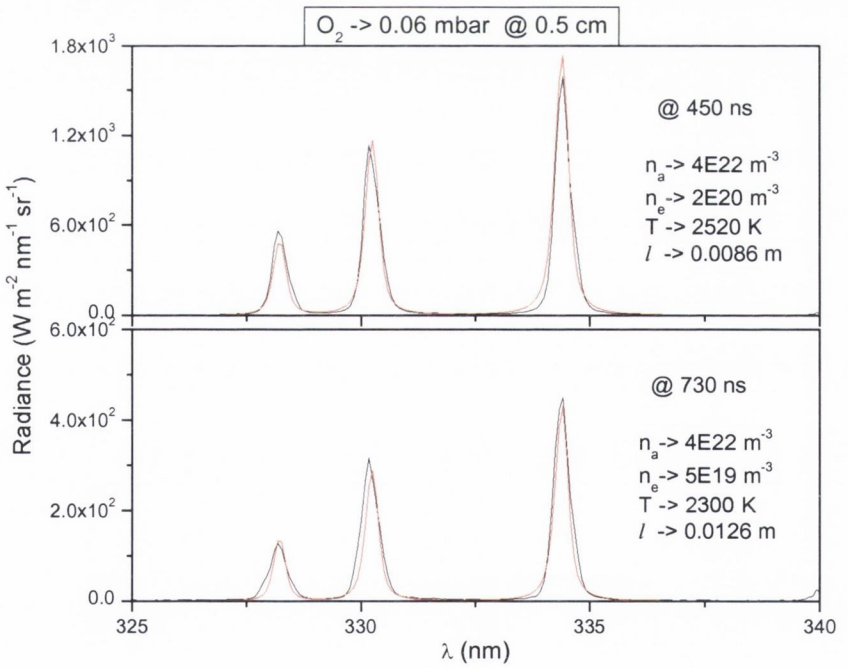

Figure 3.16. Recorded and calculated spectra at two different delay time 450 ns (top) and 730 ns (bottom). For both cases the plasma expanded in 0.06 mbar of oxygen.

Figure 3.16 shows the recorded and calculated spectra for two different times, 450 ns and 730 ns, both at 0.5 cm from the target and in 0.06 mbar of oxygen.

Similar to the results obtained for the vacuum case (Figure 3.14) there is a decrease in both electron density and temperature. Though in this case there is a stronger reduction if both cases are compared with their respective measurements at 290 ns (Figure 3.13 for vacuum and Figure 3.15 for oxygen).

3.2 Langmuir probe

In Chapter 1 the basis of the theory and general procedures on how to use the measured I-V characteristic to extract the plasma parameters were given. It was mentioned that errors in the application of this technique can arise due to non fulfilment of the theoretical conditions. The design of the circuit can, as well, lead to misinterpretation of the extracted plasma parameters. Another important issue is that the probe should not perturb the plasma. That is, the amount of charge drained by it should be comparatively small compared to the total amount of charge in the plasma.

3.2.1 Probe as a perturbation

To have an estimate of whether the probe was perturbing the plasma a method developed by Waymouth [Waymouth, 1966] was used. Waymouth stated that, if the drain of electron current is sufficiently large in relation to the processes replenishing the high energy "tail" of the electron-energy distribution, the shape of the distribution will be perturbed by the act of measurement. He then developed the idea of comparing the time constant with which a given probe will deplete (depletion time) a given plasma of electrons of a given velocity, with the time constant required to replenish (replenishment time) a Maxwellian "tail" with electrons of a given velocity. This replenishment time comes from the "self-collision time", defined by Spitzer [Spitzer, 1962] as the time constant with which an originally non Maxwellian distribution approaches a Maxwellian by Coulomb collisions only. For the sake of clarity the complete model is presented.

For an isotropic distribution of electron velocities, the particle current of electrons of velocity v which flows to the probe is given by:

$$\Upsilon(\mathrm{v}) = n(\mathrm{v})\frac{1}{4}\mathrm{vA}\left[1-\left(\frac{\mathrm{v}_0}{\mathrm{v}}\right)^2\right] \qquad (3.12)$$

where v_0 is the critical velocity that electrons have to overcome to reach the probe, which is defined by the bias voltage and A is the area of the probe.

If $N_e(v)$ is the total number of electrons in the plasma then,

$$n(v) = \frac{N_e(v)}{V} \tag{3.13}$$

where V is the volume of the plasma.

The time rate of change of $N_e(v)$ resulting from the loss of electrons of velocity v to the probe is:

$$\frac{dN_e(v)}{dt} = -\Upsilon(v)$$

$$\frac{dN_e(v)}{dt} = \frac{N_e(v)}{V}\frac{v}{4}A\left[1-\left(\frac{v_0}{v}\right)^2\right] \tag{3.14}$$

$$N_e(v) = N_0(v)\exp\left(-\frac{t}{\tau_d}\right)$$

where

$$\tau_d = \frac{4V}{Av}\left[\frac{1}{1-\left(v_0/v\right)^2}\right] \tag{3.15}$$

The above depletion time becomes infinitely long for electrons of velocity v_0, but for electrons with $v>>v_0$ it approaches a limiting value:

$$\tau_d = \frac{4V}{Av} \tag{3.16}$$

At this point Waymouth discusses the issue of which is the proper value of time constant to use in the criterion and selects a time constant (τ_d), such that half of the electron current drawn by a probe at the potential $-mv_0^2/2e$ is characterised by a depletion time constant shorter than τ_d.

The electron current drawn by a probe biased at $-mv_0^2/2e$ from a Maxwellian plasma is proportional to $\exp\left(-mv_0^2/2kT_e\right)$. Half of the total electron current drawn by the probe at this potential is due to electrons with velocity greater than v where:

$$\frac{\exp\left(-mv^2/2kT_e\right)}{\exp\left(-mv_0^2/2kT_e\right)} = \frac{1}{2}$$

$$v_0^2 - v^2 = \frac{2kT_e}{m}\ln(0.5) \tag{3.16}$$

$$\left(1 - \frac{v_0^2}{v^2}\right) = -1.38\left(\frac{kT_e}{mv^2}\right)$$

Therefore half the current drawn by the probe is characterised by a depletion time constant shorter than:

$$\tau_d = \left(\frac{2.9V}{Av}\right)\frac{mv^2}{kT_e} \tag{3.17}$$

Then comparing equation (3.17) with the previous mentioned replenishment time constant:

$$t_r = \frac{m^2v^3}{80\pi n_e e^4} \tag{3.18}$$

with the condition that $\tau_d >> t_r$ and using equation (3.13), the condition for the absence of a depletion effect becomes a determination of the total number of electrons in the plasma which must be exceeded:

$$N_e >> 1.5x10^4 T_e^2 A \tag{3.19}$$

where T_e is the electron temperature in degrees Kelvin and A is the area of the probe in cm^2. In the last step it was assumed that the maximum electron velocity obtained in any experiment will be given by $\frac{mv^2}{2} = 10\left(\frac{3kT_e}{2}\right)$. In other words equation (3.19) gives the maximum number of electrons that can be drained by a probe of a given area from a plasma at a given temperature.

Three different probe areas were used for the plasma study through out this thesis. Figure 3.17 shows the results of applying equation (3.19) using all probe areas and for two plasma temperatures 0.1 eV and 1 eV. Instead of plotting the total number of electrons, the number density as a function of time is plotted. The volume of the plasma at each time was calculated using the Anisimov model.

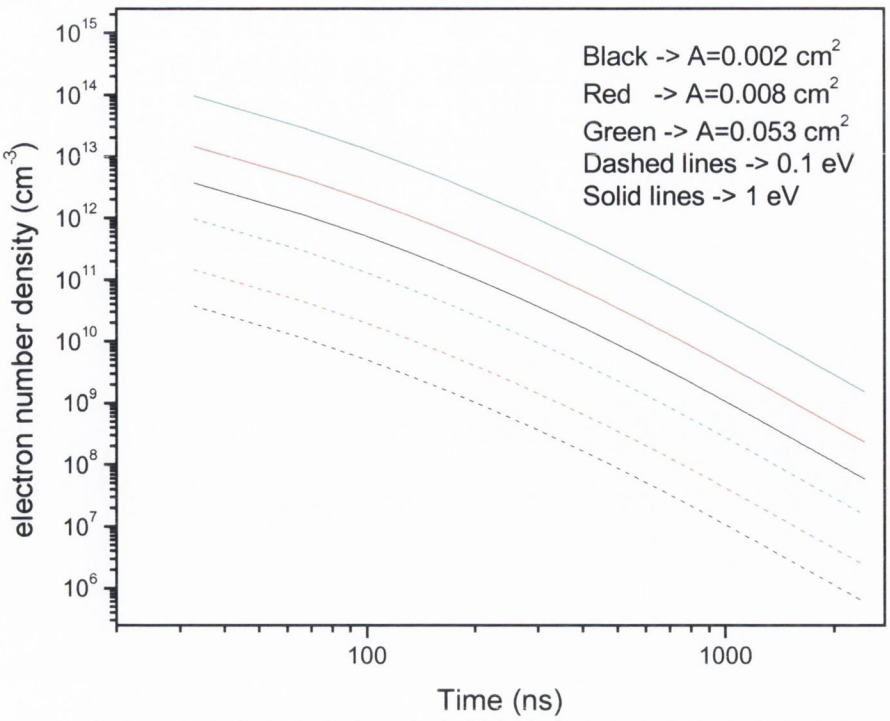

Figure 3.17. Minimum electron number density that should exist in a plasma at the specified temperatures to avoid perturbations, if a probe with the stated areas is immersed in it.

3.2.2 Koopman circuit

In Chapter 1 it was mentioned that making a small modification to the classical circuit for Langmuir probes, Koopman [Koopman, 1971] proposed a circuit for the study of flowing plasmas through the Langmuir method. In general the only change was the introduction of a capacitor in the circuit. Although a scheme of the circuit was shown in Figure 1.6 it is worth presenting it in this section as well (Figure 3.18). It is a simple *RC* circuit in which a current is set while the capacitor is charging with a time constant defined by R_1C_1. Once the charging process is finished only transient currents coming from the plasma are allowed. As the plasma plume flows by the probe position electrons and/or ions are drained and a current circulates through the circuit. If the plasma is not perturbed, the magnitude of the current will be defined by the ion and electron distribution functions, the bias voltage and the area of the probe. At this point the following question arises; will the current drained by the probe be affected in any way by the components of the circuit?

To the extent of the reviewed literature for the development of this thesis, little has been said on the role of the circuit and its components during a signal

acquisition. Koopman mentioned the idea of selecting a low resistance value of R_2 to ensure good time response. In order to answer the above question the following experiment was performed. The voltage at different nodes of the circuit was monitored as the ionic or electron signals were recorded, the measurements were carried out for two planar probes with different areas and also different combinations of R_2C_1.

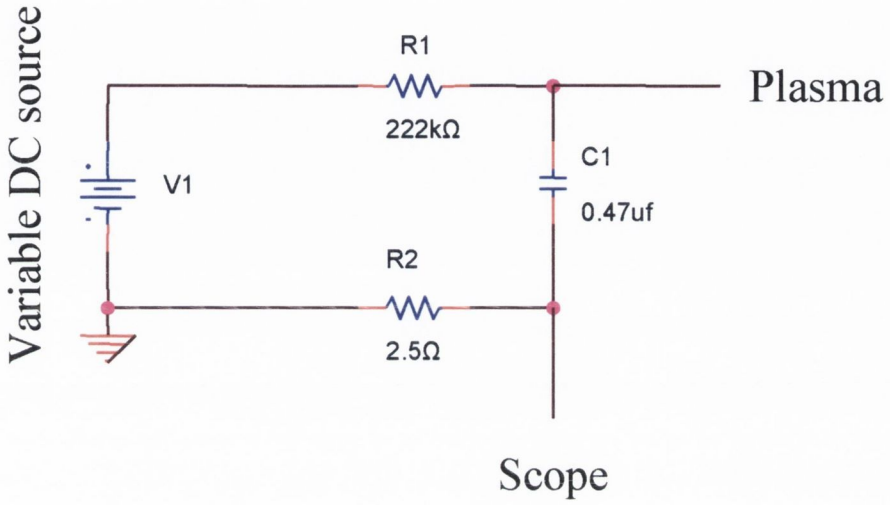

Figure 3.18. Scheme of the Koopman circuit.

The table 3.2 presents the different capacitances and resistances combinations that were used in the experiment. As can be seen all the signals were acquired at three different bias voltages. The bias voltages - 30 V and + 30 V were chosen to analyse the circuit response to a pure ion or electron current, respectively. Acquisition at 0 V allows comparison of the behaviour around the 'floating potential'.

Table 3.2. Values of the capacitances, resistances and bias voltages used for circuit analysis.

Probe area (cm^2)	Capacitance (μf)	Resistance (Ω)	Bias Voltage (V)
0.002	0.47	0.005	- 30
and	1.3	0.5	0
0.053	5	1	+ 30
	10		

For all measurements the two probes were placed at 2.6 cm from the target and in the axis of expansion. The measurements were carried out in vacuum.

Figure 3.19 shows the current densities obtained using the two probes for all possible combinations of circuit components. The inset of the figures shows the effective voltage at the probe for the case where the 10 μf and the 0.47 μf capacitances were used.

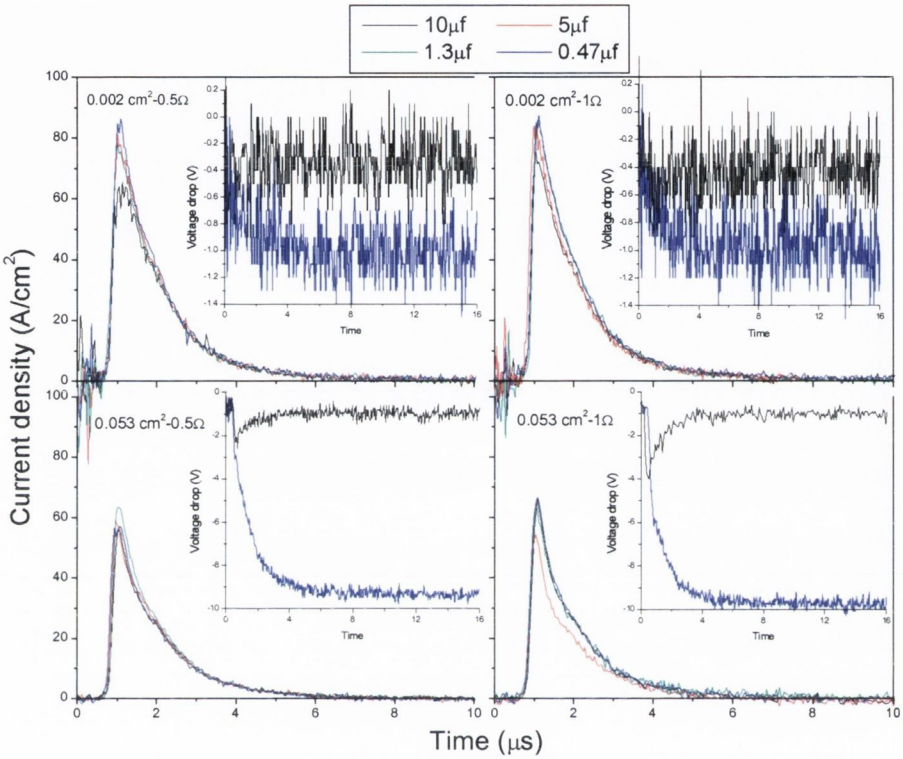

Figure 3.19. Ion density currents measured with the two probes with different combinations of circuit components. For all cases the probes were placed at 2.6 cm from the target and the experiment was carried out in vacuum. The inset of the figures shows the effective voltage at the probe.

From the figure it can be observed that for the same probe the value of the R_2C_1 selected has no effect on the ion current. Comparison between the two probes shows that the temporal evolution of the signals remains the same. The only difference is with respect to the magnitude of the current density. This difference of about 20 % can be understood if the error in area measurement and edge effects are considered.

Figure 3.20 shows the results for the measurements performed with the probe positively biased. The electron signals were characterized by the appearance of two peaks. The first peak was constant both in time and current value. This behaved the same for all R_2C_1 and probe combinations. The second peak moved to longer times

and higher current values for larger values of capacitance. This behavior was more pronounced for the probe with larger area, where the higher values of current were obtained. The second peak could be related to the ionization and the consequent current establishment through the plasma due to the high electric field.

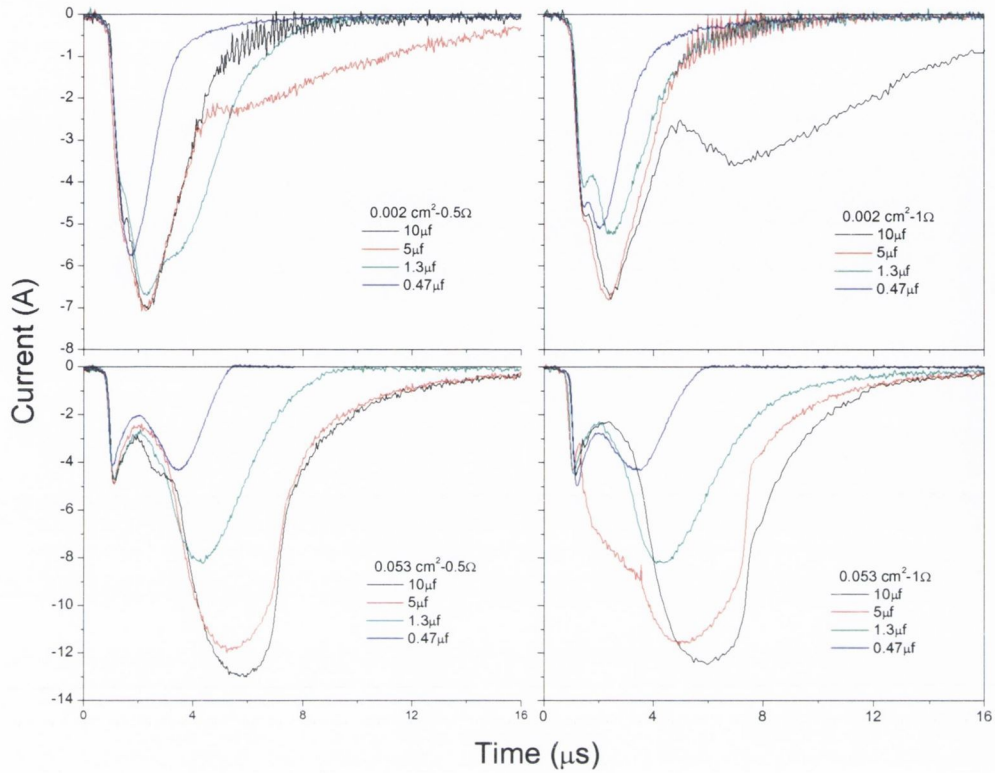

Figure 3.20. Electron currents measured with the two probes with different combinations of circuit components. For all cases the probes were placed at 2.6 cm from the target and the experiment was carried out in vacuum.

Figure 3.21 shows example of the probe current obtained during the electron current measurements at the electron retardation region (top) and the derivative signal obtained (bottom) as explained in the following paragraph.

The above mentioned features helped to draw the conclusion that the particle current was only determined by the geometry of the probe and the plasma properties. In other words if there is no perturbation of the plasma properties, the current that flows through the circuit is proportional to the area of the probe and the number density of charged species in the plasma. There was no modification of the drained current made by the circuit. This suggests that the Koopman circuit behaves as a simple passive high pass filter, with a cut off frequency defined by R_2C_1. Another corroboration was the fact that when R_2=0.005 Ω was used in the circuit a derivative

signal was observed, which is a typical response of a high pass filter to a low frequency signal.

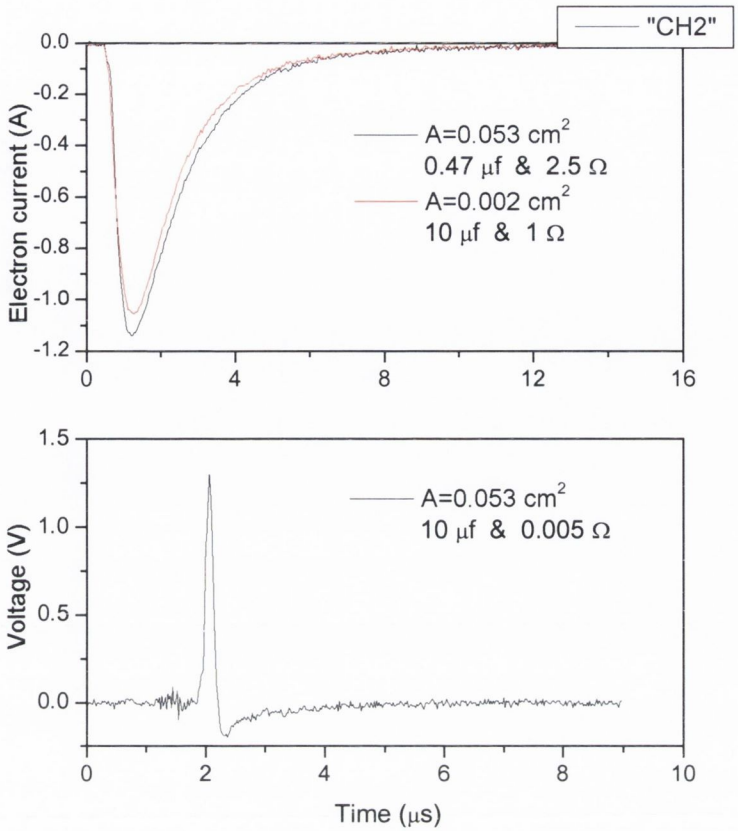

Figure 3.21. Example of the probe current obtained during the electron current measurements at the electron retardation region (top) and the derivative signal obtained (bottom).

It is important to mention that while the cut off frequency is negligible for probe measurements in vacuum, where typical signal rise time is around 2-4 μs, it does becomes an important issue when the experiments are performed in a gas background. Calculation for the circuit showed in Figure 3.18 gives a cut off frequency of 132 kHz which is about 7 μs. From the ion and electron signals, in Figures 3.19 & 3.20 respectively, it can be observed that there should be no reduction in the measured current values.

Until now the analysis was centred on whether the current the probe drained from the plasma was affected or not by the circuit used in the measurement. No attention was given to the bias voltage at which the probe was held during the measurement. This is an important issue since it is from the constructed I-V plot that the plasma properties are extracted. An error in the reading of the voltage at which a given current was measured implies an error in the slope of the plot and so in the calculated

electron temperature. Although a voltage (V_{bias}) is set by the source V_1 any voltage drop due to the probe current across R_2 and the depletion of charge on C_1 will affect V_{bias}. This voltage drop is the sum of the voltage across C_1 (V_c) and across R_1 (V_r) and will change in time as the current. So the real voltage (V_{real}) at which the current is collected can be defined as follow:

$$V_{real} = \mp V_{bias} \pm \left[\left(\frac{1}{C_1} \int i(t)dt \right) + \left(i(t)R_2 \right) \right] \qquad (3.20)$$

It should be note that no matter what the polarity of the V_{bias} is, the drained current will reduce the absolute value of the voltage, so $V_{real} < V_{bias}$. Examples of the above mentioned voltage drop were presented in the inset of Figure 3.19 and in Figure 3.21.

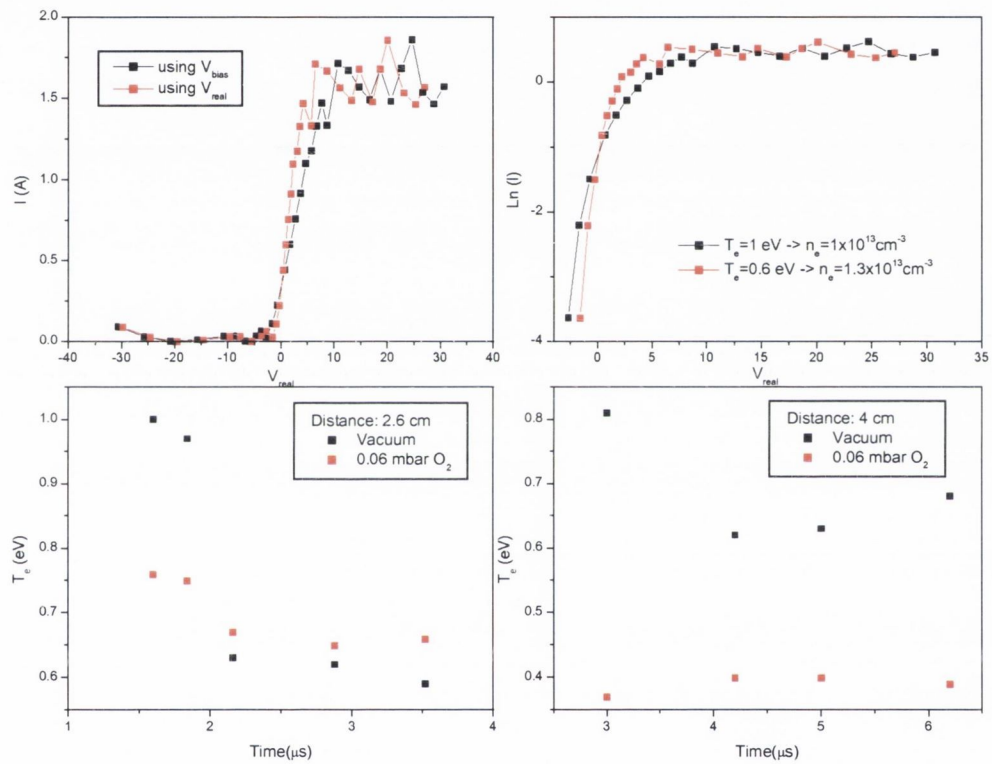

Figure 3.22. Shows the I-V plot obtained from a measurement at 2.6 cm from the target in vacuum and at 1.92 μs. The measured current was plotted versus V_{bias} (black) and V_{real} (red). The bottom graphs present the temperatures extracted at different positions and chamber atmosphere using V_{real}.

As it was mentioned before, although the current values remain the same, not taking into account the voltage drop results in errors in the extracted plasma parameters. Figure 3.22 shows the effects of using V_{bias} or V_{real} in the I-V plots (top). In the figure is also shown the electron temperatures for different times and pressures at both 2.6 and 4 cm from the target. For both cases the extracted electron densities

were of the order of 10^{13} cm^{-3}. In all the calculations the procedure explained in Chapter 1 was used.

Figure 3.23 shows the ions signal and the density calculated using equation (1.15). Figure 3.24 shows the Log-Log plot of the peak ion signals.

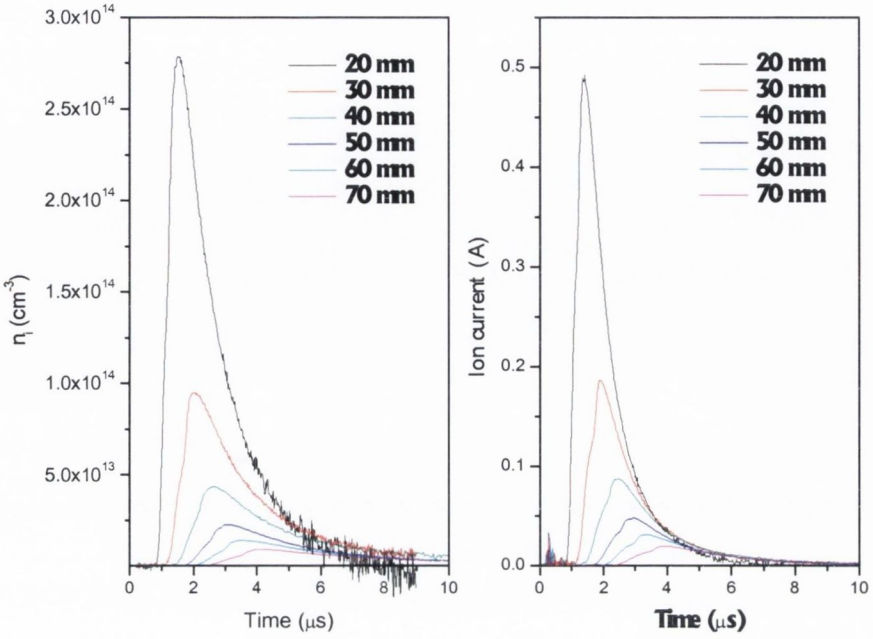

Figure 3.23. Ion signals and densities measured in vacuum at different distances from the target.

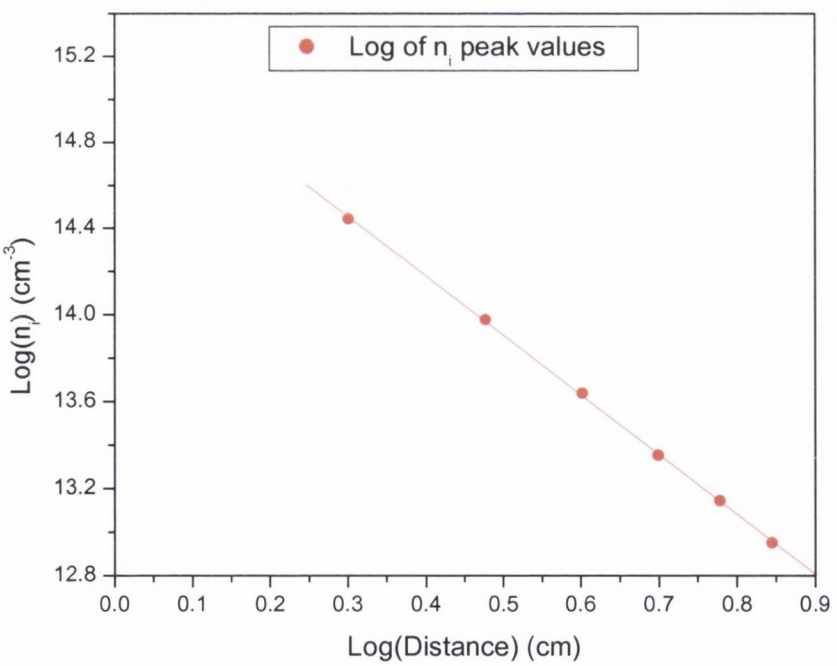

Figure 3.24. Peak ion densities as extracted from ion signals measurements in vacuum.

Although the I-V plots were corrected using V_{real} the values of the electron and the ion densities extracted from them did not agree. The electron densities are an order of magnitude lower than the ion densities. Besides, the extracted temperatures are in contradiction with the temperatures obtained from the spectroscopic analysis. Such behaviour has no evident explanation, but it could be linked with the voltage drop produced in the circuit.

As it was mentioned any voltage drop will produce an effective reduction in the bias voltage. This means that the potential difference across the probe sheath and the sheath thickness both change during the measurement. It was proposed by Waymouth [Waymouth, 1966] that this leads to a capacitive current in the probe which can change the real measurement.

3.3 Discussion and conclusions

3.3.1 Spectroscopy

Three main points could be singled out from the previous study. Firstly, the importance of confirming the prediction of the different validity criteria for assuming PLTE or LTE. Most of them have been developed specifically for hydrogen or helium-like species, so high error margins should be allowed for. A good way to confirmation is the Boltzmann plot. As pointed by Griem [Griem, 1963], discrepancies in such a plot indicates deviations from the above mentioned equilibriums. Secondly, care must be taken to identify self-absorption of the studied transitions. Finally, care most be taken in deciding to neglect or not the effects of Doppler broadening. All three points are, of course, related to the specific plasma.

3.3.2 Langmuir Probe

Increasing the capacitance and minimizing the resistance values will give small change of voltage from the one maintained by the source. For the resistance, care must be taken in order to prevent differentiation of the signal, as was explained before. It should be mentioned that the capacitance should not be too large. This is because due to the instabilities on the pulse to pulse laser generation the measurements should be averaged. An increase in the time constant C_1R_1 will cause a reduction in the frequency at which the experiment can be performed.

Although there is no direct evidence that the drained current is changed by the circuit; excessive voltage drop could lead to erroneous values of the plasma parameters.

In general terms the ionic signals tend to be less affected by the previous process and ion densities extracted from them are reliable.

Before presenting any general conclusion it would be important to mention the following. A full characterization of the plasma would require a more extensive study than the one which was presented in this chapter. That is, to extend the analysis to more spectral regions, use of other methods for characterising the level populations, etc. Such study is beyond the scope of this thesis. As will be discussed in the next chapter, plasma properties obtained in Chapter 2 together with the information extracted in the present one are sufficient to discuss and reach the main goal of this work, as stated in the thesis introduction.

In general terms both Langmuir probe and spectroscopy results suggest that the obtained plasma was weakly ionised.

The presence of PLTE of high lying atomic levels with the ionic ground state, together with the obtained low plasma temperature, gives evidence of a plasma in the recombining phase. This is in agreement with previous reports [Fujimoto, 1979].

The introduction of oxygen caused little changes apart from a tendency to accelerate the reduction in ionised species and the decrease in the temperature.

From the technical point of view it can be concluded that the combination of both Langmuir probe and Spectroscopic techniques can be used for a successful plasma characterization.

References

Griem, H. R., *Physical Review*, **131**, p. 1170 (1963).

Thorne, A., U. Litzen, and S. Johansson, *Spectrophysics* (Springer, 1999).

Born, M., *Journal of Physics D (Applied Physics)*, **32**, p. 2492 (1999).

Dimitrijevic, M. S. and N. Konjevic, *Journal of Quantitative Spectroscopy and Radiative Transfer*, **30**, p. 45 (1983).

Lide, D. R., (CRC Press, Florida, 1998).

Harilal, S. S., C. V. Bindhu, R. C. Issac, et al., *Journal of Applied Physics*, **82**, p. 2140 (1997).

Hermann, J., C. Boulmer-Leborgne, and D. Hong, *Journal of Applied Physics*, **83**, p. 691 (1998).

Waymouth, J. F., *Journal of Applied Physics*, **37**, p. 4492 (1966).

Spitzer, L., *Physics of fully ionized gases* (Interscience, 1962).

Koopman, D. W., *Physics of Fluids*, **14**, p. 1707 (1971).

Fujimoto, T., *Journal of Quantitative Spectroscopy and Radiative Transfer*, **21**, p. 439 (1979).

Chapter 4 Thin film growth

The Chapters 2 and 3 were devoted to the study and characterization of the plasma produced during the PLD of ZnO thin films. In Chapter 2 plasma features such as shape and expansion velocities were studied for both cases, in vacuum and in a gas background. While in Chapter 3 plasma composition, temperature, density and ionization degree were analysed.

As was mentioned in the introduction thin films of ZnO have been produced by wide range of techniques, including chemical vapour deposition (CVD) [Calli, et al., 1970], metallo-organic chemical vapour deposition (MOCVD) [Lau, et al., 1980] and pulsed laser deposition (PLD) [Sankur, et al., 1983]. These films have many potential applications in solar cells, light emitting devices, spin electronics, surface acoustic wave devices etc. ZnO is a wide bandgap (3.3 eV) II-VI semiconductor, which shows an efficient band-edge emission. The near UV interband emission, and its relation to the structural, stoichiometric and surface properties of the ZnO thin films, has been discussed in several papers in the recent years [Tang, et al., 1998; Wu, et al., 2001]. Studies of the influence of the film thickness [Shim, et al., 2002], oxygen pressure [Im, et al., 2000] and growth time [Vasco, et al., 2001] on the optical properties have been reported, and suggest that the oxygen stoichiometry is critical to obtaining good quality films. This chapter presents the characterization of the obtained thin films. Structure, morphology, stoichiometry and optical properties of the films will be analysed. The effects of Mn doping on both optical and magnetic properties of the ZnO thin films will be presented as well. Using the results obtained from the previous chapters conclusions on how the plasma conditions are related to the properties of the final films will be obtained.

4.1 Experimental method

Two different ceramic targets were used for PLD; a 99.99% purity ZnO and $Zn_{1-x}Mn_xO$ (x=0.13). The Mn-doped target was obtained by mixing the appropriate amount of Mn_3O_4 and ZnO, calcining at 500^0C for 5 h and sintering at 900^0C for 9 h. The general scheme of the used PLD set up was shown in Figure 1.1. A KrF (248 nm, 26 ns, 10 Hz) laser at a fluence of 1 J/cm^2 was used to ablate the targets for 10 minutes in an atmosphere of oxygen. The films were deposited on (001) sapphire

substrates at 400 ^{0}C, using two different oxygen pressures and two different target-substrate distances. Some of the films were post-annealed in the deposition chamber at the same substrate temperature and oxygen pressure as during the growth to see if there was any improvement of the crystal quality or the state of oxidation.

The surface morphology of the films was examined scanning electron microscopy (SEM) technique. Profilometer measurements of the film thickness were in the range ~ (150-200) nm, implying a growth rate of 0.03 nm/pulse. X-ray diffraction (XRD), with a Cu K_α (1.54056 A) source and θ-2θ configuration, was used to study the crystalline properties of the films. The photoluminescence of the films was measured with a HeCd (λ=325 nm) laser, a monochromator and a photomultiplier tube cooled to -23^{0}C. All the spectra were acquired for samples at room temperature using step size of 1 nm and an integration time of 1 s.

4.2 ZnO thin films

Figure 4.1 shows XRD patterns of four ZnO samples obtained for different growth conditions indicated.

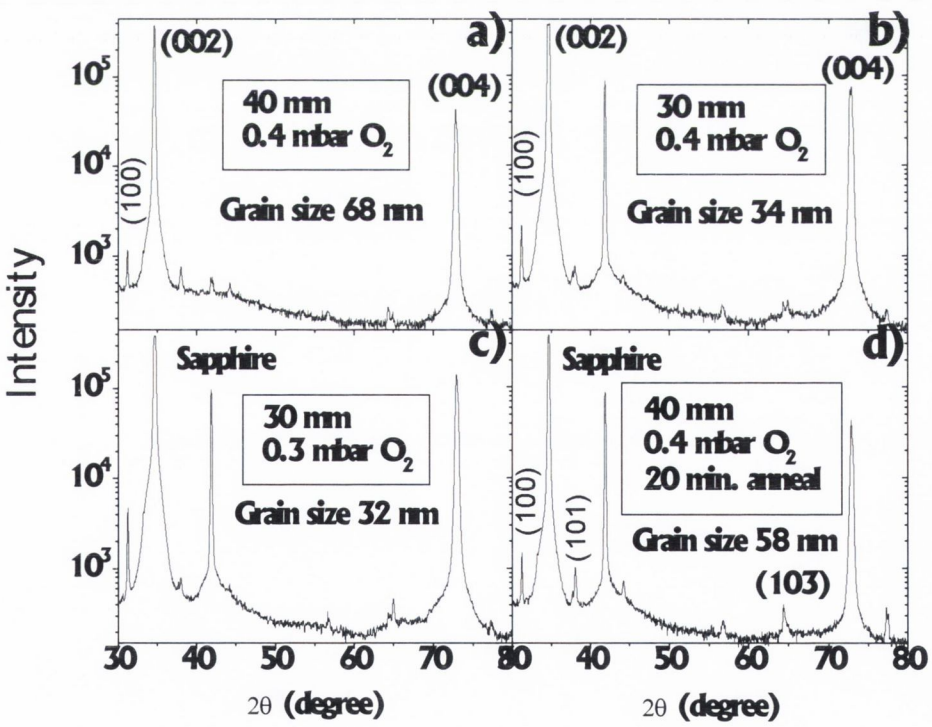

Figure 4.1 XRD pattern of c-oriented ZnO films. The corresponding grain size, as calculated using Scherrer formula, and an inset with a zoom of the intensity scale showing the presence of (100) oriented planes are also presented.

The strong (002) and (004) peaks show that there is preferential growth in the direction [00*l*]. There is relatively weak diffraction due to the presence of small quantity of (100) oriented material. The intensity and position of the (002) peak is similar for all the four samples, including the sample that was post-annealed in the chamber for 20 minutes (Fig 2(d)). All four samples were grown at the same temperature, but the two (Fig. 2(b) and 2(c)), which were deposited closer to the target at 30 mm, have a smaller grain size, as revealed by the broader diffraction lines and calculated according to the Scherrer formula. These two samples also show a higher level of diffraction from (100) planes. Comparing the XRD for the samples in Fig 2(a) and 2(d), it would seem that post-annealing does not significantly affect the crystallinity of films deposited at 40 mm.

Figure 4.2 shows the (PL) spectra of the same films as above.

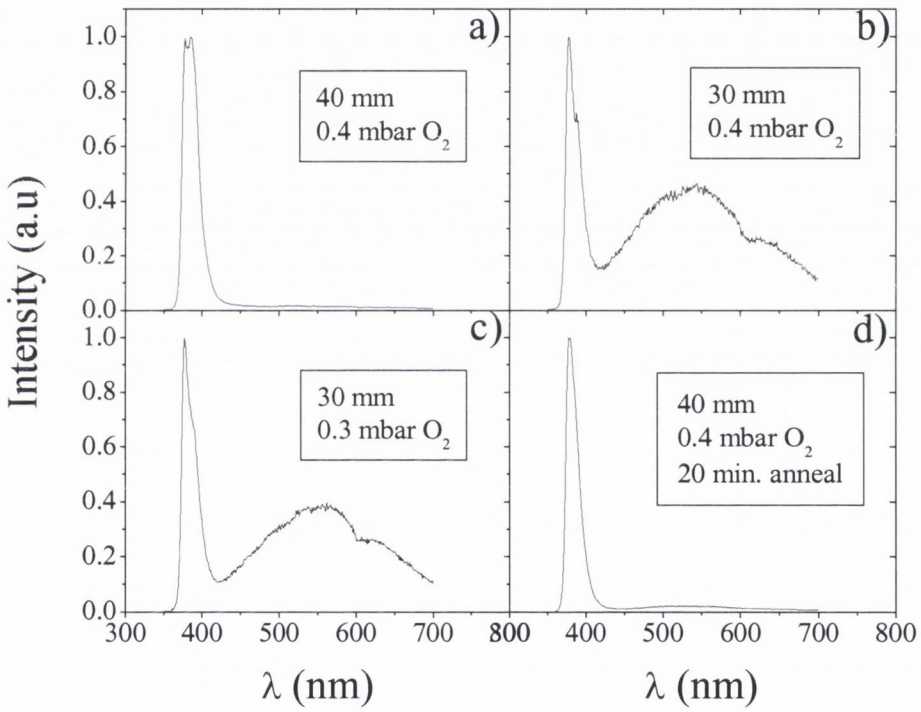

Figure 4.2. The PL spectra of all the ZnO films show the expected blue band-edge transition. The films in (b) and (c) also show yellow-green and orange bands.

All show the expected blue band associated with the band-edge transition (3.3 eV) characteristic of ZnO. However, samples grown at 30 mm Fig. 3(b) and 3(c) also show strong yellow-green and orange bands, which are understood to be associated

with oxygen vacancies [Im, et al., 2000]. Figure 4.3 shows an example of the typical surface morphology obtained in the grown thin films.

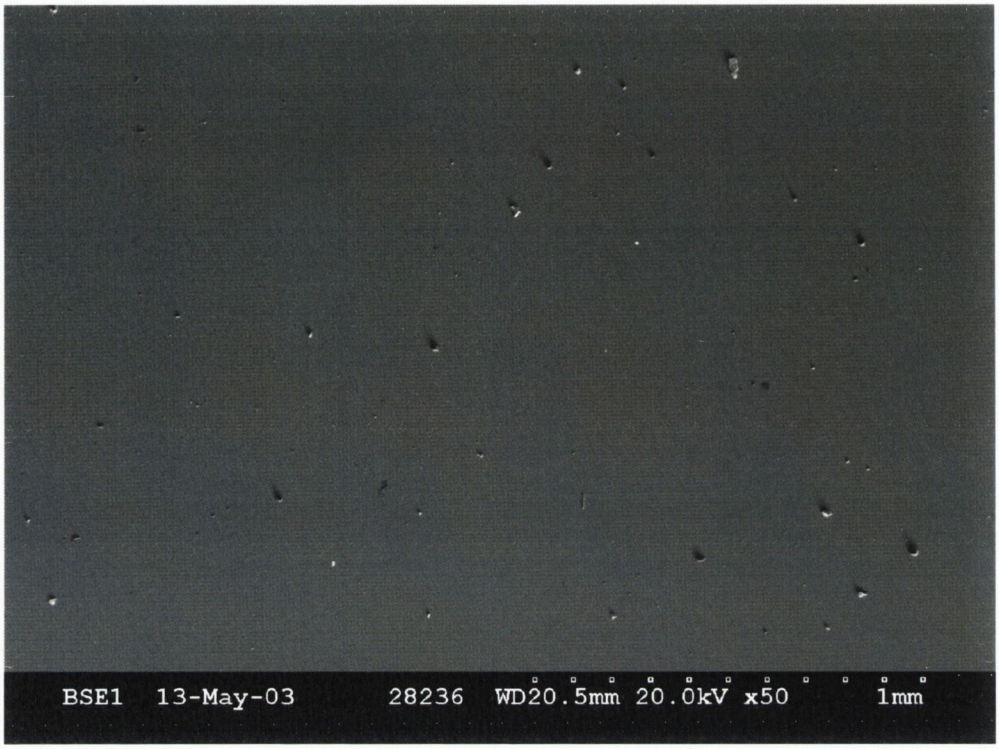

Figure 4.3. Example of the typical surface morphology of the grown thin film. The photograph was acquired using SEM with the specifications marked in the bottom of the figure.

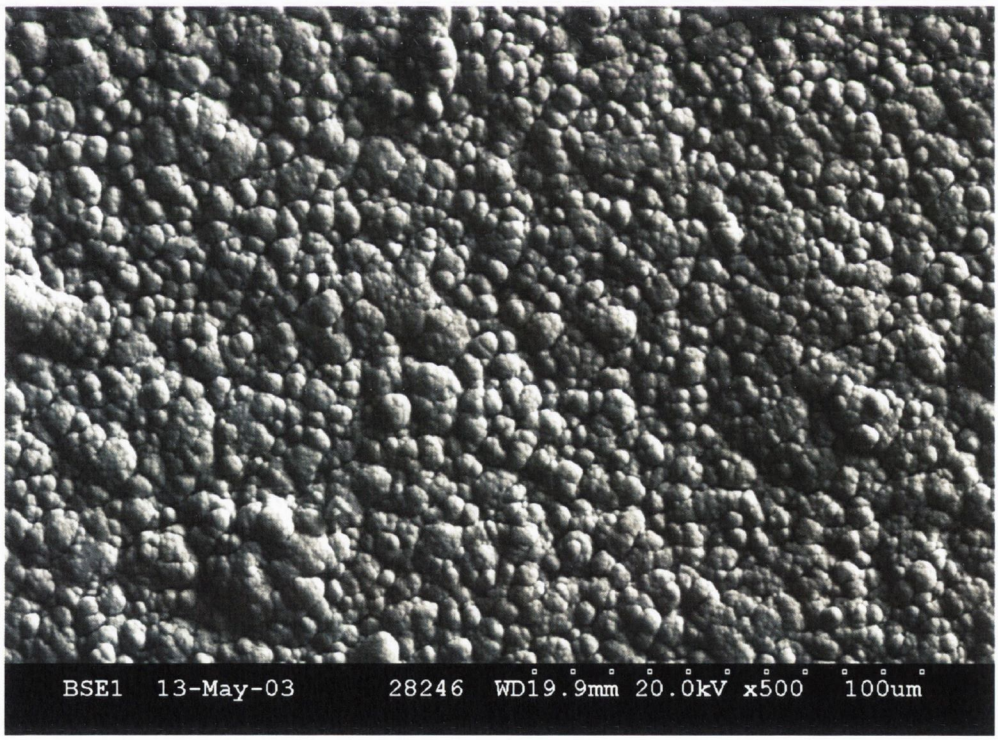

Figure 4.4. Surface morphology of the target used for the thin film growth. The photograph was acquired using SEM with the specifications marked in the bottom of the figure.

For all films the characteristic droplet was detected. Apart from it the films showed a reasonable smoothness. Several mechanisms have been discussed to be responsible for the droplet generation in PLD [Chrisey, et al., 1994]. In the case presented here seems to be due to the direct transport of target grains onto the substrate. This can be understood by looking at the SEM photograph of the target (Figure 4.4).

4.2.1 ZnMnO films

Figure 4.5 shows the XRD patterns of two ZnMnO samples.

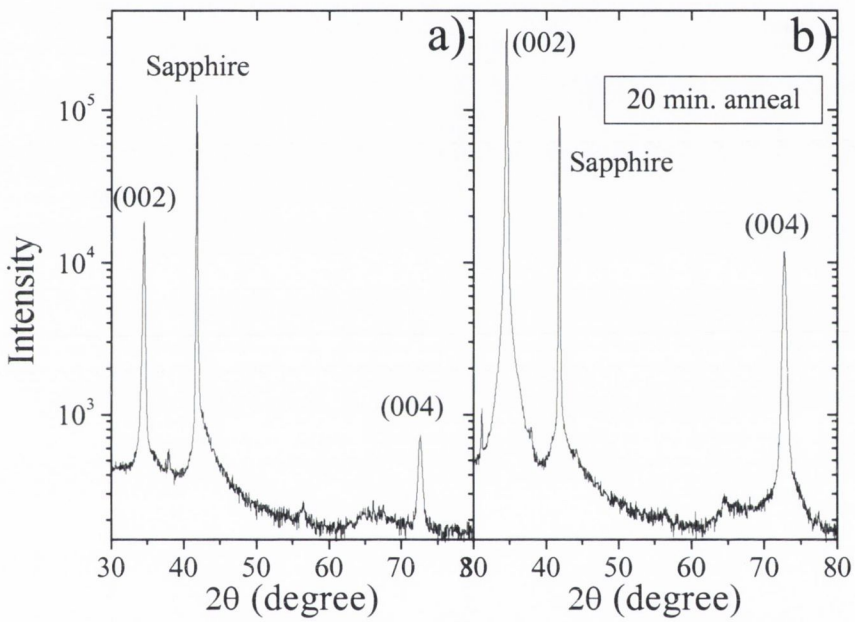

Figure 4.5. XRD pattern of ZnMnO films (a) without and (b) with post-annealing.

As for the pure ZnO films the strong (002) and (004) peaks show that there is preferential growth in the direction [00*l*] and that there is relatively weak diffraction due to the presence of small quantity of (100) oriented material.

The Mn fraction was measured to 13 % using energy dispersive analysis by X-ray (EDAX) in the SEM. These Mn-doped films have the same crystal structure of the pure ZnO, but with a small shift of the diffraction peaks to lower angles, indicating the expected enlargement of the c axis due to Mn doping [Fukumura, et al., 1999].

The magnetic properties of the films were studied using SQUID measurements. Figure 4.6 and 4.7 show the results obtained for the magnetic moment as a function of both the magnetic field and the temperature respectively.

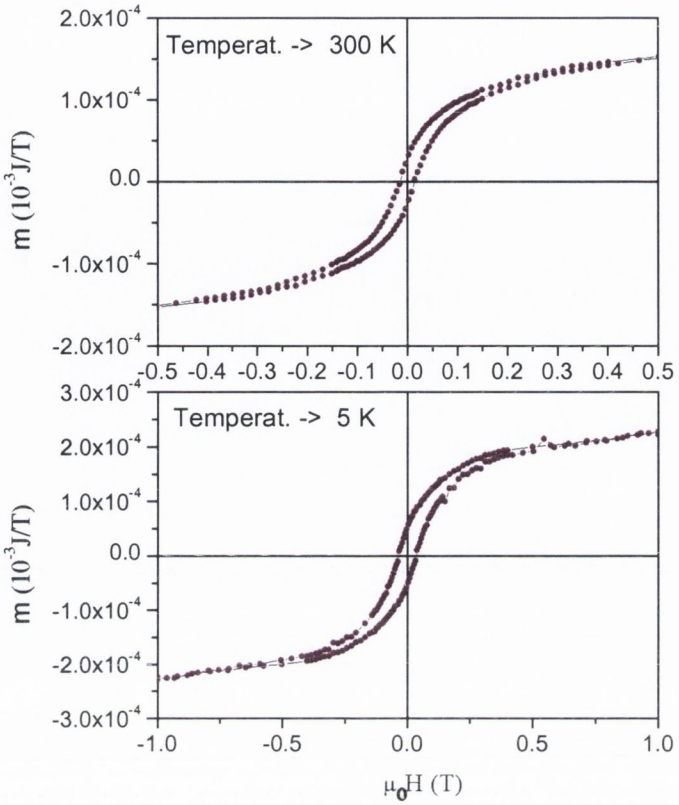

Figure 4.6. Behaviour of the magnetic moment of the films as a function of the magnetic field for two different sample temperature.

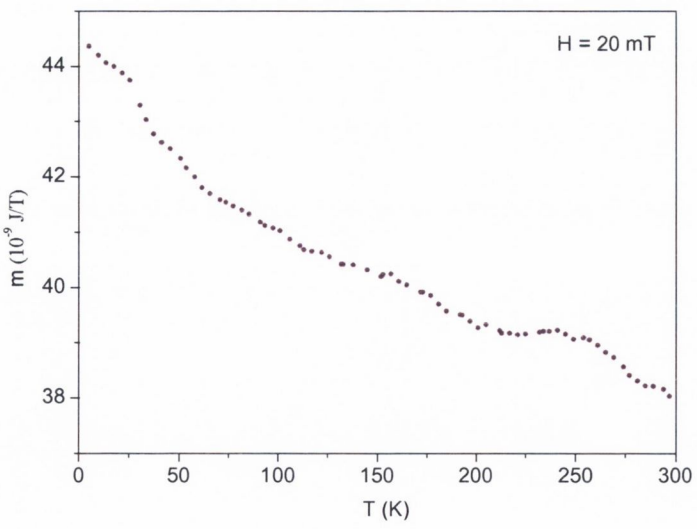

Figure 4.6. Behaviour of the magnetic moment of the films as a function of the temperature. At a constant magnetic field.

The X-ray mapping performed to the films (Figure 4.7) rule out the possibility that the magnetic properties exhibited by the films were due to accumulations of Mn.

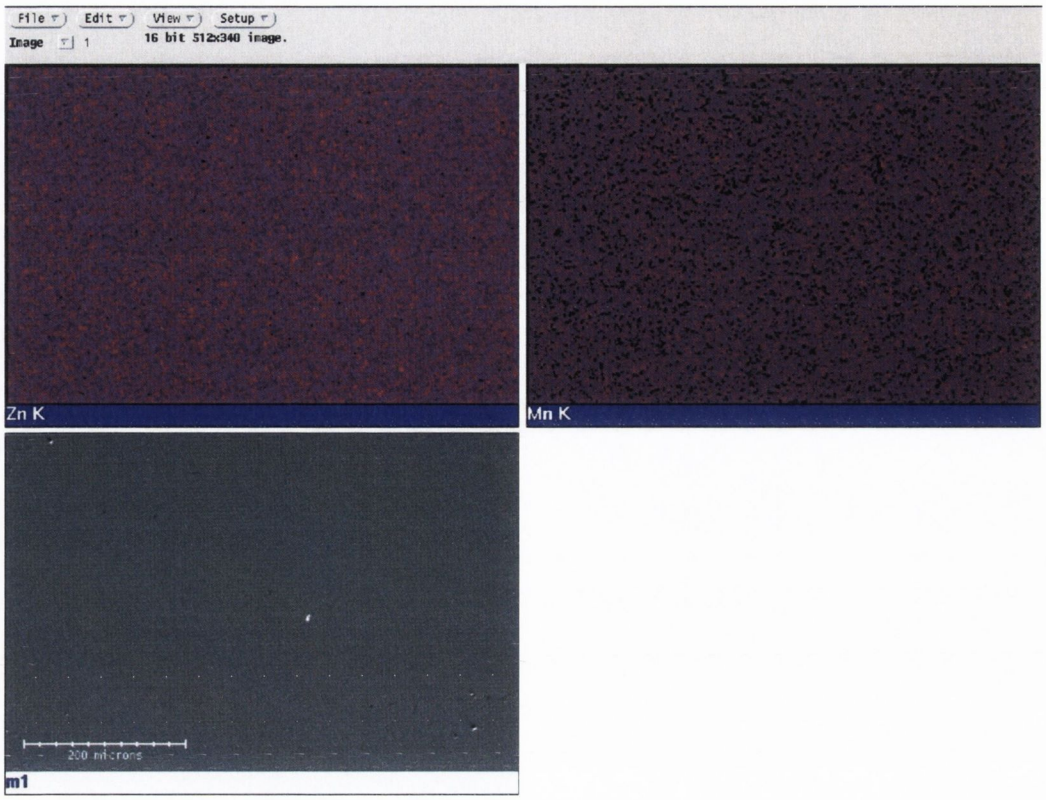

Figure 4.7. Example of the X-ray mapping performed to the Mn doped thin films. In the figure the colour scale goes from black (no signal) to red (maximum detected signal).

Here we observe that post-annealing for 20 minutes has a significant effect on the crystal quality as evidenced by the increase in both intensity of the (00*l*) peaks and grain size. The PL for these Zn-doped films also showed the blue band emission, but with strong quenching of the intensity, as is expected for heavily Mn-doped material [Osiko, 1959].

4.3 Discussion

In general the results can be summarised as follow. For the ZnO case the studied films were grown with similar growth parameters, yet dramatic differences in their final properties were obtained. Besides, annealing of a sample with good as grown quality, did not improve it. From the PL study can be concluded that such a quality difference is related to the oxygen stoichiometry in the films. The Mn doped ZnO films were grown using the same parameters with which the best ZnO thin films were obtained. In this case annealing did improve the film quality.

In explaining the above results the first step will be to discuss the possible mechanisms of oxygen incorporation.

During the plasma expansion the following reactions can take place:

$$\begin{aligned} &Zn^{+} + O_2 \rightarrow ZnO^{+} + O \\ &Zn^{*} + O_2 \rightarrow ZnO + O \\ &Zn + O_2 + e^{-} \rightarrow ZnO + O + e^{-} \end{aligned} \qquad (4.1)$$

The third reaction could be obtained as well with an energetic atom instead of the electron. Besides, any of the above reactions can take place with atomic oxygen. The first reaction in equation (4.1) has been reported [Fisher, et al., 1990] to have a threshold of about 3 eV and a maximum cross section at 6 eV. Although no data was found for the energy requirement of the second reaction, it can be expected that the excitation of the atomic zinc should, at least, equal the dissociation energy of the oxygen molecule (5.12 eV). Similar energy requirement should fulfil the electron participating in the third reaction.

In the Chapter 2 it was shown that for the pressures at which the films were grown a clear blast wave is developed as early as 500 ns after the laser pulse arrival (Figure 2.10). Besides, such a blast wave was decelerated to energies lower than 1 eV (Figure 2.11). From this the possibility for the first reaction of taking place can be ruled out. Similar behaviour would be expected for the electrons in the contact front of the plasma, ruling out the third reaction.

Reaction inside the plasma plume will have little probability due to the low plasma temperature, which from the spectroscopic analysis were obtained to be of the order of (0.2-0.5) eV. Furthermore, incorporation of oxygen due to reactions involving charged particles (Zn^{+}, e^{-}) would be negligible compared to the reaction with neutral species. This is due to the low ionization ratio of the produced plasma during the deposition process, as was shown in Chapter 3.

The probability of occurrence for the second reaction is favoured, firstly, for the predominance of atomic zinc in the plasma plume. Secondly, as seen in the recorded spectra (Chapter 3), transitions from levels of energy as high as 7.78 eV and 8.11 eV are detected. Of course in such a reaction the maximum released energy will be about 4 eV, which is the maximum achievable energy among the allowed transitions for the involved levels. There is only one excited state, within the studied spectral region, from which the excited atoms will produce enough energy to drive such a reaction. This is the level $4s4d\ ^1P_0$ with a strong allowed transition to the ground state and an

energy difference of 5.79 eV. It is perhaps this is the reason of the strong radiance reduction observed for the line (636.234 nm) with the introduction of 0.4 mbar of oxygen (Figure 3.3). This line has the level $4s4d\ ^1P_0$ as the transition lower level (Figure 3.4). A decrease of the population of this level will reduce the probability of population of the upper transition level ($4s4d\ ^1D$) due to collisional excitation. Although, it reduces as well the opacity of this line, causing an increase in the radiance. An absolute assessment of this would require a full characterization of the processes populating and depopulating these levels and accounting for self-absorption.

In any case should the second reaction being taking place little or no differences would be expected for an increase from 0.3 mbar to 0.4 mbar which is the difference in the pressures used for the growth of the films under analysis.

It seems from above that determining processes of oxygen incorporation take place at the substrate surface. If this is the case the oxidation of the film could be divided into two steps. The first step takes place during the material arrival onto the substrate; the second step will take place in the period of time between pulses.

During the first step the material will condense as metal. For temperatures between (370-415) °C, the weight gain per area (ι) in g/cm^2 of the forming oxide will follow a parabolic law [Tuck, et al., 1981] as a function of time (t), defined by:

$$\iota^2 = \kappa_p t \tag{4.2}$$

where κ_p ($\times 10^{-12}$ g^{2}cm^{-4}s^{-1}) is the parabolic constant. This constant varies logarithmically with the oxygen pressure (P_0) in torr. The variation for a temperature of 405 °C follows the expresion:

$$\kappa_p = 1 + 1.55 Log(P_0) \tag{4.3}$$

For temperatures between (320-370) °C, the weight gain per area varies logarithmically [Tuck, et al., 1981] with time following the equation:

$$\iota = \kappa_e \log\left(1 + \frac{t}{\tau}\right) \tag{4.4}$$

where κ_e ($\times 10^{-6}$ g cm^{-2}) and τ are constants which are not pressure dependent (Table 4.1).

Deciding which of the two laws determine the oxidation for the PLD setup used in the film growth is not trivial. As it was mentioned in the Chapter 1, error in the substrate temperature is ~ 15 %, which cover both temperature regions.

Table 4.1. Logarithmic rate constants.

Temperature (°C)	κ_e ($\times 10^{-6}$ g cm^{-2})	τ (s)
365	14	1.6
360	13	1.5
355	12	2.2
350	11	2.6
345	10	2.8
340	9	2.7
330	7	2.2
320	6	2.5

As mentioned earlier in this chapter the average deposition rate was 0.3 nm/s or 0.03 nm/pulse. Knowing that the area of the substrate is 0.25 cm^2 and using the zinc bulk density (5.6 g/cm^3) the mass of material deposited per second is calculated to be 4.2×10^{-8} g/s or 4.2×10^{-9} g/pulse. Using equation (4.4), assuming a substrate temperature of 365 °C, the weight gain in 1s is calculated to be 9.5×10^{-10} g/s. If equation (4.2) is used, after evaluating equation (4.2) for 0.3 torr (0.4 mbar), the weight gain is 1.1×10^{-7} g/s.

These results, as a first approximation, suggest that an oxidation process following a parabolic behaviour in time would be more probable. It is a first approximation because, really, the material during a PLD process does not arrive to the substrate in a continuum basis but as "packs" of material over a period of time defined by the time over which the plasma plume remains in contact with the substrate.

Figure 4.8 shows the normalised ion signals acquired with the same conditions as the films under discussion were grown.

The ion signals show that for 40 mm the residence time of the plasma in the vicinity of the substrate deposition time is about 100 μs, whereas at 30 mm it is only about 40 μs. It means that the real rate of mass arrival to the substrate is 4.2×10^{-11} g/μs and 1.1×10^{-10} g/μs respectively. Calculations of equations (4.2) and (4.4), now for 1 μs, give 1.2×10^{-10} g/μs and 9.5×10^{-16} g/μs respectively. These results confirm the oxidation with parabolic time dependence as the most probable. Although the rate

of mass arrival to the substrate at both distances are lower than the weight gain due to the parabolic oxidation, at 40 mm the rate of mass arrival (one order less than at 30 mm) insures a better oxidation.

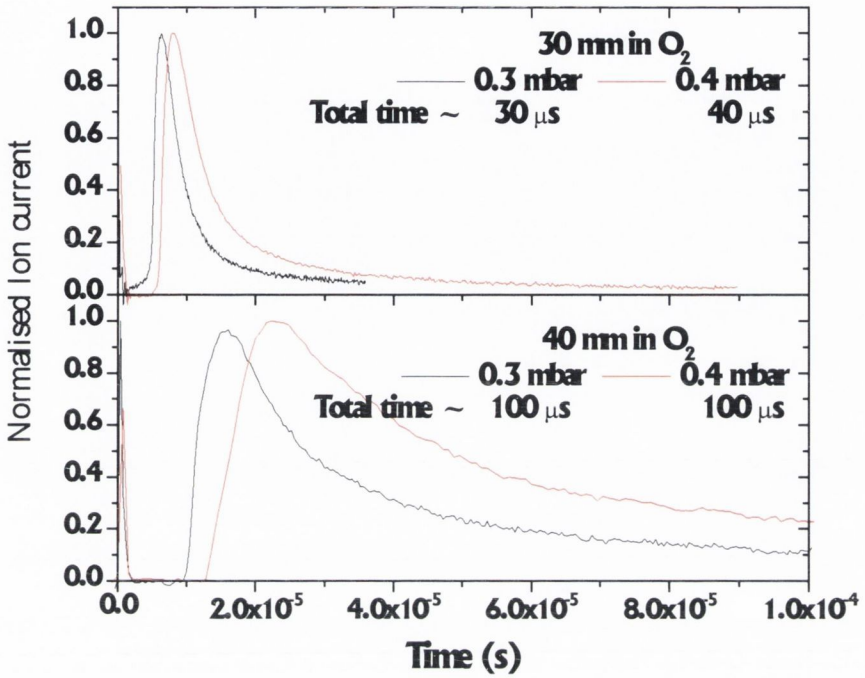

Figure 4.8. Normalised ion currents acquired with the same conditions used for the growth of the ZnO films under discussion.

During the second step, which takes place after the plasma plume moved away the substrate position, the material will be oxidised, so oxygen incorporation will no longer follow the laws above described. The oxygen incorporation will be mainly due to the diffusion into the formed ZnO [Robin, et al., 1973]. This is a process which involves interaction with defects and hole migration. The diffusion coefficient has been measured to vary from 4.9×10^{-16} to 3.2×10^{-15} cm^2/s within the temperature range from 940 to 1141 °C and at 700 torr of oxygen. Diffusion data for lower pressures and temperatures are not available, but it is to be expected a decrease in the coefficient values. In general the depth of the diffusion will at most be of the order of Ångströms, which is only noticeable at earlier times of the growth when the film thickness is of this order.

Regarding the ZnMnO films, the main feature distinguishing them from the ZnO films, is that annealing after deposition produces a dramatic increase in the crystal

quality. This suggests that incorporation of oxygen during both the plasma expansion and condensation onto the substrate was poor. Even when grown with conditions at which the best ZnO thin films were obtained. Manganese is expected to drive reaction with oxygen much easier than zinc as it has both lower threshold and greater cross section values [Fisher, et al., 1990].

Figure 4.9 shows the normalised ion signals acquired at the same conditions used for the films growth.

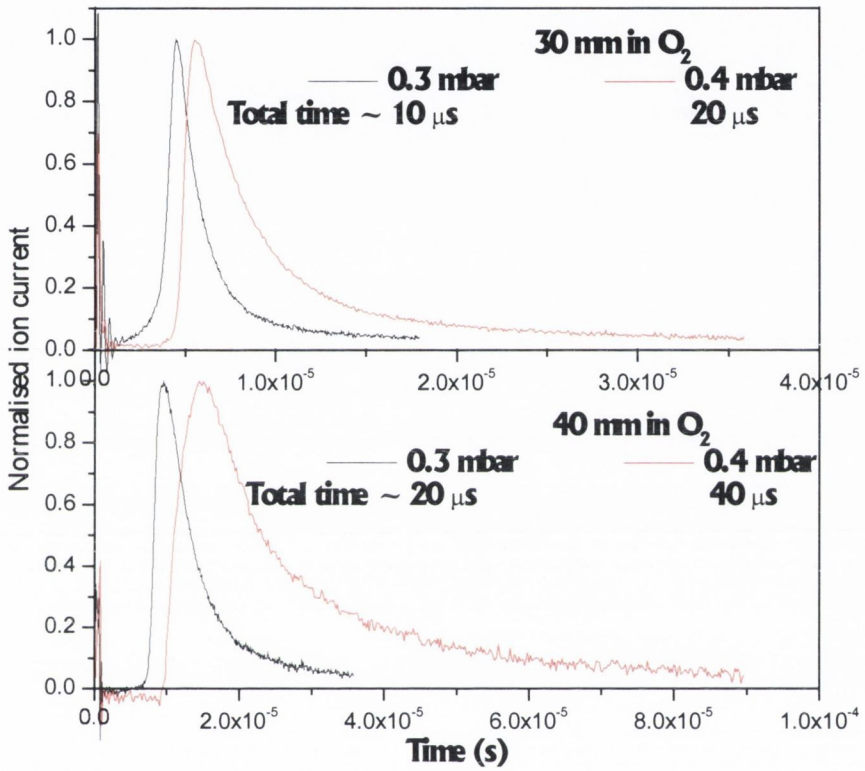

Figure 4.9. Normalised ion currents acquired with the same conditions used for the growth of the ZnMnO films under discussion.

From the analysis developed in Chapter 2 for the laser produced plasma from the pure ZnO target, it can be concluded that the plasma obtained from the Mn doped target was more energetic. Both the relative narrow with of the signals and that the signal recorded at 40 mm in 0.4 mbar shows no evidence of diffusion like behaviour support this statement. Although a conclusive explanation needs a full study, a possible reason for such result is an increase in the amount of energy absorbed during the laser-material interaction. In any case the fact that the time of residence of the plasma at the substrate position is lower by about a factor of 2 supports the discussion presented for the ZnO thin films.

4.4 Conclusion

PLD has been used to grow of ZnO thin films with good structural and optical properties. We have confirmed the earlier result that a substrate temperature of 400^0C is sufficient to obtain crystalline growth of ZnO on sapphire. The grown Mn doped ZnO films presented as well good structural properties. The optical properties showed the expected shift toward higher band gap energies and quenching in the luminescence. Good magnetic properties were obtained, showing high critical temperature. For both materials was shown that all or at least the most important component of the oxygen incorporation to the thin film takes place during the condensation of the material onto the substrate.

References

Calli, G. and J. E. Coker, *Applied Physics Letters*, **16**, p. 439 (1970).

Lau, C. K., S. K. Tiku, and K. M. Lakin, *J. Electrochem. Soc.*, **127**, p. 1843 (1980).

Sankur, H. and J. T. Cheung, *Journal of Vacuum Science & Technology A*, **1**, p. 1806 (1983).

Tang, Z. K., G. K. L. Wong, P. Yu, et al., *Applied Physics Letters*, **72**, p. 3270 (1998).

Wu, X. L., G. G. Siu, C. L. Fu, et al., *Applied Physics Letters*, **78**, p. 2285 (2001).

Shim, S., H. S. Kang, J. S. Kang, et al., *Applied Surface Science*, **186**, p. 474 (2002).

Im, S., B. J. Jim, and S. Yi, *Journal of Applied Physics*, **9**, p. 4558 (2000).

Vasco, E., C. Zaldo, and L. Vazquez, *Journal of Physics: Condensed Matter*, **13**, p. 663 (2001).

Chrisey, D. B. and G. K. Hubler, (Wiley, New York, 1994).

Fukumura, T., Z. Jin, A. Ohtomo, et al., *Applied Physics Letters*, **75**, p. 3366 (1999).

Osiko, V. V., *Opt. Spectra*, 7, p. 454 (1959).

Fisher, E. R., J. L. Elkind, D. E. Clemmer, et al., *Journal of Chemical Physics*, **93**, p. 2676 (1990).

Tuck, C. D. S., M. E. Whitehead, and R. E. Smallman, *Corrosion Science*, **21**, p. 333 (1981).

Robin, R., A. R. Cooper, and A. H. Heuer, *Journal of Applied Physics*, **44**, p. 3770 (1973).

Conclusions and future work

The thesis was divided in three main sections, two of them (Chapter 2 and 3) were devoted to the study and analysis of the laser produced plasma. Finally in the third section (Chapter 4) the conclusions obtained in the first two sections were used as the basis for the explanation and discussion of the results obtained from the film growth.

In the Chapter 2 both the in-vacuum and in-a-gas-background plasma expansion were analysed.

- In vacuum all the analysis was based on the Anisimov model. Using ion signals, acquired with a Langmuir probe, it was corroborated that this model describes successfully the expansion of laser produced plasma.
- In the case of plasma expansion in a background gas, firstly, a full characterization of the expansion was performed using ICCD photography and ion signals. The Sedov-Taylor model was applied and shown that whilst it describes the general features of the expansion, i.e. front expansion $\sim t^{2/5}$, it failed in a full description of the plasma properties.
- It was proposed that the Freiwald-Axford model may be more appropriate for the description of the plasma expansion in a background gas. However this model was not applied in its original form. Based on some assumptions, which were used by the authors during the mathematical formulation of the model, the idea of describing the plasma contact front instead of the commonly described shock front was proposed.
- The above proposition allowed us at the same time to use the plasma specific heats ratio as obtained from Anisimov model instead of approximated values of the same physical magnitude but for the gas background.
- A detailed comparison between the two models and the correctness of the plasma expansion velocities, positions and pressures corroborated that such an approach was correct.
- As a result of the model comparison it was shown that the use of ion signals as extracted using the Langmuir probe is not correct for describing the plasma front. On the other hand the use of ICCD photography is correct.

- It was corroborated that due to the interaction with the background gas the plasma reaches a maximum in its expansion which is well predicted by the Predtechensky model. Beyond this distance the plasma enters into a diffusive regime which is well described by a 3-D diffusion model.
- In general it was shown that plasma properties such as initial energy and specific heats ratio obtained from the Anisimov model can be used as input for the initial conditions of the plasma expansion in a background gas.

In Chapter 3 the study was directed to the plasma internal properties. Using emission spectroscopy the plasma was shown to be composed mainly of atomic species. All the detected emission lines were representative of Zn transitions. Theoretical validity criteria for the assumption of existence of LTE or PLTE in the plasma were applied.

- It was shown that the Boltzmann plot is a good way of testing such criteria. Both deviations in this plot and in the relative line radiances within the different multiplets were indicative of the presence of self-absorption.
- From an analysis of the different mechanisms of line broadening it was concluded that the Stark effect was predominant among the pressure mechanisms.
- The Doppler broadening was discussed and it was shown that for a laser produced plasma expanding in vacuum this broadening was due to the supersonic velocities of the plasma expansion rather than the thermal velocities of the radiating species.
- It was proposed to calculate a "median" value of such broadening by using the angular distribution of the species in the plasma, as calculated with the Anisimov model.
- Synthetic spectra were generated to fit those experimentally obtained and from them the plasma ion/electron density and the temperature were extracted. All calculations were performed taking line self-absorption into account. Good agreement between the ion densities extracted with the Langmuir probe and from the synthetic spectra was found. The importance of considering the Doppler broadening was also shown.

- It was demonstrated that the criteria for PLTE overestimates the minimum energy level down to which such equilibrium will apply. Once more the Anisimov model proved to be of great help in setting boundaries to some of the variables in the calculation.

Also within this chapter, the Langmuir probe technique was studied. A discussion was presented where the typical Koopman circuit is analysed.

- It was demonstrated that it behaves as a passive high pass filter which does not affect the drain current unless the signal frequency is less than the circuit cut-off frequency.
- It was shown, however, that care must be taken with the voltage drop due to the drain current. It can offset the bias voltage leading to a wrong I-V plot and the consequent error in both temperature and electron density extracted from it.

In Chapter 4 the results obtained from the thin film depositions were presented. Structure, surface smoothness and optical properties of the ZnO thin films were studied and shown to present good quality. Similar results were presented from the Mn doped ZnO thin films. In this case the magnetic properties were as well presented, showing that the obtained films have high critical temperature (> 300 K).

- It was shown that oxygen incorporation into the growing thin film occurs, preferentially, during the material condensation on the substrate.

Finally, the following question was posed in the introduction of the thesis: Can the optimum conditions for the growth of good quality thin films can be predicted from models or at least bounded between some limits?

The answer is, yes. In order to produce a thin film of a given oxide material the following steps will lead to a faster and easier growth process:

1. To search and identify the mechanisms which direct a normal oxidation of the evaporated elements, i.e. optimum pressure and temperature. At the same time to look for the cross sections for chemical collision.
2. From an ablation in vacuum monitored with Langmuir probe and emission spectroscopy the plasma should be characterised. That is, after calculating the mass loss the initial energy of the plasma can be extracted which gives a rather accurate idea of the amount of energy couple to the plasma from the laser pulse. The specific heats ratio is determined.

3. Using these parameters and the Freiwald-Axford model the behaviour of the plasma expansion in a given gas background pressure can be obtained. Possibility of reaction in the plasma front can be assessed from the calculated expansion kinetic energy. Maximum expansion distance can be obtained as well from this model and corroborated with the Predtechensky model.

In this way it can be estimated whether chemical reactions are possible during the plasma expansion or if the oxidation will take place on the substrate. Depending on all the results it can be decided whether to increase the laser energy or the pressure of the gas background or decide if the substrate will be placed in a region in which the plasma is still driving a blast wave or is diffusing.

As a future work it would be interesting to develop the same procedure for other materials and gases.

Appendix A

E. de Posada, G. Tobin , E. McGlynn, and J.G. Lunney, "Pulsed laser deposition of ZnO and Mn-doped ZnO thin films", *Applied Surface Science*, v 208-209, n 1, Mar 15, 2003, p 589-593

D. O'Mahony, **E. de Posada**, J. G. Lunney, J. P. Mosnier, E. McGlynn, "Pulsed laser deposition of wide bandgap semiconductor thin films", Proc. SPIE, 4876, 508-516 (2002).

C. Roy, S. Byrne, E. McGlynn, J-P Mosnier, **E. de Posada**, D. O'Mahony, J.G. Lunney, M. Henry, "Correlation of Raman and X-Ray Diffraction Measurements of Annealed Pulsed Laser Deposited ZnO Thin Films", *Thin Solid Films*, v 436, n 2, Jul 31, 2003, p 273-276

Enda McGlynn, James Fryar, Martin O. Henry, Jean-Paul Mosnier, James G. Lunney, Donagh O' Mahony and **Eduardo de Posada,** "Exciton–polariton behaviour in bulk and polycrystalline ZnO", Physica B, 340-342, (2003) 230-234.

G. Tobin, E. McGlynn, M. O. Henry, J. P. Mosnier, J. G. Lunney, D. O'Mahony and **E. de Posada,** "Ultraviolet stimulated emission from bulk and polycrystalline ZnO thin films with varying grain sizes", Physica B, 340-342, (2003) 245-249.